Response of the Benguela upwelling system to changes in the wind forcing

Dissertation

zur

Erlangung des akademischen Grades
doctor rerum naturalium (Dr. rer. nat.)
der Mathematisch-Naturwissenschaftlichen Fakultät
der Universität Rostock
angefertigt am
Leibniz-Institut für Ostseeforschung Warnemünde (IOW)

vorgelegt von
Tim Junker, geb. am 22.12.1984 in Gotha

Rostock, July 28, 2014

urn:nbn:de:gbv:28-diss2014-0169-9

Erster Gutachter:	Prof. Dr. Wolfgang Fennel
	Leibniz-Institut für Ostseeforschung Warnemünde
Zweiter Gutachter:	Prof. Dr. Arne Biastoch
	GEOMAR Helmholtz-Zentrum für Ozeanforschung Kiel

Tag der Einreichung:	24.01.2014
Tag des Promotionskolloquiums:	23.05.2014

Acknowledgements

I would like to thank my supervisor Prof. Dr. Wolfgang Fennel at the Leibniz-Institute of Baltic Sea Research Warnemünde (IOW) for his guidance and advice during this research work.

The realistic numerical model of the South-East Atlantic is run by Dr. Martin Schmidt at the IOW. A climatology of the most important output variables from that model was calculated by Dr. Anja Eggert likewise working at the IOW. Thank you both for your valuable support.

I express my gratitude to Dr. Volker Mohrholz (IOW) for critical and helpful comments during the evolution of this study.

I would like to extend my thanks to the staff of the Department of Physical Oceanography and Instrumentation at the IOW, in particular to the people working in the Theoretical Oceanography and Numerical Modelling working group.

Special thanks should be given to Inga Haller for her input in the final editing stage of this thesis.

The mean ocean dynamic topography data used in this study has been obtained from Nikolai Maximenko (IPRC) and Peter Niiler (SIO). Data covering the years 1992 to 2002 was downloaded from the Asia Pacific Data-Research Center (http://apdrc.soest.hawaii.edu/projects/DOT).

I wish to acknowledge also use of the Ferret program for analysis and graphics in this study. Ferret is a product of NOAA's Pacific Marine Environmental Laboratory. (Information is available at http://ferret.pmel.noaa.gov/Ferret/)

Contents

List of Figures

List of Tables

List of Abbreviations

ABF	Angola-Benguela front
AC	Angola Current
ASCAT	Advanced Scatterometer
BC	Benguela Current
BUS	Benguela upwelling system
BVF	Brunt-Väisälä frequency
CFC	Cape Frio cell
CJ	Coastal jet
CVT	Cumulated vertical transport
EBC	Eastern boundary condition
ESACW	Eastern South Atlantic Central Water
FT	Fourier transformation
GCM	General circulation model
IOW	Leibniz-Institute of Baltic Sea Research Warnemünde
LFA	Low frequency approximation
LRWA	Long Rossby wave approximation
LWA	Long wave approximation
MDOT	Mean dynamic ocean topography
MOM	Modular Ocean Model
NCEP	National Centers for Environmental Prediction
PUC	Poleward undercurrent
QuikSCAT	Quick Scatterometer
SACW	South Atlantic Central Water
SCOW	Scattered Climatology of Ocean Winds
SST	Sea surface temperature
WOA	World Ocean Atlas
WSC	Wind stress curl
WSCA	Wind stress curl anomaly

1. Motivation, aim, and outline

Winds are the largest source of momentum acting on the oceans surface layer. In the Benguela upwelling system (BUS), the wind forcing is of particular importance because the southeast trade winds drive upwelling. As a consequence, nutrients are transported into the euphotic zone and stimulate primary production. This signal propagates through the food web. The state of the Benguela ecosystem and its productivity depends highly on the biogeochemical characteristics of the upwelling water originating typically from a depth of 100 to 200 meter. This in turn is impacted by the vertical current component and the characteristics of the source water. Its composition is largely affected by the meridional velocity as the two main central water masses enter the BUS from opposite directions. The structure of both the meridional and the vertical velocity depends on the strength and spatial shape of the wind forcing. Remotely sensed wind data that is available for a few years in high spatial resolution reveals that the wind patterns are very pronounced and persistent in the BUS. The prevailing meridional winds exhibit spatial inhomogeneities in the order of a few 100 km that result in a wind stress curl (WSC) and a wind divergence. Moreover, the wind forcing exhibits temporal variations. Wind pulses of about two to ten days duration overlay the annual and semi-annual cycle of the forcing.

The present study aims at understanding the coastal currents response in the BUS to spatial and temporal variations of the wind forcing. This may provide new insights in how the wind impacts the ecosystem conditions on the southwest African shelf. In addition, the results of this study may help improving general circulation models (GCMs) by understanding their dynamical shortcomings in eastern boundary upwelling systems.

In order to investigate the basic physical processes in the currents response to the wind forcing, an analytical model is applied. In contrast to most theoretical studies on eastern boundary systems that focus mainly on cross-shore variations of the wind field, this model takes into account zonal *and* meridional variations of the forcing. The model wind mimics hereby observations and can be adjusted by the choice of parameters. An idealized numerical box model is used to verify the outcome of the analytical model. The results are combined with the data from an oceanic GCM and observations and used to explain the impact of spatial and temporal changes of the wind forcing on the currents response. The study focuses hereby on three major aspects of the BUS: the seasonality of the meridional transport along the southwest African coast, the cross-shore advection in the very northern BUS, and the spatial and seasonal variation of the upwelling.

The study is organized as follows: a brief introduction to the most important characteristics of the BUS and the theory of eastern boundary upwelling systems is given in chapter 2. In chapter 3, an analytical theory for the BUS is developed taking into account spatial inhomogeneities of the wind forcing. Chapter 4 is dedicated to the introduction of two numerical models that are used throughout this study. In chapter 5, the results of the analytical model, the numerical models and observations are combined to investigate the response of the coastal currents in the BUS to changes in the wind forcing. Finally, a summary including the most important results of this study is given in chapter 6.

2. General introduction

2.1. The Benguela upwelling system

2.1.1. Location and boundaries

The BUS is an area on the shelf of southwest Africa extending approximately from 15°S to 34°S. The BUS is among the four major eastern boundary upwelling systems in the world oceans, Chavez and Messie (2009). Cold upwelled water supplies the euphotic zone with nutrients stimulating high primary production in those systems. The fact that the BUS is meridionally bounded by warm water systems makes it unique among these major upwelling areas, Shannon and Nelson (1996). The persistence and strength of upwelling in the BUS varies with latitude. Areas of intense upwelling are located off Cape Frio (18.4°S) and Lüderitz (26.4°S). The Lüderitz upwelling cell divides the BUS itself into two subsystems: the northern and the southern BUS, Hutchings et al. (2009).

To the north, the BUS is bounded by the Angola-Benguela front (ABF) located roughly between 15°S and 17°S. Its position varies seasonally. The ABF can be found farthest north in austral winter and most south during summer, Meeuwis and Lutjeharms (1990). The southern boundary of the BUS can be regarded as the area of the Agulhas current retroreflection near the Cape of Good Hope (34.4°S). A map showing some important geographic features of the Benguela region as well as the bathymetry of that area is presented in figure 2.1.

A comprehensive review of the BUS was presented by Shannon and Nelson (1996) and Shillington (1998).

2.1.2. Circulation and water masses

The large scale circulation in the South-East Atlantic is dominated by the northwestward flowing Benguela Current (BC) that is the eastern boundary current of the South Atlantic and the eastern branch of the subtropical gyre. The upper level circulation in the South Atlantic is described in Peterson and Stramma (1991). The interaction of the BUS with the subtropical gyre and the subtropical cell was addressed in Lass and Mohrholz (2008). Interaction happens for instance by poleward outbreaks of the Angola Current (AC) carrying suboxic waters with high nutrients along the African shelf into the northern BUS.

The cross-shelf communication of the BUS with the open ocean and the BC is governed by the Ekman offshore transport in the mixed layer, the onshore subthermocline rectification flow, eddies, Rossby waves, and filaments. Recent observations of a filament in the northern BUS based on high resolution hydrographic data was presented by Muller et al. (2013). The offshore transport associated with that filament was in the order of $3\,\mathrm{Sv}$ ($1\,\mathrm{Sv} = 10^6\,\mathrm{m}^3\,\mathrm{s}^{-1}$) and substantially larger than the integrated Ekman offshore transport. Studies on the characteristics of Rossby waves in the South Atlantic are rare. Reason et al. (1987) used a numerical model to investigate the properties of first mode annual-period baroclinic Rossby waves in the interior South Atlantic Ocean. The WSC maxima off the Namibian coast were identified to be a hot spot in the generation of long Rossby waves. The sea level variability and Rossby wave dynamics in the South Atlantic based on a few years of remotely sensed sea level data were analyzed by Le Traon and Minster (1993) and Witter and Gordon (1999). The impact of Rossby waves on the sea level and chlorophyll *a* concentration anomaly in the South Atlantic was studied by Gutknecht et al. (2010).

The current patterns in the BUS consist of locally forced (through wind stress) and remote (wave induced) signals. The impact of both on the longshore currents in the BUS is often discussed in the frame of positive temperature anomalies referred to as Benguela Niños. Those events are the largest scale and lowest frequency instance of variability observed in the BUS, Shillington et al. (2006). Positive temperature anomalies during the recent twenty years have been observed for instance in the years 1995 and 2001, e.g. Gammelsrød et al. (1998), Rouault et al. (2007). Using results from a coupled GCM, Richter et al. (2010) showed that meridional wind stress anomalies along the southwest African coast play a crucial role in the development of positive temperature anomalies in the BUS. Florenchie et al. (2003) found by the help of an ocean GCM that Benguela Niños are generated by specific wind stress events in the west-central equatorial Atlantic. Those events trigger coastal Kelvin waves produced by equatorial Kelvin waves that reach the eastern boundary and propagate poleward. They carry the signal alongshore as subsurface temperature anomalies into the BUS. Observations of coastally trapped waves in the southern BUS were presented by Schumann and Brink (1990).

There are two distinct central water masses in the BUS: the South Atlantic Central Water (SACW) of tropical origin and the Eastern South Atlantic Central Water (ESACW) which has its origin in the Cape region. The SACW is warm, oxygen poor but nutrient rich, whereas the ESACW is oxygen rich but nutrient depleted. The SACW is transported by the southward extension of the AC, that is the eastern branch of the Angola Gyre, into the BUS. Model studies and field data demonstrate the existence of SACW up to 27°S, Fennel et al. (2012). The ESACW is brought into the BUS by the northward directed coastal branch of the BC. The modeled mixing of different tracers representing the two central water masses is shown in figure 2.2. Mohrholz et al. (2008) showed that the oxygen concentration on the southwest African shelf depends highly on the water mass composition, i.e. the proportion of the two central water masses. This in turn depends on the strength and direction of the longshore currents. In austral summer, the poleward flow transports SACW into the northern BUS, whereas during winter, the water mass composition is dominated by ESACW, Mohrholz et al. (2008).

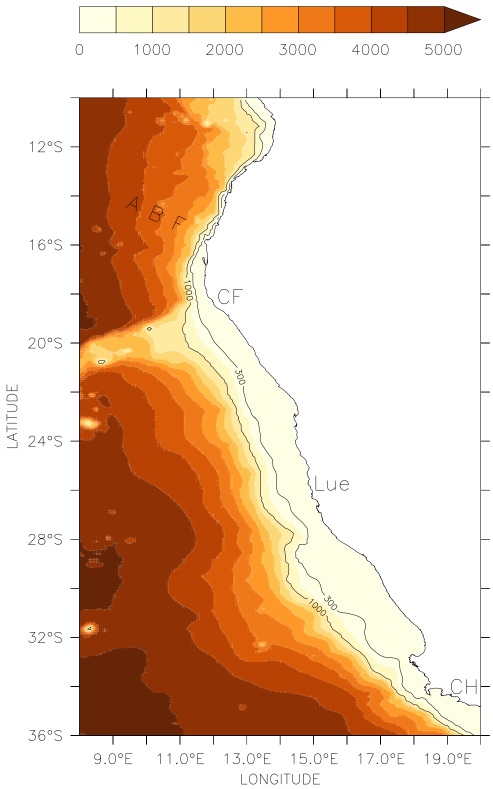

Figure 2.1. Map of the Benguela region that shows the approximate location of Cape Frio (CF), Lüderitz (Lue), Cape of Good Hope (CH), and the Angola-Benguela front (ABF). The color encodes the water depth [m] derived from the ETOPO5 data set. The 300 m and 1000 m depth contours are shown.

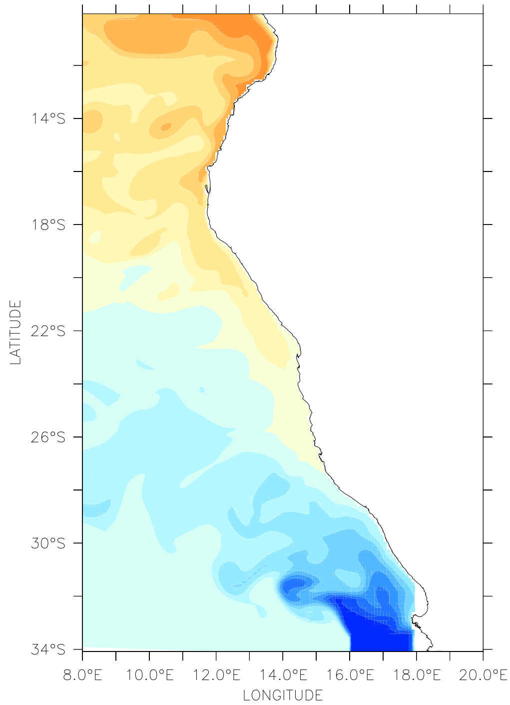

Figure 2.2. Modeled mixing of tracers injected in the equatorial undercurrent (representing SACW, orange) and near the Cape of Good Hope (ESACW, blue) after about 12 years of model integration, redrawn from Fennel et al. (2012).

2.1.3. Wind field

The BUS is characterized by coastal upwelling, Shillington (1998). The upwelling is a consequence of the divergence of the Ekman offshore transport which in turn is driven by the southeast trade winds. These winds are part of the anticlockwise circulation around the center of the South Atlantic anticyclone, also referred to as the St. Helena high pressure system, e.g. Lass and Mohrholz (2008), Shannon and Nelson (1996). The South Atlantic anticyclone is maintained throughout the year but undergoes seasonal shifts in position as the Intertropical Convergence Zone moves seasonally in latitude, Shannon (1985).

Since 2008, a climatology of ocean winds derived from spatially high resolved (0.25°) remotely sensed data for the period of September 1999 to October 2009 is available (Scattered Climatology of Ocean Winds, SCOW; downloaded at http://cioss.coas.oregonstate.edu/scow/), Risien and Chelton (2008). This data reveals very pronounced and persistent patterns in the meridional wind stress and the WSC in the Benguela region. Figure 2.3 shows the meridional wind stress derived from that climatology for the months of January and July. There are two regions of intensified meridional wind stress in the vicinity of the coast: the area off Cape Frio and off Lüderitz. Further more, the Cape region is

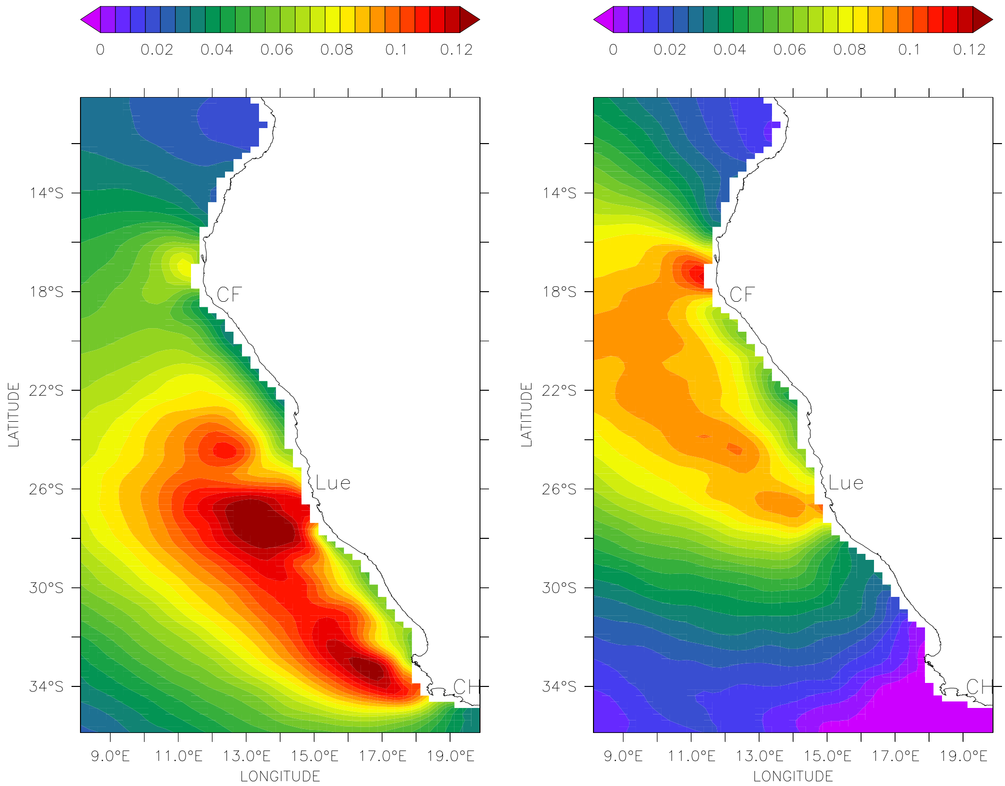

(a) January **(b)** July

Figure 2.3. Mean meridional wind stress [N m^{-2}] in the BUS for January and July derived from SCOW.

governed by strong meridional wind stress in January. Between these spots of enhanced wind stress, a band of less strong wind stretches along the coast. The mean meridional wind stress close to the coast is stronger in July than in January north of about 24°S and vice versa south of that parallel. The meridional wind stress decreases rapidly north of about 16°S that can be clearly seen in the climatological data for July. The mean meridional wind stress component increases with increasing offshore distance along the entire coast of the BUS. The resulting zonal gradient in the meridional wind stress contributes substantially to the very persistent negative (cyclonic) WSC found in the BUS. An estimated seasonal cycle of WSC in eastern boundary regions based on historical surface marine wind reports was first presented by Bakun and Nelson (1991). The authors described the negative WSC patterns in the BUS shaped as a wedge extending from about 20°S narrowing to the south. The meridional extent of the area with negative WSC migrated seasonally. It reached its most limited poleward extent in austral winter when it is not stretching further south than about 25°S. The mean WSC derived from the SCOW is shown in figure 2.4 for the month of January and July. The basic patterns coincide with those described by Bakun and Nelson (1991). A band of stronger, negative WSC extends from Cape Frio to the Cape region in January. In contrast, the area of mean negative WSC is more wedge like shaped in July with its smallest offshore extent at about 32°S. To the west of the area of negative WSC, a region of positive WSC attaches in both month.

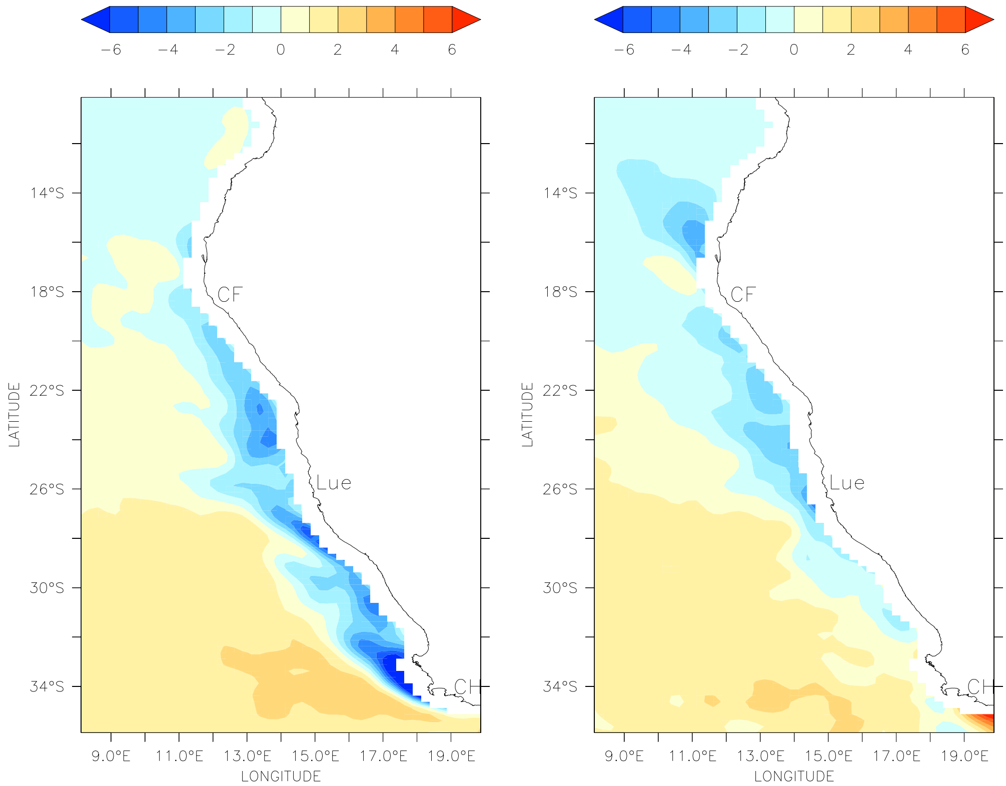

(a) January **(b)** July

Figure 2.4. Mean WSC [$10^{-4}\,\mathrm{N\,m^{-2}\,km^{-1}}$] in the BUS for January and July derived from SCOW.

The strength of the annual and semi-annual cycle of the wind forcing varies spatially within the BUS. Lass and Mohrholz (2008) calculated the Fourier coefficients of the annual and semi-annual component of the meridional wind stress from remote sensing data in the South Atlantic. They found that the annual cycle is very exposed along the South African coast. In contrast, the semi annual cycle of the meridional wind stress is small compared to the annual mean except for a very limited area off Cape Frio. The monthly mean meridional wind stress at two spots in the northern and southern BUS is presented in figure 2.5. The meridional wind stress component in the southern BUS has a maximum in austral spring (November) and a minimum in winter (June) with a distinct seasonal cycle. The wind stress in the northern BUS has a tendency to biannual maxima occurring in autumn (May) and spring (October) and a minimum in summer (January).

2.2. Theory of eastern boundary upwelling systems

There are many theoretical studies that address wind driven eastern boundary flows, among them Anderson and Gill (1975), Hurlburt and Thompson (1973), Suginohara and Kitamura (1984), McCreary and Chao (1985), and Philander and Yoon (1982). These studies use numerical models while analytical models are employed for instance in McCreary (1981) and Fennel (1999). Based on those studies, the response of an easterly bounded coastal ocean to a spatially homogeneous wind that is switched on at a certain time can be described as follows: in the first phase, immediately after

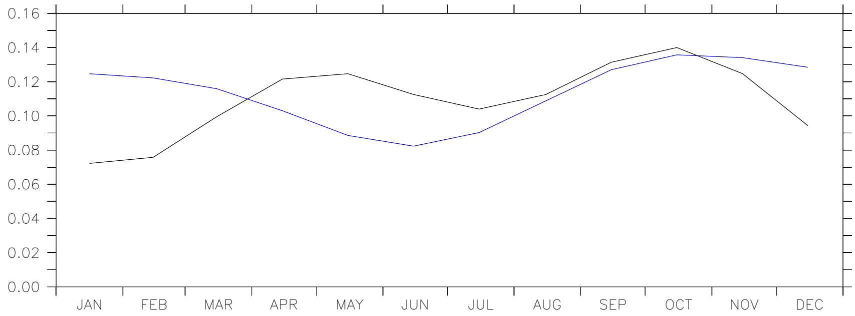

Figure 2.5. Monthly mean meridional wind stress [$\mathrm{N\,m^{-2}}$] in the northern BUS off Cape Frio (black) and in the southern BUS off Lüderitz (blue) derived from SCOW.

the onset of the wind, the wind drives an accelerating equatorward coastal jet (CJ) in the vicinity of the coast. As long as the winds are uniform in alongshore direction, the response in that phase is two-dimensional (independent of the longshore coordinate), Philander and Yoon (1982). Hence, the upwelling at the coast is fed into the Ekman offshore transport. A second phase is introduced by the arrival of Kelvin waves which are excited at the edges of the wind band and run poleward trapped by the coast. After a time span the Kelvin waves need to reach a certain location in the forced area, the acceleration of the CJ and the upwelling is stopped at this spot. Moreover, these waves introduce a poleward undercurrent (PUC). The wind stress is now balanced by an alongshore pressure gradient, and the Ekman rectification flow supplies the PUC. Since Kelvin waves stop the upwelling, only temporal variations of the wind field can excite new upwelling events, Fennel (1999). In reality, coastline irregularities, such as capes and bays, generate Kelvin waves in a manner similar to the longshore wind stress variability, Crépon et al. (1984). If the spherical shape of the earth is considered, the response is modified by the β-effect. The final stage to establish equilibrium conditions is now associated with the dispersion of the coastal currents into Rossby waves, Philander and Yoon (1982).

The response of the coastal ocean becomes even more complex if spatial and temporal distributions of wind stress over the upwelling region are considered. Several studies have shown that the existence of a WSC significantly alters the coastal circulation and strongly affects the upwelling as well as the longshore velocity, e.g. Hurlburt and Thompson (1973), McCreary and Chao (1985). Using a numerical model on the northern hemisphere in the β-plane approximation, Hurlburt and Thompson (1973) found that positive WSC in the coastal upwelling zone reduces the surface jet and enhances the PUC. McCreary et al. (1987) indicated, using as well a numerical model on the β-plane, that WSCs might be a reason for surface currents against the local wind off California. Fennel and Lass (2007) and Fennel et al. (2012) showed that this effect can also be explained in the f-plane approximation. Contrary to coastal upwelling, WSC driven upwelling (through Ekman pumping) is not influenced by coastally trapped waves. This illustrates the special meaning of WSC patterns in upwelling systems since this mechanism is able to maintain upwelling independent of Kelvin waves. Hence, the existence and strength of the WSC may also influence biological processes as well as the large scale ocean circulation. Rykaczewski and Checkley (2008) found that the production of Pacific sardine varies with the strength of the WSC over the past six decades in the California Current Ecosystem. Kanzow et al. (2010) argued that the seasonal varying strength of the WSC induced Ekman pumping on the eastern boundary of the Atlantic may be the reason for seasonal fluctuations of the Atlantic Meridional Overturning Circulation.

3. Analytical modeling of the Benguela upwelling system

Although analytical models are often highly idealized to ensure their tractability, they are well suited for studying principle physical processes. Most realistic simulations of the oceans circulation, however, can be achieved by advanced numerical models based on the full set of primitive equations.

As an eastern boundary upwelling system, the BUS is well suited for analytical modeling. The prevailing winds are basically meridional and the BUS is located at small latitudes but sufficiently far away from the equator. In order to design the analytical model appropriately, it is necessary to examine typical temporal and spatial scales of the system. This is done in the next section before the response of the BUS to a switch-on wind (on the f-plane) and a seasonally varying wind (on the β-plane) is derived.

3.1. Temporal and spatial scales

3.1.1. Temporal scales

An example of a time series of the meridional wind speed off the Namibian coast derived from remote sensing data is shown in figure 3.1. The data reveals wind fluctuations with periods of roughly ten to 14 days that can be considered as a sudden switch-on of the wind superimposing a constant wind field. The ocean responses with a variety of different waves to such wind pulses. The dispersion

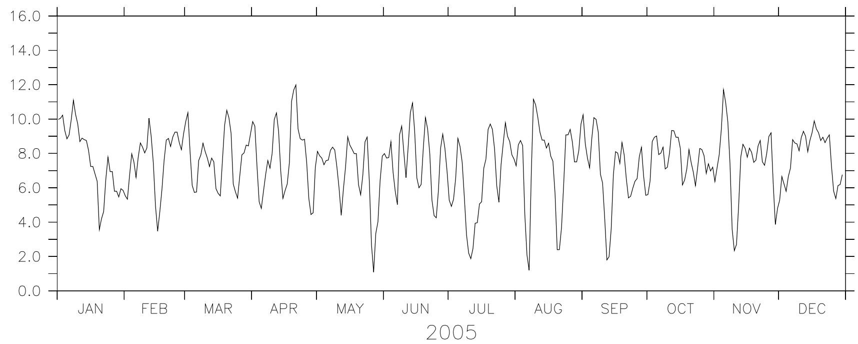

Figure 3.1. Exemplary time series of the meridional wind speed component [m s^{-1}] at 12°E, 22°S for the year 2005 derived from remote sensing data.

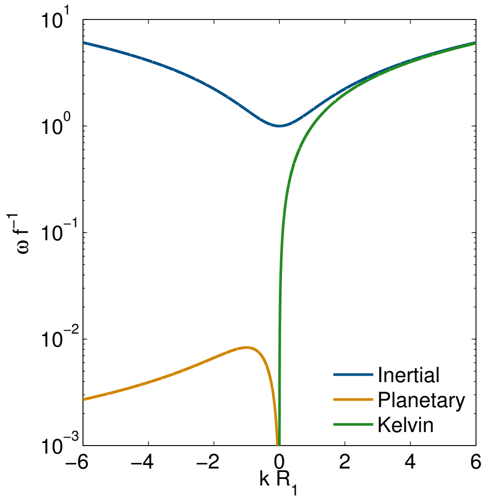

Figure 3.2. Dispersion relation of inertial waves, Kelvin waves, and planetary waves (Rossby waves). Note the logarithmic scale on the axis of ordinates.

relation of some of these waves is shown in figure 3.2. Inertial waves exist only for frequencies above the inertial frequency f. This frequency corresponds to an inertial period of roughly 30 hours in the BUS. Between internal and planetary waves (Rossby waves) exists a large spectral gap in the mid-latitudes. Planetary waves occur only below a critical frequency $\omega_c = \frac{R_n \beta}{2}$, e.g. Gill (1982), which corresponds to a period of about 150 days in the BUS. Kelvin waves, however, are non-dispersive and exist at all frequencies and wavelengths. They are a substantial part of the response to wind forcing as they adjust equilibrium conditions to the coastal ocean. The time scale of this adjustment process is the time Kelvin waves need to cross the wind band. This temporal scale can be estimated by

$$T_k = \frac{a}{c_n}.$$

Here, a is the length of the wind band and $c_n = \frac{NH}{n\pi}$ is the phase speed of Kelvin waves that is proportional to the water depth H and the Brunt-Väisälä frequency (BVF) N in the case of vertically constant stratification, see section 3.2.2. Assuming a length of the wind band of 1000 km and a first mode phase speed of $c_1 = 2\,\mathrm{m\,s^{-1}}$, it takes about 58 days for the ten gravest modes to cross the wind band.

The temporal scale for the geostrophic adjustment of the currents through inertial waves is roughly the inertial period. The time scale of Kelvin waves to cross the wind band is about ten times greater than the inertial period and well below the critical period of Rossby waves. The geostrophic adjustment of the ocean to new wind events happens therefore very fast compared to the adjustment by Kelvin waves. Rossby waves, however, do not play a role on that time scale. Hence, the adjustment process through inertial waves is neglected in the analytical model. The response to a switch-on wind is studied using an analytical model operating in a spectral band covering the sub-inertial domain above the critical frequency of Rossby waves. The response of the BUS to a switch-on wind using an analytical model in the f-plane approximation is derived and discussed in the next section.

In contrast to the response on times scales of a few ten days, upwelling on a seasonal time scale will be considerably influenced by the β-effect because the seasonal time scale exceeds the critical period of Rossby waves. The response of the coastal ocean to a seasonal varying wind stress using the β-plane approximation is presented and discussed in section 3.4.

3.1.2. Spatial scales

The Rossby Radius is an important length scale and the typical offshore scale of CJs in upwelling systems. In analytical models using an idealized eddy viscosity approach, friction is assumed to be inverse proportional to the Rossby Radius, e.g. Fennel (1999). The n-th mode Rossby Radius is calculated by

$$R_n = \frac{c_n}{f}.$$

Another important characteristic of the phase speed c_n becomes apparent. Additionally to the temporal scale (through the travel time of Kelvin waves), the phase speed c_n determines a spatial scale by the Rossby Radius R_n.

Maps showing the barotropic (external) and the first baroclinic (internal) Rossby Radius in the South Atlantic were presented by Houry et al. (1987). The external (first internal) Rossby Radius ranges from 5000 km (60 km) around the area of Cape Frio to less than 1000 km (20 km) in the Cape region. The decrease of the Rossby Radius with increasing latitude is certainly due to the β-effect. Due to the cross-shelf gradient of the water depth H (that is mirrored in the phase speed, see above), a cross-shelf gradient of the Rossby Radius may exist. Hence, the Rossby Radii on the shelf are smaller than in the interior Atlantic.

3.2. The model ocean

3.2.1. The model configuration

We consider an ocean on the southern hemisphere of constant depth H that is bounded to the east by a north-south stretching straight coast idealized as a vertical wall. The coast is located along the y-axis, i.e. $x = 0$. The model ocean is infinite to the north, south, and west. A sketch of the analytical model domain is shown in figure 3.3

To include frictional effects, the model uses a linear friction rate often referred to as Rayleigh friction. This friction allows to obtain tractable analytical solutions and helps to highlight the importance of friction for the dynamical balances of the oceans response to wind forcing, Fennel (1999). The background stratification of the model ocean is assumed to be constant, and the wind forcing enters the ocean as a volume force evenly distributed over a mixed layer.

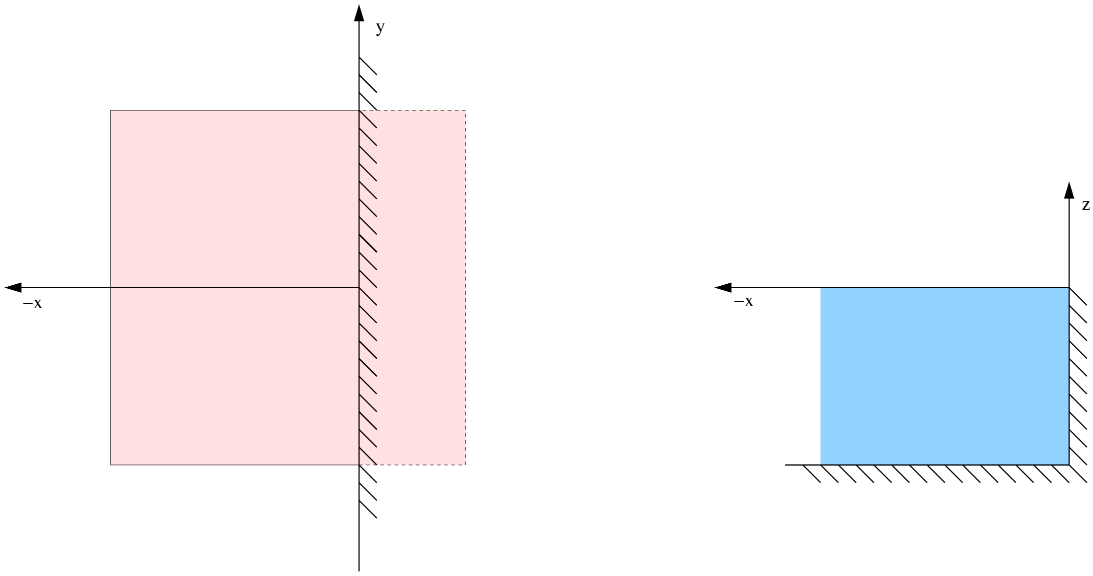

Figure 3.3. Sketch of the analytical model domain. The model is bounded to the east by a coast idealized as a vertical wall. The bottom is assumed to be flat. The forced area is shaded in the left panel. Its position and shape can be adjusted, see section 3.3.2.

3.2.2. The model equations

The model is based on the linear, hydrostatic Boussinesq equations for an ocean on the southern hemisphere that is forced only in meridional direction, see e.g. Fennel and Lass (1989),

$$(\partial_t + r)\, u + fv + \partial_x p = 0, \tag{3.1a}$$

$$(\partial_t + r)\, v - fu + \partial_y p = Y, \tag{3.1b}$$

$$\partial_z\, (\partial_t + r)\, p + N^2 w = 0, \tag{3.1c}$$

$$\partial_x u + \partial_y v + \partial_z w = 0. \tag{3.1d}$$

Here u, v, and w are the zonal (cross-shore), meridional (alongshore), and vertical current components. Further, p is the perturbation pressure divided by the density, f is the magnitude of the Coriolis parameter, r is a linear friction rate, and N was the BVF. The wind forcing in meridional direction is represented by Y. The symbols ∂_x, ∂_y, ∂_z, and ∂_t denote partial derivatives with respect to the zonal, meridional, vertical, and time coordinate.

To complete the system of equations (3.1), boundary conditions on the surface and the bottom as well as on the eastern boundary and far away from the coast are needed. We choose them to be on the zonal velocity u,

$$u(x = 0) = 0 \quad \text{and} \quad u(-\infty) = 0, \tag{3.2}$$

i.e. there is now flow through the eastern boundary and the zonal velocity far away from the forced area shall vanish. The vertical boundary conditions on w read

$$w(z=0) = \frac{1}{g}\left(\partial_t + r\right)p \quad \text{and} \quad w(-H) = 0. \tag{3.3}$$

They state that sea level changes are mirrored in the vertical velocity and that there is no flow through the bottom.

The technique of solving the linear, hydrostatic Boussinesq equations analytically is described in detail in Fennel and Lass (1989). The basic idea is the separation of the vertical coordinate in the equations (3.1) by expanding the dynamical quantities u, v, w, Y, and p into a series of vertical eigenfunctions,

$$\phi(x,y,z,t) = \sum_{n=0}^{\infty} \phi_n(x,y,t)F_n(z). \tag{3.4}$$

These vertical eigenfunctions F_n's are then subject to the vertical eigenvalue problem

$$\left(\boldsymbol{Z} + \lambda_n^2\right) F_n(z) = 0 \tag{3.5}$$

that rises from the combination of equation (3.1c) and (3.1d). The operator $\boldsymbol{Z}$ is defined as

$$\boldsymbol{Z} := \partial_z \frac{1}{N(z)^2} \partial_z.$$

The vertical boundary conditions for $F_n(z)$ follow from (3.3) and (3.1c) and read

$$\partial_z F_n(0) + \frac{N^2(0)}{g} F_n(0) = 0 \quad \text{and} \quad \partial_z F_n(-H) = 0.$$

The vertical eigenvalue problem (3.5) can not be solved analytically in general as it depends on the vertical structure of the BVF $N(z)$. Assuming a constant profile for N simplifies the solution of the vertical eigenvalue problem to

$$F_0 \approx \frac{1}{\sqrt{H}} \quad \text{and} \quad \lambda_0 = \frac{1}{\sqrt{gH}} \quad \text{for} \quad n = 0$$

and

$$F_n(z) = \sqrt{\frac{2}{H}} \cos\left(\frac{n\pi z}{H}\right) \quad \text{and} \quad \lambda_n = \frac{n\pi}{NH} \quad \text{for} \quad n \geq 1.$$

Note that $\lambda_n = c_n^{-1}$ is the inverse phase speed of Kelvin waves, and hence, the n-th mode Rossby Radius becomes $R_n = \lambda_n^{-1} f^{-1}$.

3.3. Response to a switch-on wind on the f-plane

3.3.1. Formal solution

A formal solution of the oceans response based on the equations (3.1) has been presented in Fennel et al. (2012). Its derivation is outlined in this subsection. After expansion into vertical eigenfunctions of the set (3.1) and Fourier transformation (FT) w.r.t. y and t,

$$\Psi(\kappa,\omega) = \int_{-\infty}^{\infty} \Psi(y,t) e^{-i\omega t + i\kappa y} \frac{dt}{2\pi}\frac{dy}{2\pi}, \tag{3.6}$$

where Ψ stands for the quantities u, v, w, p, and Y, an equation for the zonal velocity u_n can easily be derived,

$$\partial_x^2 u_n - \alpha_n^2 u_n = \left(\frac{i\kappa}{i\varpi} + \lambda_n^2 f\right) Y_n. \tag{3.7}$$

Here, $\alpha_n^2 = \kappa^2 + R_n^{-2} - \lambda_n^2 \varpi^2$ and $\varpi = \omega + ir$. A solution for the zonal velocity u_n is found applying the technique of Green's function to the inhomogeneous, linear, second order differential equation (3.7). The Green's function obeys

$$\partial_x^2 G_n(x,x') - \alpha_n^2 G_n(x,x') = \delta(x - x'). \tag{3.8}$$

The solution of this equation is derived elsewhere, e.g. Fennel and Lass (1989). It reads

$$G_n(x,x') = \frac{1}{2\alpha_n}(e^{\alpha_n(x+x')} - e^{-\alpha_n|x-x'|}). \tag{3.9}$$

In the frame of the β-plane approximation, equation (3.7) would be completed by the term $-\frac{\beta}{i\varpi}\partial_x u_n$. Furthermore, (3.9) changes to

$$G_n(x,x') = e^{-\frac{i\beta}{2\varpi}(x-x')} \frac{1}{2\alpha_n}(e^{\alpha_n(x+x')} - e^{-\alpha_n|x-x'|}). \tag{3.10}$$

The formal solution of the oceans response on the f-plane according to Fennel et al. (2012) is

$$u_n(x,\kappa,\omega) = \frac{i\kappa}{i\varpi} G_n * \partial_{x'} Y_n + \frac{1}{f} R_n^{-2} G_n * Y_n, \tag{3.11a}$$

$$v_n(x,\kappa,\omega) = -\frac{1}{i\varpi}\partial_x G_n * \partial_{x'} Y_n - \lambda_n \frac{-i}{\lambda_n \varpi + \kappa} \frac{1}{R_n} e^{\frac{x+x'}{R_n}} * Y_n, \tag{3.11b}$$

$$p_n(x,\kappa,\omega) = \frac{f}{i\varpi} G_n * \partial_{x'} Y_n + \frac{-i}{\lambda_n \varpi + \kappa} \frac{1}{R_n} e^{\frac{x+x'}{R_n}} * Y_n. \tag{3.11c}$$

The long wave approximation (LWA), i.e. $\kappa R_n \ll 1$, has been applied to the Green's function for small frequencies, i.e. $\omega \approx 0$, when deriving the Kelvin wave poles $\kappa = -\lambda_n \varpi$ in the set (3.11).

Expressions like $G_n * Y_n$ denote convolution integrals of the Green's function with the wind forcing function,

$$G_n * Y_n = \int_{-\infty}^{0} G_n(x, x')\, Y_n(x')\, dx'.$$

The set of equations (3.11) represents a formal solution of the oceans response depending on the meridional wind forcing function Y_n and the involved parameters. Both are specified in the next subsection.

3.3.2. Forcing function and parameter choices

Since the prevailing winds in the BUS are directed alongshore the model is forced by a meridional wind only,

$$Y(x, y, z, t) = \frac{v_*^2}{H_{\mathrm{mix}}} \theta(z + H_{\mathrm{mix}}) T(t) Q(y) \Pi(x). \tag{3.12}$$

The wind varies in both meridional and zonal direction. Moreover, the wind is considered to enter the ocean as a volume force evenly distributed over an upper mixed layer of thickness H_{mix}. Here, the square of the friction velocity v_*^2 that is proportional to the meridional wind stress component τ_y was introduced. The model wind is switched on at a certain time $t = 0$ being constant hereafter,

$$T(t) = \Theta(t). \tag{3.13}$$

The shape of the forcing functions $\Pi(x)$ and $Q(y)$ follows observations based on remotely sensed data. Figure 3.4 presents a zonal section of the meridional wind stress along 23°S for the months of January and July. A wind maximum that is closer to the coast in January than in July is clearly observed. Up to a distance of 600 km to the coast, both wind profiles can be approximated by a cosine function of the type

$$\Pi(x) = \theta(x + L + l) \cos(b\,(x + l)) \tag{3.14}$$

where $b = \frac{\pi}{2L}$ controls the wave length of the cosine function. The location of the wind maximum is determined by the parameter l that is in the range of $0 \leq l \leq L$. The distance from the coast to the offshore edge of the wind band is $L + l$. Typical values for these parameters derived from observations are in the range of 280 km $\leq l \leq$ 410 km and 330 km $\leq L \leq$ 600 km. Unless otherwise stated, we use a value of $L = 500$ km which lies well between the observed ones for January and July. The value of l is varied throughout the study in order to investigate its influence, i.e. the strength of the wind stress and WSC near the coast, on the currents response. It is worth noting that the cosine approach takes into account the phase opposition of wind stress and WSC in the northern BUS.

Two alongshore profiles of the mean meridional wind stress, one in the vicinity of the coast and the other located two degrees offshore, are shown in figure 3.5 for July. The offshore located profile has a dome-shaped structure with low wind stress south of about 32°S and north of about 12°S. The inshore profile reveals two distinct wind peaks that compare to the wind maxima off Cape Frio and Lüderitz

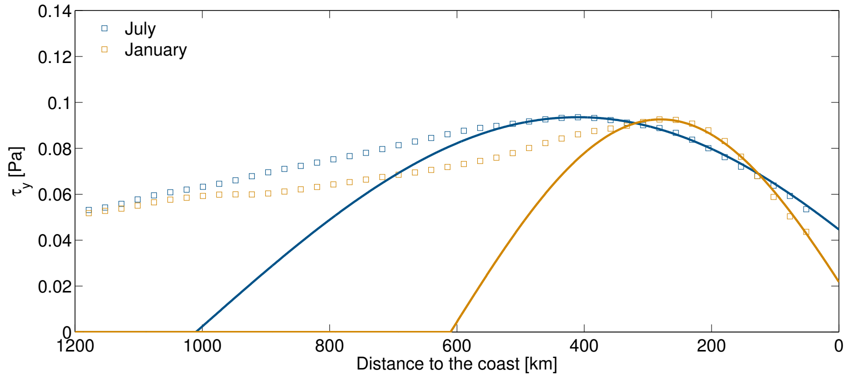

Figure 3.4. Zonal profiles of the mean meridional wind stress derived from the climatology SCOW (squares) compared to the idealized wind forcing function $\Pi(x)$ according to equation (3.14) (lines) for January and July at 23°S . The wind forcing parameters are chosen to be l = 280 km (l = 410 km) and L = 330 km (L = 600 km) for January (July).

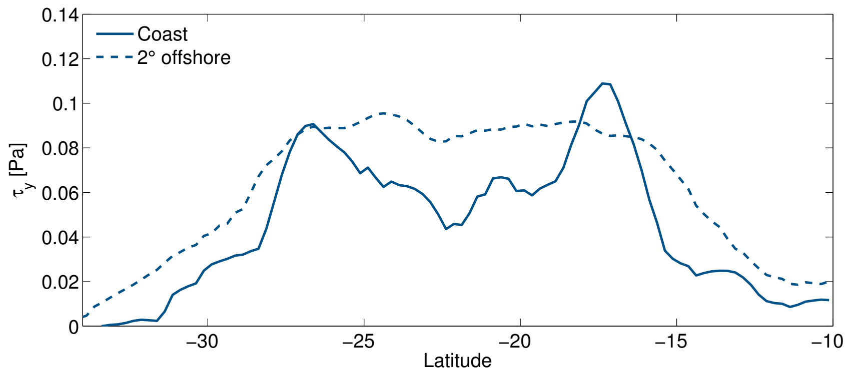

Figure 3.5. Alongshore profile of the mean meridional wind stress derived from SCOW in the vicinity of the coast and two degrees offshore for July.

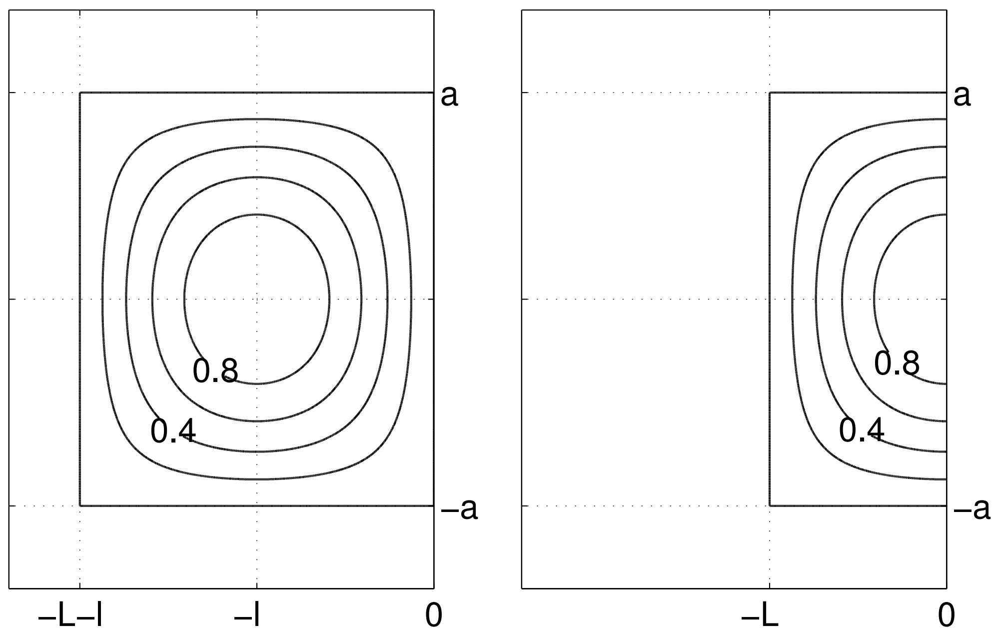

(a) l=500 km

(b) l = 0 km

Figure 3.6. Spatial shape of the analytical forcing function $Q(y)\Pi(x)$ for two different values of the parameter l. The contour interval is 0.2.

shown in figure 2.3. Following the remotely sensed data of the meridional wind stress, we choose a meridional wind profile that is symmetric and centered around the x-axis,

$$Q(y) = \theta(a - |y|)\cos(\kappa_0 y). \tag{3.15}$$

Here, $\kappa_0 = \frac{\pi}{2a}$ controls the wave length of the cosine function and $2a$ is the meridional extent of the wind band. In this model, we choose $a = 500\,\mathrm{km}$. The spatial shape of the wind forcing is presented in figure 3.6 for two different values of the parameter l.

The FT of the meridional wind forcing (3.12) w.r.t. y and t and expansion into vertical modes gives

$$Y_n(x,\kappa,\omega) = \frac{v_*^2}{h_n} T(\omega) Q(\kappa) \Pi(x) \tag{3.16}$$

where

$$\frac{1}{h_0} = \sqrt{\frac{1}{H}} \quad \text{for} \quad n = 0$$

and

$$\frac{1}{h_n} = \sqrt{\frac{2}{H}} \frac{\sin(\frac{n\pi}{H} H_{\mathrm{mix}})}{\frac{n\pi}{H} H_{\mathrm{mix}}} \quad \text{for} \quad n \geq 1.$$

The FT of $T(t)$ yields

$$T(\omega) = \frac{i}{\omega + i\epsilon} \quad \text{with} \quad \epsilon \to +0. \tag{3.17}$$

The magnitude of the Coriolis parameter is $f = 6 \cdot 10^{-5}\,\text{s}^{-1}$, and the friction parameter $r = 0.02f$. The square of the friction velocity is $v_*^2 = 0.8\,\text{cm}^2\,\text{s}^{-2}$ which represents a mean meridional wind stress of $\tau_y \approx 0.8\,\text{N}\,\text{m}^{-2}$. The water depth is $H = 1000\,\text{m}$ and the mixed layer depth $H_{\text{mix}} = 20\,\text{m}$. The first internal Rossby Radius is chosen to be $R_1 = 50\,\text{km}$ as long as otherwise stated. A comprehensive list of the chosen parameters involved in the analytical f-plane model is given in table A.1 in the appendix A.

3.3.3. Calculation of the convolution integrals

In order to calculate the response of the coastal ocean we need to estimate the convolution integrals $R_n^{-2} G_n * \Pi$, $G_n * \partial_{x'} \Pi$, and $\frac{1}{R_n} e^{\frac{x+x'}{R_n}} * \Pi$ in the formal solution (3.11). The detailed calculation of these integrals is presented in the appendix B.1. They read on the f-plane

$$
\begin{aligned}
A_n(x,\kappa,\omega) &:= R_n^{-2} G_n(x,x') * \Pi(x') \\
&= \frac{R_n^{-2}}{\alpha_n^2 + b^2} \left(e^{\alpha_n x} \cos(bl) + \frac{b}{2\alpha_n} \left(e^{\alpha_n (x-L-l)} - e^{-\alpha_n |x+L+l|} \right) - \Pi(x) \right), \qquad (3.18) \\
B_n(x,\kappa,\omega) &:= G_n(x,x') * \partial_{x'} \Pi(x') \\
&= \frac{1}{\alpha_n^2 + b^2} \left(-e^{\alpha_n x} b \sin(bl) - \frac{b}{2} \left(e^{\alpha_n (x-L-l)} - \operatorname{sign}(x+L+l) e^{-\alpha_n |x+L+l|} \right) - \partial_x \Pi(x) \right), \qquad (3.19) \\
C_n(x) &:= \frac{1}{R_n} \Pi(x) * e^{\frac{(x+x')}{R_n}} \\
&= \frac{1}{1 + R_n^2 b^2} \left(e^{\frac{x}{R_n}} \left(\cos(bl) + b R_n \sin(bl) \right) + b R_n e^{\frac{(x-L-l)}{R_n}} \right). \qquad (3.20)
\end{aligned}
$$

The convolution integrals A_n and B_n cover the oceans response at all time scales and wave lengths. The wave numbers b and κ in the denominator of these integrals suggests an impact of the wind scales on the currents response at all frequencies. Before we derive a solution in the subinertial frequency domain, we therefore investigate the response in the near-inertial frequency range.

3.3.4. Near-inertial response

The response of the coastal ocean in the near-inertial frequency domain includes inertial oscillations and inertial waves. We chose exemplary for the near-inertial response the term $f^{-1} R_n^{-2} G_n * Y_n$ in (3.11a) and neglect all exponential terms in the convolution integral (3.18). These exponential terms correspond to inertial waves that are excited at the boundary of the model domain and propagate westward. Behind the waves, the geostrophic balance is established, see e.g. Kundu et al. (1983). We consider only contributions of poles like

$$
u_n \propto -\frac{v_*^2}{h_n} \frac{1}{f R_n^2} \Pi(x) \iint \frac{1}{\alpha_n^2 + b^2} Q(\kappa) T(\omega) e^{i\kappa y - i\omega t} \frac{d\kappa}{2\pi} \frac{d\omega}{2\pi}. \qquad (3.21)
$$

The inverse FT w.r.t. κ leads to the calculation of the integral

$$\int Q(\kappa)\frac{1}{\kappa^2+\zeta_n^2}e^{i\kappa y}\frac{d\kappa}{2\pi} \tag{3.22}$$

where $\zeta_n^2 := \lambda_n^2 f^2 - \lambda_n^2\overline{\omega}^2 + b^2$. The above integral is calculated with the help of the convolution theorem

$$\mathcal{F}(f(\kappa)\cdot g(\kappa)) = \int f(y')g(y-y')dy'$$

where we choose $f(y') = Q(y')$. This leads to the calculation of the integral

$$\int \frac{1}{\kappa^2+\zeta_n^2}e^{i\kappa y}\frac{d\kappa}{2\pi} = \frac{1}{2\zeta_n}\left(\Theta(y)e^{-\zeta_n y} + \Theta(-y)e^{\zeta_n y}\right) = \frac{1}{2\zeta_n}e^{-\zeta_n|y|}$$

where Jordan's lemma together with the Residue theorem has been applied. We find for (3.22)

$$\int Q(\kappa)\frac{1}{\kappa^2+\zeta_n^2}e^{i\kappa y}\frac{d\kappa}{2\pi} = \frac{1}{\zeta_n^2+\kappa_0^2}\left[Q(y) + \frac{\kappa_0}{\zeta_n}\frac{1}{2}\left(e^{-\zeta_n|y+a|} + e^{-\zeta_n|y-a|}\right)\right]. \tag{3.23}$$

The part of the response depending on the meridional coordinate consists of the sum of the wind forcing function $Q(y)$ and a rectification around the northern and southern boundary of the wind field,

$$M_n(y) := Q(y) + S_n(y)$$

with

$$S_n(y) := \frac{\kappa_0}{\zeta_n}\frac{1}{2}\left(e^{-\zeta_n|y+a|} + e^{-\zeta_n|y-a|}\right).$$

This rectification is small in general as will be shown in section 3.3.5. In the near-inertial frequency domain, the exponential terms in (3.23) correspond to inertial waves propagating meridionally away from the boundaries of the wind band, i.e. at $y = \pm a$, and involve branch points at $\zeta_n = 0$. Once more, we neglect the wave contribution but consider the first term in (3.23) including the pole $\zeta_n^2 = -\kappa_0^2$. The inverse FT w.r.t. ω leads to the calculation of the integral

$$\int \frac{\lambda_n^{-2}}{\overline{\omega}^2-\Delta_n^2}\frac{i}{\omega+i\epsilon}e^{-i\omega t}\frac{d\omega}{2\pi} = \Theta(t)\frac{-1}{\lambda_n^2(r^2+\Delta_n^2)}\left(1 - e^{-rt}\left(\frac{r}{\Delta_n}\sin(\Delta_n t) - \cos(\Delta_n t)\right)\right). \tag{3.24}$$

Here, the frequency

$$\Delta_n = f\sqrt{1+R_n^2(b^2+\kappa_0^2)}$$

was introduced. This frequency corresponds to the frequency of inertial oscillations. It is enhanced by the wave numbers of the forcing field b and κ_0 and becomes mode dependent through the Rossby Radius R_n. Such a frequency enhancement is often referred to as "blue shift". This phenomenon is known from studies of the oceans response to moving fronts where the "blue shift" depends on the ratio of the inertial wave phase speed and the speed of the moving front, e.g. Kundu and Thomson (1985), Fennel and Lass (1989). The frequency Δ_n is presented in figure 3.7 as a function of the zonal wind scale L and the Rossby Radius R_n. In general, the zonal scale of the wind forcing exceeds the Rossby Radius, i.e. $R_n^2 b^2 \ll 1$. Therefore, the frequency shift is weak and the frequency Δ_n is

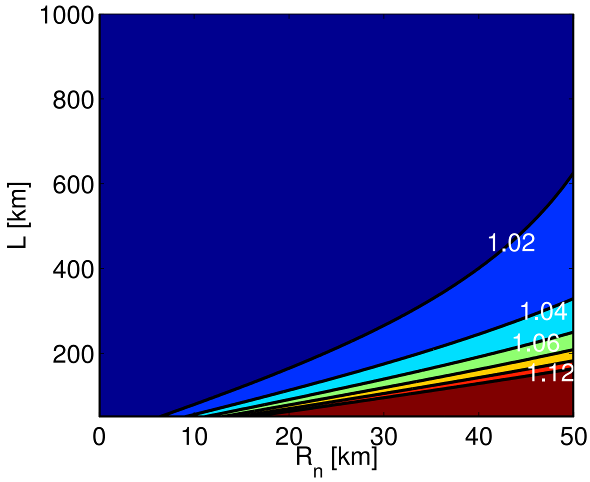

Figure 3.7. Inertial wave frequency Δ_n normalized by f as a function of the zonal wind scale L and the Rossby Radius R_n.

still near-inertial. But the "blue shift" becomes more apparent if the Rossby Radius R_n increases and the zonal scale of the wind band L decreases. For typical values of $R_1 = 50\,\text{km}$ and $L = 500\,\text{km}$, the inertial frequency is $\Delta_1 \approx 1.02\, f$. If the zonal scales of the wind band are further reduced the inertial frequency increases to $\Delta_1 \gtrsim 1.08\, f$ for $L \leq 200\,\text{km}$.

Using (3.24), the near-inertial response of the zonal velocity apart from boundary effects can be written as

$$u_n = -\frac{1}{f} Y_n \frac{1}{(1 + R_n^2(b^2 + \kappa_0^2))(1 + r^2 \Delta_n^{-2})} \left(1 - e^{-rt} \left(\frac{r}{\Delta_n} \sin(\Delta_n t) + \cos(\Delta_n t)\right)\right).$$

Noting that $R_n^2(b^2 + \kappa_0^2) \ll 1$ and $r\Delta_n^{-1} \ll 1$, we find an approximate expression for the zonal velocity in the near-inertial frequency domain,

$$u_n(x, y, t) \approx -\frac{1}{f} Y_n(x, y, t) \left(1 - e^{-rt} \cos(\Delta_n t)\right).$$

The response consists of the Ekman flow overlayed by inertial oscillations with frequency Δ_n. Since these oscillations are mode dependent the vertical structure of the response is affected. The frequency is highest at the bottom which leads to an upward phase propagation, see Kundu and Thomson (1985).

The discussion of the near-inertial response is of course not complete because inertial waves were not considered. But the evaluation of the corresponding integrals is quite complicated and not the focus of this study.

3.3.5. Subinertial response

In order to derive the response in the subinertial frequency domain, we have to compute the contribution of the pole $\omega = 0$ arising from (3.17). Here, the denominator of the convolution integrals

(3.18) and (3.19) becomes $\alpha_n^2 + b^2 = \lambda_n^2 f^2 + \kappa^2 + b^2$ provided that $r \ll f$. It can be rewritten to $\kappa^2 + \zeta_n^2$ where $\zeta_n^2 := \lambda_n^2 f^2 + b^2$. For the inverse FT in A_n and B_n, we apply the LWA, i.e. $\kappa^2 \ll R_n^{-2}$, to the convolution integrals. However, contrary to Fennel et al. (2012), we apply the LWA only to the exponents, but we keep the poles $\kappa^2 = -\zeta_n^2$ in the convolution integrals and consider

$$A_n(x,\kappa) = \frac{R_n^{-2}}{\kappa^2 + \zeta_n^2}\left(e^{\frac{x}{R_n}} \cos(bl) + \frac{bR_n}{2}\left(e^{\frac{(x-L-l)}{R_n}} - e^{-\frac{|x+L+l|}{R_n}}\right) - \Pi(x)\right), \tag{3.25}$$

$$B_n(x,\kappa) = \frac{1}{\kappa^2 + \zeta_n^2}\left(-be^{\frac{x}{R_n}} \sin(bl) - \frac{b}{2}\left(e^{\frac{(x-L-l)}{R_n}} - \operatorname{sign}(x+L+l)e^{-\frac{|x+L+l|}{R_n}}\right) - \partial_x \Pi(x)\right). \tag{3.26}$$

A solution in the frequency domain can be derived by applying the inverse FT to the formal solution (3.11). These calculations are presented in the subsequent subsection.

Response in the frequency domain

The inverse FT of the formal solution for u_n, v_n, and p_n demands the calculation of the Fourier integrals

$$\int Q(\kappa)\frac{1}{\kappa^2 + \zeta_n^2} e^{i\kappa y} \frac{d\kappa}{2\pi} \tag{3.27}$$

and

$$\int Q(\kappa)\frac{i\kappa}{\kappa^2 + \zeta_n^2} e^{i\kappa y} \frac{d\kappa}{2\pi}. \tag{3.28}$$

The integral (3.27) has been calculated in the previous subsection, see equation (3.23). We found that the response depending on the meridional coordinate consists of the sum of the wind forcing function $Q(y)$ and a rectification around the northern and southern edge of the wind field denoted as

$$S_n(y) = \frac{\kappa_0}{\zeta_n}\frac{1}{2}\left(e^{-\zeta_n|y+a|} + e^{-\zeta_n|y-a|}\right).$$

Since the integral (3.28) is the derivative of the integral (3.27) w.r.t. y it simply amounts to

$$\frac{1}{\zeta_n^2 + \kappa_0^2}\partial_y M_n(y) = \frac{1}{\zeta_n^2 + \kappa_0^2}\left(\partial_y Q(y) + \partial_y S_n(y)\right) \tag{3.29}$$

where

$$\partial_y S_n(y) = \frac{\kappa_0}{2}\left(\operatorname{sign}(y+a)e^{-\zeta_n|y+a|} + \operatorname{sign}(y-a)e^{-\zeta_n|y-a|}\right).$$

Applying the LWA also to the denominator of the convolution integrals would lead to $S_n = 0$. Including the rectification S_n, the response becomes mode dependent. We find for the first baroclinic mode $S_1 \leq \frac{\kappa_0}{\zeta_1} \approx R_1\kappa_0 \approx 0.15$ with the maximum value at the northern and southern edge of the wind field. Thus, the absolute values of the baroclinic velocities and the pressure become slightly enhanced around the meridional boundaries of the wind field. The rectification in the middle of the wind band is negligible since the meridional extent of the wind band exceeds the meridional trapping

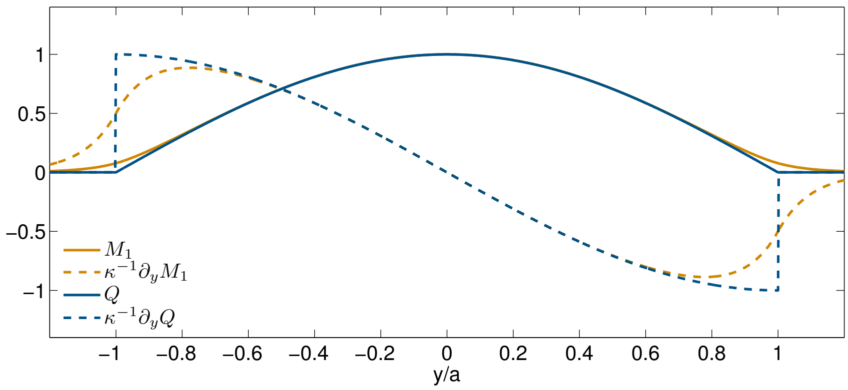

Figure 3.8. Comparison of the functions $Q(y)$ and $M_n(y)$ and $\kappa^{-1}\partial_y Q(y)$ and $\kappa^{-1}\partial_y M_n(y)$ for the first baroclinic mode.

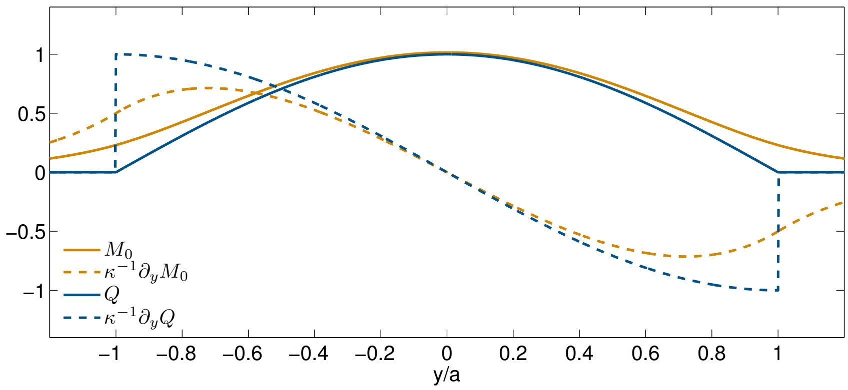

Figure 3.9. Same as figure 3.8 but for the barotropic mode. The meridional trapping scale in $S_0(y)$ is a tenth of the barotropic Rossby Radius R_0.

scale, i.e. $a \gg \zeta_n^{-1} = \frac{R_n}{\sqrt{b^2 R_n^2 + 1}} \approx R_n$. Remarkably, the zonal wave number of the wind band b determines the meridional trapping scale of the currents around the meridional boundaries of the forcing field. The shape of the functions $M_n(y)$ and $\kappa^{-1}\partial_y M_n(y)$ are compared to the function $Q(y)$ and $\kappa^{-1}\partial_y Q(y)$ in figure 3.8 for the first baroclinic mode. The difference between the forcing functions $Q(y)$ and the function $M_n(y)$ (or their derivatives) is small in the middle of the wind band, but the smoothing effect around the northern and southern borders is obvious.

The rectification for the barotropic mode is $S_0 \leq \frac{k_0}{\zeta_0} \approx 0.5$ and thus higher than for the baroclinic modes. Since the barotropic trapping scale exceeds the meridional scale of the chosen wind band, i.e. $\zeta_0^{-1} \approx R_0 > |y + a|$, the velocities in the middle of the wind band are enhanced by $S_0 \approx 0.2$. Therefore, including the term S_n in the solution would give preference to the barotropic mode. However, the barotropic Rossby radius depends highly on the water depth which is with $H = 1000\,\mathrm{m}$ chosen to be relatively large in this model. Anyway, reducing the barotropic trapping scale R_0 to a tenth of its original value keeps the correction $S_n \approx 0$ in the middle of the wind band, see figure 3.9. But the smoothing around the boundaries of the wind field is still ensured.

The inverse FT of the formal solution for v_n and p_n demands also the calculation of the Fourier integral

$$I_n(y,\omega) := \int \frac{-i}{\overline{\omega}\lambda_n + \kappa} Q(\kappa) e^{i\kappa y} \frac{d\kappa}{2\pi} \tag{3.30}$$

containing the Kelvin wave response. The calculation is presented in the appendix B.2, and the solution reads

$$\begin{aligned} I_n(y,\omega) = \frac{\kappa_0}{\lambda_n^2\overline{\omega}^2 - \kappa_0^2} \Big(\Theta(a-y) e^{i\lambda_n\overline{\omega}(a-y)} + \Theta(-a-y) e^{i\lambda_n\overline{\omega}(-a-y)} \\ -\Theta(a-|y|) \left(\frac{i\lambda_n\overline{\omega}}{\kappa_0} \cos(\kappa_0 y) + \sin(\kappa_0 y) \right) \Big). \end{aligned} \tag{3.31}$$

From the definition of the integral I_n, equation (3.30), follows immediately

$$Q(y) = (\partial_y + i\lambda_n\overline{\omega}) I_n(y,\omega). \tag{3.32}$$

Having carried out the inverse FT w.r.t. κ, the solution for the zonal and meridional velocity as well as for the pressure in the frequency domain can be summarized as follows:

$$u_n(x,y,\omega) = \frac{v_*^2}{h_n} T(\omega) \left(\frac{1}{i\overline{\omega}} B_n(x) \partial_y M_n(y) + \frac{1}{f} A_n(x) M_n(y) \right), \tag{3.33a}$$

$$v_n(x,y,\omega) = \frac{v_*^2}{h_n} T(\omega) \left(-\frac{1}{i\overline{\omega}} \partial_x B_n(x) M_n(y) - \lambda_n I_n(y,\omega) C_n(x) \right), \tag{3.33b}$$

$$p_n(x,y,\omega) = \frac{v_*^2}{h_n} T(\omega) \left(\frac{f}{i\overline{\omega}} B_n(x) M_n(y) + I_n(y,\omega) C_n(x) \right). \tag{3.33c}$$

The convolution integrals A_n and B_n read

$$A_n(x) = \frac{R_n^{-2}}{\kappa_0^2 + \zeta_n^2} \left(e^{\frac{x}{R_n}} \cos(bl) + \frac{bR_n}{2} \left(e^{\frac{(x-L-l)}{R_n}} - e^{-\frac{|x+L+l|}{R_n}} \right) - \Pi(x) \right), \tag{3.34}$$

$$B_n(x) = \frac{1}{\kappa_0^2 + \zeta_n^2} \left(-be^{\frac{x}{R_n}} \sin(bl) - \frac{b}{2} \left(e^{\frac{(x-L-l)}{R_n}} - \operatorname{sign}(x+L+l) e^{-\frac{|x+L+l|}{R_n}} \right) - \partial_x \Pi(x) \right). \tag{3.35}$$

The integral C_n is presented in (3.20). The response in the time domain is derived in the following subsection.

Response in the time domain

The inverse FT of the set (3.33) w.r.t. ω leads to the estimation of the integrals

$$\int \frac{1}{i\overline{\omega}} T(\omega) e^{-i\omega t} \frac{d\omega}{2\pi} = -\frac{\Theta(t)}{r} \left(1 - e^{-rt} \right) \tag{3.36}$$

and

$$J_n(y,t) := \int T(\omega) I_n(y,\omega) e^{-i\omega t} \frac{d\omega}{2\pi}.$$

From the definition of the integral J_n follows directly

$$(\partial_y - (\partial_t + r)\,\lambda_n)J_n(t,y) = Q(y)\Theta(t). \tag{3.37}$$

The detailed calculation of J_n is presented in the appendix B.2. The result is

$$\begin{aligned} J_n(y,t) = &\frac{\Theta(t)\Theta(a-|y|)}{\lambda_n r(1+\frac{\kappa_0^2}{r^2\lambda_n^2})}\left(\cos(\kappa_0 y) - \frac{\kappa_0}{r\lambda_n}\sin(\kappa_0 y) - e^{-rt}\Psi_n\left(y+\frac{t}{\lambda_n}\right)\right) \\ &+ \frac{\Theta(a-y)\Theta(t-\lambda_n(a-y))}{\lambda_n r(1+\frac{\kappa_0^2}{r^2\lambda_n^2})}\left(\frac{\kappa_0}{r\lambda_n}e^{-r\lambda_n(a-y)} + e^{-rt}\Psi_n\left(y+\frac{t}{\lambda_n}\right)\right) \\ &+ \frac{\Theta(-a-y)\Theta(t-\lambda_n(-a-y))}{\lambda_n r(1+\frac{\kappa_0^2}{r^2\lambda_n^2})}\left(\frac{\kappa_0}{r\lambda_n}e^{-r\lambda_n(-a-y)} - e^{-rt}\Psi_n\left(y+\frac{t}{\lambda_n}\right)\right) \end{aligned} \tag{3.38}$$

where

$$\Psi_n\left(y+\frac{t}{\lambda_n}\right) := \cos\left(\kappa_0\left(y+\frac{t}{\lambda_n}\right)\right) - \frac{\kappa_0}{r\lambda_n}\sin\left(\kappa_0\left(y+\frac{t}{\lambda_n}\right)\right)$$

was introduced for convenience. The quantity J_n describes the CJ and Kelvin wave dynamics (in the time domain) that is an important part of the oceans response to wind forcing. We elaborate on it when investigating the vertical currents. For the case of homogeneous wind stress in meridional direction, i.e. $Q(y) = 1$ and therefore $Q(\kappa) = \delta(\kappa)$, the integral $I_n = -\frac{i}{\varpi\lambda_n}$ and consequently the integral J_n converges to (3.36). The Kelvin waves vanish from the alongshore response that now basically consists of a jet that develops with time.

We summarize here the solution for the horizontal currents and the pressure in the time domain:

$$u_n(x,y,t) = \frac{v_*^2}{r\,h_n}\Theta(t)\left(-\left(1-e^{-rt}\right)\partial_y M_n(y)\,B_n(x) + r\,M_n(y)\frac{1}{f}A_n(x)\right), \tag{3.39a}$$

$$v_n(x,y,t) = \frac{v_*^2}{r\,h_n}\left(\Theta(t)\left(1-e^{-rt}\right)M_n(y)\partial_x B_n(x) - r\lambda_n J_n(y,t)C_n(x)\right), \tag{3.39b}$$

$$p_n(x,y,t) = \frac{v_*^2}{r\,h_n}\left(-\Theta(t)\left(1-e^{-rt}\right)f M_n(y)B_n(x) + rJ_n(y,t)C_n(x)\right). \tag{3.39c}$$

For consistency, the approximation $\zeta_n^2+\kappa_0^2 \approx R_n^{-2}+b^2$ is applied to the denominator of the convolution integrals A_n and B_n. As a result, these integrals achieve the same denominator as C_n, and we find

$$\begin{aligned} A_n(x) &= \frac{1}{1+b^2R_n^2}\left(\cos(bl)e^{\frac{x}{R_n}} + \frac{bR_n}{2}\left(e^{\frac{x-L-l}{R_n}} - e^{-\frac{|L+l+x|}{R_n}}\right) - \Pi(x)\right), \\ B_n(x) &= \frac{R_n^2}{1+b^2R_n^2}\left(-b\sin(bl)e^{\frac{x}{R_n}} - \frac{b}{2}\left(e^{\frac{x-L-l}{R_n}} - \mathrm{sign}(x+L+l)e^{-\frac{|x+L+l|}{R_n}}\right) - \partial_x\Pi(x)\right), \\ C_n(x) &= \frac{1}{1+R_n^2b^2}\left(\left(\cos(bl) + bR_n\sin(bl)\right)e^{\frac{x}{R_n}} + bR_ne^{\frac{x-L-l}{R_n}}\right). \end{aligned}$$

The calculation of the derivative $\partial_x B_n(x)$ in (3.39b) is straightforward,

$$\partial_x B_n(x) = \frac{bR_n}{1+R_n^2 b^2}\left(-e^{\frac{x}{R_n}}\sin(bl) - \frac{1}{2}\left(e^{\frac{x-L-l}{R_n}} + e^{\frac{-|x+L+l|}{R_n}}\right) + bR_n\Pi(x)\right).$$

The response depending on the meridional coordinate M_n in (3.39) is

$$M_n(y) = Q(y) + \frac{\kappa_0}{\zeta_n}\frac{1}{2}\left(e^{-\zeta_n|y+a|} + e^{-\zeta_n|y-a|}\right).$$

The derivative $\partial_y M_n$ and the function J_n was presented in (3.29) and (3.38), respectively.

The convolution integrals A_n, B_n, and C_n fulfill the relations

$$\partial_x A_n = R_n^{-1} C_n + R_n^{-2} B_n, \tag{3.40a}$$

$$\partial_x B_n = A_n - C_n + \Pi. \tag{3.40b}$$

Combining both equations gives

$$\partial_x^2 B_n - R_n^{-2} B_n = \partial_x \Pi, \tag{3.41}$$

$$R_n^2 \partial_x^2 A_n - A_n = \Pi. \tag{3.42}$$

Alternatively, these relations can be derived by multiplying (3.8) with $\partial_{x'} Y(x')$ or $Y(x')$, respectively, and integrating from $-\infty$ to 0 afterwards.

As the horizontal boundary conditions (3.2) demand, the convolution integrals A_n and B_n vanish at the coast and far offshore, i.e. at $x = 0$ and at $x \to -\infty$. In the case of zero WSC, i.e. $L \to \infty$ and consequently $b \to 0$, we find

$$A_n \to e^{\frac{x}{R_n}}\Pi(0) - \Pi(x),$$

$$B_n \to 0,$$

$$C_n \to e^{\frac{x}{R_n}}\Pi(0).$$

The equations (3.39) describe the response of the ocean for every single mode n. In order to gain a solution involving all modes, the mode summation according to (3.4) must be carried out. This is done by the help of numerical calculations where maximal mode numbers of $n_{\max} = 200$ for the cross-shore currents and $n_{\max} = 800$ for the longshore currents and the pressure were used.

Consistency of the solution

In the frame of the applied approximations, the equations (3.39) are a solution of the set

$$f v_n + \partial_x p_n = 0, \tag{3.43a}$$

$$(\partial_t + r)\, v_n - f u_n + \partial_y p_n = Y_n, \tag{3.43b}$$

$$\partial_x u_n + \partial_y v_n + \lambda_n^2 (\partial_t + r)\, p_n = 0. \tag{3.43c}$$

This system describes the oceans state after the adjustment by inertial waves. We point out that the presented response is an approximate solution of the set (3.43) as long as the rectification term S_n is included. Applying the LWA also to the denominator of the convolution integrals A_n and B_n would lead to $S_n = 0$. This procedure yields an exact solution of the set (3.43) as presented by Fennel et al. (2012). In that approach, however, the response of the zonal velocity is partly governed by the term $\partial_y Q$ due to the occurrence of the meridional wave number κ in equation (3.11a). This results in sharp edges at the boundaries of the wind band as shown by figure 3.8.

Another possibility of avoiding sharp edges in the response would be using an exponential function of the type $Q(y) \propto e^{-y^2}$ instead of a wind forcing that includes the Heaviside function. However, this would put the error function into play in the calculation of the integral (3.30). Therefore, we dismissed this option.

Vertical currents

The vertical velocity can be calculated from the pressure field by the help of equation (3.1c) that reads

$$w_n(x,y,t) = -\frac{1}{N^2}\partial_z (\partial_t + r)\, p_n(x,y,t).$$

Performing the mode summation

$$w(x,y,z,t) = -\frac{1}{N^2}\sum_{n=1}^{\infty} \partial_z F_n(z)\, (\partial_t + r)\, p_n(x,y,t)$$

gives

$$w(x,y,z,t) = v_*^2 \frac{H}{H_{\mathrm{mix}}} \sum_{n=1}^{\infty} \frac{2\lambda_n^2}{\pi^2 n^2} \sin\left(\frac{n\pi}{H} H_{\mathrm{mix}}\right) \sin\left(\frac{n\pi}{H} z\right) \cdot \left(-f M_n(y) B_n(x) \Theta(t) + (\partial_t + r)\, J_n(y,t) C_n(x)\right). \tag{3.44}$$

We neglect hereby the barotropic mode ($n = 0$) since it is diminished by the very fast barotropic Kelvin wave anyway. Further, we used

$$-\frac{1}{N^2}\partial_z F_n(z) = \frac{H\lambda_n^2}{n\pi}\sqrt{\frac{2}{H}} \sin\left(\frac{n\pi}{H} z\right)$$

and

$$\frac{1}{h_n} = \sqrt{\frac{2}{H}} \frac{\sin\left(\frac{n\pi}{H} H_{\text{mix}}\right)}{\frac{\pi n}{H} H_{\text{mix}}}.$$

The term $(\partial_t + r)\, J_n(y,t)$ in (3.44) can be estimated from (3.38), and we find

$$\begin{aligned}
(\partial_t + r)\, J_n(y,t) = & \frac{\Theta(t)\Theta(a-|y|)}{\lambda_n\left(1+\frac{\kappa_0^2}{r^2\lambda_n^2}\right)} \frac{\kappa_0}{r\lambda_n}\left(\frac{\lambda_n r}{\kappa_0}\cos(\kappa_0 y) - \sin(\kappa_0 y) + e^{-rt}\Phi_n\left(y+\frac{t}{\lambda_n}\right)\right) \\
& + \frac{\Theta(a-y)\Theta(t-\lambda_n(a-y))}{\lambda_n\left(1+\frac{\kappa_0^2}{r^2\lambda_n^2}\right)} \frac{\kappa_0}{r\lambda_n}\left(e^{-r\lambda_n(a-y)} - e^{-rt}\Phi_n\left(y+\frac{t}{\lambda_n}\right)\right) \\
& + \frac{\Theta(-a-y)\Theta(t-\lambda_n(-a-y))}{\lambda_n\left(1+\frac{\kappa_0^2}{r^2\lambda_n^2}\right)} \frac{\kappa_0}{r\lambda_n}\left(e^{-r\lambda_n(-a-y)} + e^{-rt}\Phi_n\left(y+\frac{t}{\lambda_n}\right)\right) \qquad (3.45)
\end{aligned}$$

where we define

$$\Phi_n\left(y+\frac{t}{\lambda_n}\right) := \sin\left(\kappa_0\left(y+\frac{t}{\lambda_n}\right)\right) + \frac{\kappa_0}{r\lambda_n}\cos\left(\kappa_0\left(y+\frac{t}{\lambda_n}\right)\right).$$

The quantity (3.45) describes the Kelvin wave dynamics of the vertical velocity component. In order to highlight the role of these waves on the upwelling dynamics, we evaluate the inviscid case of (3.45) and find

$$\begin{aligned}
\partial_t J_n(y,t) \propto\ & \Theta(t)\Theta(a-|y|)\cos\left(\kappa_0\left(y+\frac{t}{\lambda_n}\right)\right) \\
& - \Theta(a-y)\Theta(t-\lambda_n(a-y))\cos\left(\kappa_0\left(y+\frac{t}{\lambda_n}\right)\right) \\
& + \Theta(-a-y)\Theta(t-\lambda_n(-a-y))\cos\left(\kappa_0\left(y+\frac{t}{\lambda_n}\right)\right).
\end{aligned}$$

The upwelling inside the wind band ceases completely after a time span $t_n = a\lambda_n$. This is the time scale each Kelvin wave mode emanated at the northern boundary of the forcing area needs to cross the wind band. Kelvin waves excited at the southern boundary ($\propto \Theta(-a-y)$) export the upwelling into the unforced region. If non-zero friction is considered Kelvin waves do not stop the upwelling completely.

3.3.6. Discussion of the response

The response of the coastal ocean to a sudden onset of a meridionally and zonally varying wind on the f-plane was presented in (3.39) and will be discussed in this subsection. The response of the velocity components and the pressure consists basically of two terms. The one describes the WSC dynamics governed by the terms including B_n and $\partial_x B_n$ and is denoted by the affix "curl" hereafter. The other depicts the coastal dynamics that is a consequence of the coastal inhibition. It is governed by the terms proportional to A_n or C_n denoted by the affix "coast". This notation is related to the source of these terms rather than to its zonal relevance. The shape of the convolution integrals along the zonal coordinate is presented in figure 3.10 and discussed throughout this subsection.

Zonal velocity

The coastal dynamics of the zonal velocity

$$u_n^{\mathrm{coast}} \propto -\frac{1}{f} M_n(y) A_n(x) \approx -\frac{1}{f} M_n(y) \left(\Pi(x) - \Pi(0) e^{\frac{x}{R_n}} \right) \tag{3.46}$$

fulfills the eastern boundary condition (EBC), i.e. $u = 0$ at $x = 0$, and is governed by the Ekman transport

$$u_n^{\mathrm{Ekm}} \approx -\frac{1}{f} M_n(y) \Pi(x)$$

away from the eastern boundary, i.e. for $x < -R_n$. The WSC dynamics of u_n and v_n is obviously geostrophically balanced which entails

$$\partial_x u_n^{\mathrm{curl}} + \partial_y v_n^{\mathrm{curl}} = 0.$$

The divergence of the coastal zonal velocity

$$\partial_x u_n^{\mathrm{coast}} = -\partial_z w_n - \partial_y v_n^{\mathrm{coast}}$$

is balanced by the divergence of the vertical velocity and the coastal contribution of the longshore velocity as can be shown by the help of equation (3.40a).

As long as the wind forcing is homogeneous in alongshore direction, i.e. there is no divergence of the meridional wind stress, the zonal velocity component consists only of the coastal contribution. If the wind field is divergent, the term

$$u_n^{\mathrm{curl}} \propto -\frac{1}{r} \partial_y M_n(y) B_n(x) \approx -\frac{1}{r} \partial_y M_n(y) R_n^2 \left(\partial_x \Pi(x) - \partial_x \Pi(0) \right) \tag{3.47}$$

contributes to the response. Here, the notation $\partial_x \Pi(0) = \partial_x \Pi|_{x=0}$ was introduced. Obviously, the WSC term fulfills the EBC as well. The importance of the WSC dynamics relative to the Ekman offshore transport is determined basically by the spatial scales of the wind field and the Rossby Radius. The meridional scale of the wind field at which the WSC term becomes important can be estimated from the equations (3.46) and (3.47),

$$\kappa_0 \gtrsim R_n^{-2} b^{-2} \frac{r}{f} b.$$

Noting that $R_1^{-2}b^{-2} \approx 40$ and $r = 0.02\, f$ we find $\kappa_0 \gtrsim 0.8\, b$. Hence, the long shore wind scale a must be in the order of (or smaller) than the zonal scale L. Apart from the edges of the wind band, the WSC contribution to the zonal velocity is

$$u_n^{\mathrm{curl}} \propto \partial_y M_n(y) \partial_x \Pi(x).$$

If this contribution becomes relevant, it introduces an onshore flow in the south-western and north eastern quadrant of the wind patch and an offshore flow in the two others. It is worth noting that the WSC term does not contribute to the overall zonal transport in the wind patch if $Q(a) = Q(-a)$ since

$$\int_{-a}^{a} u_n^{\mathrm{curl}}\, dy \propto \int_{-a}^{a} \partial_y M_n(y)\, dy = 0.$$

This is especially the case when the wind band is symmetric in meridional direction.

In contrast to the Ekman currents that are steady right after the onset of the wind, the WSC dynamics develops with time,

$$u_n^{\mathrm{curl}} \propto \Theta(t) \left(1 - e^{-rt}\right).$$

The time scale of adjusting equilibrium conditions for that term is the inverse friction parameter. It is of the order of $r^{-1} \approx 10\,$d.

Meridional velocity

The coastal contribution to the longshore velocity in the vicinity of the coast in the case of $l \approx L$ (high WSC) is

$$v^{\mathrm{coast}} \propto C_n \propto \frac{bR_n}{1 + b^2 R_n^2} e^{\frac{x}{R_n}}.$$

The WSC term contribution is

$$v^{\mathrm{curl}} \propto \partial_x B_n(x) \propto -\frac{bR_n}{1 + b^2 R_n^2} e^{\frac{x}{R_n}}.$$

Both terms compete with each other for their relevance in shaping the coastal alongshore currents. The WSC term induces an alongshore jet in opposite direction to the coastal dynamics. A similar jet can be expected around the western edge of the wind field where

$$\partial_x B_n(x \approx l + L) \propto -\left(e^{\frac{x-L-l}{R_n}} + e^{\frac{-|x+L+l|}{R_n}}\right).$$

For the case of low WSC, i.e. $l \approx 0$, we find

$$v^{\mathrm{coast}} \propto C_n(x) \propto \frac{1}{1 + b^2 R_n^2} e^{\frac{x}{R_n}}$$

whereas the WSC contribution is negligible. The coastal alongshore velocity tends to be dominated by the gravest modes even more if the WSC is strong.

The WSC induced alongshore transport between the coast and an offshore spot is determined by

$$\int_x^0 v^{\mathrm{curl}}\, dx' \propto \int_x^0 \partial_{x'} B_n \, dx' = -B_n(x)$$

because $B_n(0) = 0$ and thus southward directed between $x = -l$ and $x = 0$.

Vertical velocity

The vertical velocity is composed of terms representing coastal upwelling and WSC induced upwelling. The maximum of the coastal upwelling is located at the coast, i.e. $x = 0$, and the response is trapped by the Rossby Radius,

$$w_n^{\mathrm{coast}} \propto C_n \propto e^{\frac{x}{R_n}}.$$

The WSC driven upwelling $w^{\mathrm{curl}} \propto B_n(x)$ is zero at the coast. The location of its maximum depends on the Rossby Radius and on the shape of the wind field,

$$\partial_x B_n \propto b R_n \Pi(x) - \sin(bl) e^{\frac{x}{R_n}} = 0.$$

The intersection of the functions $bR_n\Pi(x)$ and $\sin(bl)e^{\frac{x}{R_n}}$ marks the location of maximum WSC driven upwelling along the x-axis. A numerical approach shows that the maximum of the WSC driven vertical velocity can be found about two to four times of the Rossby Radius R_1 west of the eastern boundary. A minimum of the vertical velocity related to WSC induced downwelling can be found in the same distance east of the offshore edge of the wind band. The corresponding maxima and minima of B_n can be clearly seen in figure 3.10. The location of maximum WSC induced upwelling is associated with the western edge of the poleward directed meridional flow induced by the WSC.

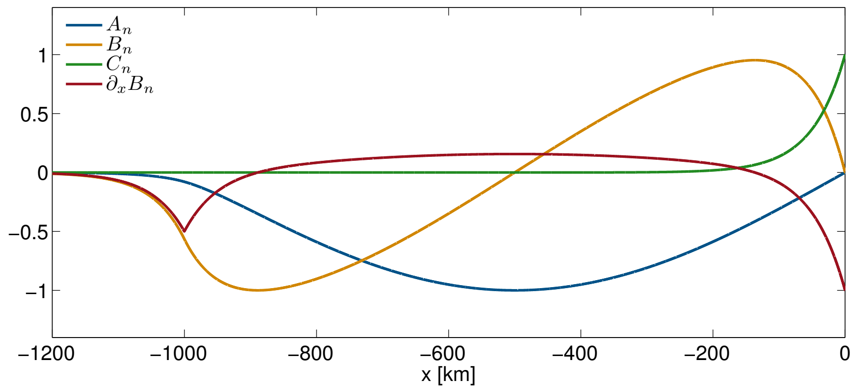

(a) $R_n = 50\,km$

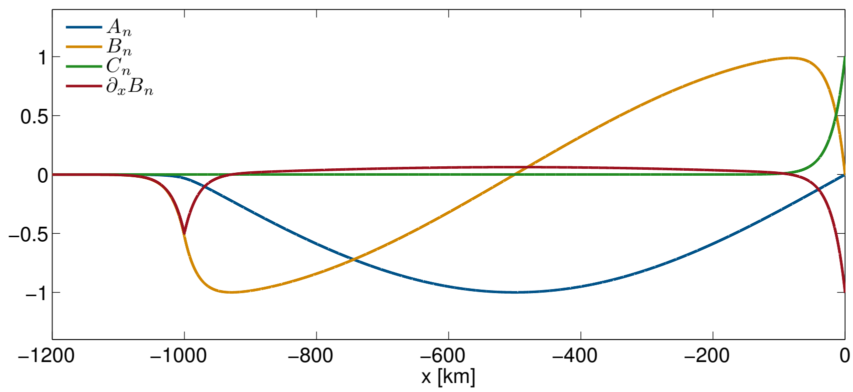

(b)) $R_n = 20\,km$

Figure 3.10. Zonal shape of the normalized functions A_n, B_n, C_n, and $\partial_x B_n$ for two different Rossby Radii and $l = 500\,\text{km}$.

3.4. Response to a seasonally varying wind on the β-plane

3.4.1. The pressure equation

On the β-plane, we use a Green's function for the pressure since the boundary conditions are simple on p and it is easy to find u, v, and w once p is known, LeBlond and Mysak (1978). We start with the set of equations (3.1) and derive an equation for p alone,

$$\boldsymbol{L}\left(\partial_t + r\right)\left[\Delta p + \boldsymbol{L}\boldsymbol{Z}p\right] + \beta\left(\left(f^2 - \left(\partial_t + r\right)^2\right)\partial_x p + 2f\left(\partial_t + r\right)\partial_y p\right) = \boldsymbol{L}\left(-f\partial_x Y + \left(\partial_t + r\right)\partial_y Y\right) - 2\beta f\left(\partial_t + r\right)Y. \quad (3.48)$$

This is the pressure equation representing the inertial and planetary wave response of the ocean to meridional wind forcing on the β-plane, see LeBlond and Mysak (1978). Here $\boldsymbol{L} := \left(\partial_t + r\right)^2 + f^2$ and $\Delta = \partial_x^2 + \partial_y^2$ is the Laplace operator and β is the variation of the Coriolis parameter with latitude according to the β-plane approach, i.e. $f = f_0 + \beta y$. The Coriolis parameter f is assumed to vary only little, i.e. $f_0 \gg \beta y$. While equation (3.48) is complicated for arbitrary time scales it can be simplified for processes with frequencies much smaller than the inertial frequency ($\omega < f$). We assume $\left(\partial_t + r\right) \ll f$ and thus $\boldsymbol{L} \approx f^2$. Then equation (3.48) simplifies to

$$\left(\partial_t + r\right)\left[\Delta p + f^2\boldsymbol{Z}p\right] + \beta\partial_x p = -f\partial_x Y + \left(\partial_t + r\right)\partial_y Y.$$

The term $2\frac{\beta}{f}\left(\partial_t + r\right)Y$ was hereby considered to be small. Neglecting furthermore the forcing term $\left(\partial_t + r\right)\partial_y Y$ on the right hand side of (3.48) because of $\left(\partial_t + r\right) < f$, we consequently end up with a differential equation for the pressure

$$\left(\partial_t + r\right)\left[\Delta p + f^2\boldsymbol{Z}p\right] + \beta\partial_x p = -f\partial_x Y. \quad (3.49)$$

An EBC for (3.49) can be derived combining (3.1a), (3.1b), and the EBC on u (3.2) to

$$\left(\partial_t + r\right)\partial_x p - f\partial_y p = -fY \qquad \text{at} \qquad x = 0. \quad (3.50)$$

The western boundary condition for the pressure p is chosen to be

$$\left(\partial_t + r\right)p = 0 \qquad \text{at} \qquad x = -\infty. \quad (3.51)$$

Alternatively, equation (3.49) can be derived by methods of perturbation (quasi-geostrophic) theory where the velocity and the pressure are decomposed into geostrophic and ageostrophic components, e.g. Gill (1982). The pressure in (3.49) then represents the geostrophic pressure that can be written in terms of a stream function $\psi = \frac{p_g}{f_0}$ such that

$$u_g = \partial_y\psi \qquad \text{and} \qquad v_g = \partial_x\psi.$$

From the EBC $u_g = 0$ follows $\partial_y \psi = 0$ at the coast, i.e. the eastern boundary coincides with a stream line. Therefore, one can choose

$$p_g = 0 \qquad \text{at} \qquad x = 0. \tag{3.52}$$

After expansion into eigenfunctions according to (3.4) and FT w.r.t. y and t we find for (3.49) and (3.50)

$$\partial_x^2 p_n - \frac{\beta}{i\overline{\omega}} \partial_x p_n - (\kappa^2 + R_n^{-2}) p_n = \frac{f}{i\overline{\omega}} \partial_x Y_n \tag{3.53}$$

and

$$\partial_x p_n + \xi p_n = \frac{f}{i\overline{\omega}} Y_n \qquad \text{at} \qquad x = 0. \tag{3.54}$$

Here, $\overline{\omega} = \omega + ir$ and $\xi = \kappa \frac{f}{\overline{\omega}}$ was introduced for convenience.

Inserting the ansatz $e^{i(kx + \kappa y - \omega t)}$ into the homogeneous and inviscid version of (3.49) in the frame of the LWA yields the linear dispersion relation of Rossby waves,

$$\omega_n(k) = \frac{-\beta k}{k^2 + R_n^{-2}}. \tag{3.55}$$

The calculation of the pressure p_n according to the equations (3.53) and (3.54) is presented in the following subsections after specifying the forcing functions.

3.4.2. Forcing function and parameter choices

The spatial wind forcing functions on the β-plane agree with those presented in section 3.3.2. However, in order to study the oceans response to time changes in the wind forcing, we choose now a periodic function of the type

$$T(t) = 1 + \widehat{T} \cos(\omega_0 t). \tag{3.56}$$

The amplitude of the periodic function is typically $\widehat{T} = 0.2$ according to the seasonal cycle observed in field data, see figure 2.5. The forcing frequency is $\omega_0 = \frac{2\pi}{365\,d} \approx 2 \cdot 10^{-7}\,\mathrm{s}^{-1}$. The Fourier transform of (3.56) is represented by

$$T(\omega) = 2\pi\delta(\omega) + \widehat{T}\pi\big(\delta(\omega + \omega_0) + \delta(\omega - \omega_0)\big). \tag{3.57}$$

The values of the parameters used in the β-plane model are mostly consistent to those used on the f-plane. But the choice of the friction parameter r in the analytical model is crucial and will be discussed throughout this study. As long as otherwise stated, we use a friction parameter of $r = 10^{-3} f$ in order to enhance the zonal trapping scale of Rossby waves. The variation of the Coriolis parameter with latitude is assumed to be $\beta = 2 \cdot 10^{-11}\,\mathrm{m}^{-1}\,\mathrm{s}^{-1}$. A comprehensive list of the chosen parameters involved in the analytical β-plane model is given in table A.2 in the appendix A.

3.4.3. Source representation of the pressure

A source representation of the pressure p_n can be found using Green's function K_n which obeys

$$\partial_x^2 K_n(x,x') - \frac{\beta}{i\varpi}\partial_x K_n(x,x') - (\kappa^2 + R_n^{-2})K_n(x,x') = \delta(x-x') \tag{3.58}$$

according to the differential equation (3.53). The calculation of the Green's function K_n is presented in the appendix C.1. It reads

$$K_n(x,x') = \frac{1}{2\alpha_n} e^{-\frac{i\beta}{2\varpi}(x-x')} \left(\frac{\xi - a_2}{\xi + a_1} e^{\alpha_n(x+x')} - e^{-\alpha_n|x-x'|} \right) \tag{3.59}$$

where $a_1 = -\frac{i\beta}{2\varpi} + \alpha_n$ and $a_2 = \frac{i\beta}{2\varpi} + \alpha_n$ and

$$\alpha_n(\omega) = \left\{ \begin{array}{ll} i\frac{\beta}{2\varpi}\sqrt{1 - \frac{\varpi^2}{\omega_c^2}} & |\omega| < \omega_c \\ \sqrt{\frac{1}{R_n^2} - \frac{\beta^2}{4\varpi^2}} & |\omega| > \omega_c \end{array} \right\}.$$

Here, $\omega_c = \frac{\beta R_n}{2}$ is the critical (maximum) frequency for Rossby waves. The mode number indicating subscript n has been dropped in the quantities a_1, a_2, and ω_c for convenience.

Setting β to zero in (3.59) yields the Green's function for the pressure on the f-plane,

$$K_n(x,x') \stackrel{\beta\to 0}{=} \frac{1}{2\alpha_n} \left(\frac{\xi - \alpha_n}{\xi + \alpha_n} e^{\alpha_n(x+x')} - e^{-\alpha_n|x-x'|} \right) \tag{3.60}$$

where $\alpha_n^2 \stackrel{\beta\to 0}{=} \kappa^2 + R_n^{-2}$. In contrast to the Green's function for the cross-shore component, equation (3.60) includes the explicit Kelvin pole in the frame of the LWA,

$$\frac{1}{\xi + \alpha_n} \stackrel{\beta\to 0}{=} \frac{\varpi}{f(\kappa + \lambda_n \varpi)}.$$

With the help of $\frac{\xi - a_2}{\xi + a_1} = 1 - \frac{2\alpha_n}{\xi + a_1}$ equation (3.59) can be reformulated to

$$K_n(x,x') = G_n(x,x') - \frac{1}{\xi + a_1} e^{a_1 x} e^{a_2 x'} \tag{3.61}$$

where G_n is the Green's function for the zonal velocity u_n on the β-plane, see equation (3.10).

A source representation of p_n in terms of the Green's function K_n is derived in the appendix C.2. It reads

$$p_n(x,\omega,\kappa) = \frac{f}{i\varpi} \left(K_n * \partial_{x'} Y_n - K_n(x,0) Y_n(0) \right). \tag{3.62}$$

The expression $K_n * \partial_{x'} Y_n$ stands for the convolution integral

$$K_n * \partial_{x'} Y_n = \int_{-\infty}^{0} dx' K_n(x,x') \partial_{x'} Y_n(x').$$

Moreover, we find from equation (3.61)

$$K_n(x,0)Y_n(0) = \frac{e^{a_1 x}}{\xi + a_1} Y_n(0)$$

because of $G_n(x,0) = 0$.

3.4.4. Calculation of the response

Calculation of the convolution integrals

The calculation of the pressure p_n according to (3.62) demands the calculation of the convolution integral $K_n * \partial_{x'}\Pi$. We find

$$K_n * \partial_{x'}\Pi = G_n(x,x') * \partial_{x'}\Pi(x') - \frac{1}{\xi + a_1} e^{a_1 x} \int_{-\infty}^{0} e^{a_2 x'} \partial_{x'}\Pi(x') dx' \tag{3.63}$$

with the help of equation (3.61). The integral $B_n^R := G_n * \partial_{x'}\Pi$ is calculated in the appendix B.1 and reads

$$\begin{aligned} B_n^R(x,\omega) = -\frac{b}{2\alpha_n} \Bigg[&\left(\frac{a_2}{a_2^2+b^2} + \frac{a_1}{a_1^2+b^2}\right) e^{a_1 x} \sin(bl) + \left(\frac{-b}{a_2^2+b^2} + \frac{b}{a_1^2+b^2}\right) e^{a_1 x} \cos(bl) \\ &- \Theta(x+L+l) \left(\left(\frac{a_2}{a_2^2+b^2} + \frac{a_1}{a_1^2+b^2}\right) \sin(b(x+l)) + \left(\frac{-b}{a_2^2+b^2} + \frac{b}{a_1^2+b^2}\right) \cos(b(x+l)) \right) \\ &+ \frac{a_2}{a_2^2+b^2} e^{a_1 x} e^{-a_2(L+l)} + \Theta(-x-L-l) \frac{a_1}{a_1^2+b^2} e^{a_1(x+L+l)} - \Theta(x+L+l) \frac{a_2}{a_2^2+b^2} e^{-a_2(x+L+l)} \Bigg]. \end{aligned} \tag{3.64}$$

The second contribution in (3.63) amounts to

$$\frac{1}{\xi + a_1} e^{a_1 x} \int_{-\infty}^{0} e^{a_2 x'} \partial_{x'}\Pi(x') dx' = \frac{1}{\xi + a_1} \frac{b\, e^{a_1 x}}{a_2^2 + b^2} \left(a_2 \sin(bl) - b\cos(bl) + a_2 e^{-a_2(L+l)} \right). \tag{3.65}$$

Moreover, we need to estimate the contribution at the eastern boundary of the model domain in (3.62),

$$K_n(x,0)\Pi(0) = \frac{1}{2\alpha_n} e^{-\frac{i\beta}{2\varpi}x} \left(\frac{\xi - a_2}{\xi + a_1} e^{\alpha_n x} - e^{\alpha_n x} \right) \cos(bl) = -\frac{1}{\xi + a_1} e^{a_1 x} \cos(bl) \tag{3.66}$$

where $a_1 + a_2 = 2\alpha_n$ was used.

Response in the x-κ-ω-domain

From equation (3.62), we find the response of the pressure,

$$p_n(x,\kappa,\omega) = \frac{v_*^2}{h_n} Q(\kappa) T(\omega) \left(\frac{f}{i\varpi} B_n^R(x,\omega) + \frac{f}{i\varpi} \frac{1}{\xi + a_1} C_n^R(x,\omega) \right) \tag{3.67}$$

where $C_n^R(x,\omega)$ originates from the sum of (3.66) and (3.65),

$$C_n^R(x,\omega) = \frac{a_2}{a_2^2+b^2}\left(b\sin(bl) + a_2\cos(bl) + be^{-a_2(L+l)}\right)e^{a_1 x}. \tag{3.68}$$

The first term in (3.67) that is proportional to B_n^R fulfills the quasi-geostrophic EBC (3.52). The second term

$$\frac{f}{i\varpi}\frac{1}{\xi+a_1}C_n^R(x,\omega)$$

fulfills the EBC (3.50), i.e. the boundary condition for time scales where the dynamics of Kelvin waves need to be considered.

An equation for the meridional velocity component v_n can be obtained through the geostrophic balance (3.43a),

$$v_n(x,\kappa,\omega) = \frac{v_*^2}{h_n}T(\omega)Q(\kappa)\left(-\frac{1}{i\varpi}\partial_x B_n^R(x,\omega) - \frac{1}{i\varpi}\frac{1}{\xi+a_1}\partial_x C_n^R(x,\omega)\right) \tag{3.69}$$

where $\partial_x C_n^R(x,\omega) = a_1 C_n^R(x,\omega)$.

An expression for the zonal currents u_n can be derived following the relation (3.1b), and we find

$$u_n(x,\kappa,\omega) = \frac{v_*^2}{h_n}T(\omega)Q(\kappa)\left(\frac{i\kappa}{i\varpi}B_n^R(x,\omega) + \frac{1}{f}A_n^R(x,\omega)\right) \tag{3.70}$$

where

$$\begin{aligned}
A_n^R(x,\omega) = \frac{1}{2\alpha_n}\Bigg[&\left(\frac{ba_2^2}{a_2^2+b^2} - \frac{ba_1^2}{a_1^2+b^2}\right)e^{a_1 x}\sin(bl) + \left(\frac{a_2^3}{a_2^2+b^2} + \frac{a_1^3}{a_1^2+b^2}\right)e^{a_1 x}\cos(bl)\\
-\Theta(x+L+l)&\left(\left(\frac{ba_2^2}{a_2^2+b^2} - \frac{ba_1^2}{a_1^2+b^2}\right)\sin(b(x+l)) + \left(\frac{a_2^3}{a_2^2+b^2} + \frac{a_1^3}{a_1^2+b^2}\right)\cos(b(x+l))\right)\\
&+\frac{ba_2^2}{a_2^2+b^2}e^{a_1 x}e^{-a_2(L+l)} - \Theta(-x-L-l)\frac{ba_1^2}{a_1^2+b^2}e^{a_1(x+L+l)}\\
&-\Theta(x+L+l)\frac{ba_2^2}{a_2^2+b^2}e^{-a_2(x+L+l)}\Bigg].
\end{aligned} \tag{3.71}$$

Response in the frequency domain

Performing the inverse FT w.r.t. κ in (3.67) leads us to the integral

$$I_n^R(y,\omega) = \int_{-\infty}^{\infty}\frac{-iQ(\kappa)}{\kappa+\frac{\varpi}{f}a_1}e^{i\kappa y}\frac{d\kappa}{2\pi}. \tag{3.72}$$

Its structure is similar to the integral (3.30) that governs the dynamics of alongshore Kelvin waves, except for the factor $\frac{a_1}{f}$ that accompanies ϖ. Treating the integral (3.72) formerly, we need to close the contour in the upper or lower complex κ-plane. Hereby, the sign of ϖa_1 controls the location of the pole in the complex plane and, consequently, the propagation direction of the waves with wave number $\frac{\overline{\omega}}{f}a_1$. Assuming a southward propagation of these waves demands $\mathrm{Im}(\overline{\omega}a_1) > 0$. This condition can be evaluated in the case of long Rossby waves, i.e. $a_1 \approx -\frac{i\overline{\omega}}{\beta R_n^2}$, see equation (3.78), and we find $r^2 > \omega^2$. This result implies that a southward propagation of Kelvin waves can be achieved only, if the friction parameter is greater than the forcing frequency. Obviously, this condition can not be fulfilled in the inviscid limit which points to an inconsistency.

Actually, we have to acknowledge that Kelvin waves act on timescales much shorter than those of Rossby waves as pointed out already in section 3.1.1. Hence, the longshore dynamics is adjusted within a relatively small period of time by Kelvin waves, see e.g. Philander and Yoon (1982). The time scale Kelvin waves need to cross the forced area is a few days corresponding to high frequencies. In that frequency range, i.e. $\omega \gg \omega_c = \frac{\beta R_n}{2}$, we find

$$\frac{\overline{\omega}}{f}a_1 \approx \frac{\overline{\omega}}{f}\left(\frac{i\beta}{2\overline{\omega}} + R_n^{-1}\right) = \left(i\frac{\omega_c}{\overline{\omega}} + 1\right)\frac{\overline{\omega}}{f}R_n^{-1} \approx \frac{\overline{\omega}}{f}R_n^{-1} = \lambda_n\overline{\omega}.$$

Applying this approximation, the integral (3.72) converges to the corresponding integral on the f-plane (3.30) by using temporal scaling arguments. As a result, the coastal ocean is adjusted by Kelvin waves at all times modified only by the seasonal cycle and the westward propagation of Rossby waves.

The fact that Kelvin waves exist independently of the β-effect can be demonstrated by deriving a wave equation for the meridional velocity component (or the pressure) from the homogeneous and inviscid version of the set (3.1) near the eastern boundary, i.e. $u \approx 0$,

$$c_n^2\partial_y^2 v - \partial_t^2 v = 0.$$

This Kelvin wave equation was obtained without creating any β-terms.

In the case of homogeneous wind forcing in meridional direction, i.e. $Q(\kappa) = \delta(\kappa)$, the integral (3.72) converges to $\frac{f}{i\overline{\omega}a_1}$. In accordance to the f-plane results meridional wave propagation vanishes.

Summary of the solution

The response of the horizontal velocity components and the pressure in the frequency domain can be summarized as follows:

$$u_n(x,y,\omega) = \frac{v_*^2}{h_n}T(\omega)\left(\frac{1}{i\overline{\omega}}B_n^R(x,\omega)\partial_y Q(y) + \frac{1}{f}A_n^R(x,\omega)Q(y)\right), \tag{3.73a}$$

$$v_n(x,y,\omega) = \frac{v_*^2}{h_n}T(\omega)\left(-\frac{1}{i\overline{\omega}}\partial_x B_n^R(x,\omega)Q(y) - \frac{1}{f}I_n(y,\omega)\partial_x C_n^R(x,\omega)\right), \tag{3.73b}$$

$$p_n(x,y,\omega) = \frac{v_*^2}{h_n}T(\omega)\left(\frac{f}{i\overline{\omega}}B_n^R(x,\omega)Q(y) + I_n(y,\omega)C_n^R(x,\omega)\right). \tag{3.73c}$$

The convolution integrals (3.71), (3.64), and (3.68) can be reformulated to

$$\begin{aligned}
A_n^R(x,\omega) = \frac{1}{HN} \Bigg[& \left(R_n^{-4}\left(1+b^2R_n^2\right) - \frac{b^2\beta^2}{\varpi^2}\right)\cos(bl)e^{a_1x} - \frac{b^3\beta}{i\varpi}\sin(bl)e^{a_1x} \\
& -\Theta(x+L+l)\left(\left(R_n^{-4}\left(1+b^2R_n^2\right) - \frac{b^2\beta^2}{\varpi^2}\right)\cos(b(x+l)) - \frac{b^3\beta}{i\varpi}\sin(b(x+l))\right)\Bigg] \\
+ \frac{b}{2\alpha_n} & \left[\frac{a_2^2}{a_2^2+b^2}e^{-a_2(L+l)}\left(e^{a_1x} - \Theta(x+L+l)e^{-a_2x}\right) - \Theta(-x-L-l)\frac{a_1^2}{a_1^2+b^2}e^{a_1(x+L+l)}\right]
\end{aligned} \tag{3.74a}$$

and

$$\begin{aligned}
B_n^R(x,\omega) = -\frac{b}{HN} \Bigg[& R_n^{-2}\left(1+R_n^2b^2\right)\sin(bl)e^{a_1x} - b\frac{\beta}{i\varpi}\cos(bl)e^{a_1x} \\
& -\Theta(x+L+l)\left(R_n^{-2}\left(1+R_n^2b^2\right)\sin(b(x+l)) - b\frac{\beta}{i\varpi}\cos(b(x+l))\right)\Bigg] \\
- \frac{b}{2\alpha_n} & \left[\frac{a_2}{a_2^2+b^2}e^{-a_2(L+l)}\left(e^{a_1x} - \Theta(x+L+l)e^{-a_2x}\right) + \Theta(-x-L-l)\frac{a_1}{a_1^2+b^2}e^{a_1(x+L+l)}\right]
\end{aligned} \tag{3.74b}$$

and

$$C_n^R(x,\omega) = \frac{a_2}{a_2^2+b^2}e^{a_1x}\left(b\sin(bl) + a_2\cos(bl) + be^{-a_2(L+l)}\right). \tag{3.74c}$$

Hereby, a common denominator $HN = (a_1^2+b^2)(a_2^2+b^2) = R_n^{-4}(1+b^2R_n^2)^2 - \frac{b^2\beta^2}{\varpi^2}$ was introduced. Furthermore, the relations

$$\begin{aligned}
a_1a_2 &= R_n^{-2}, \\
a_1+a_2 &= 2\alpha_n, \qquad \text{and} \qquad a_1-a_2 = \frac{\beta}{i\varpi}, \\
a_1^2+a_2^2 &= 2R_n^{-2} - \frac{\beta^2}{\varpi^2}, \qquad \text{and} \qquad a_1^2-a_2^2 = 2\alpha_n\frac{\beta}{i\varpi}, \\
a_1^3+a_2^3 &= 2\alpha_n\left(R_n^{-2} - \frac{\beta^2}{\varpi^2}\right),
\end{aligned}$$

were used during the reformulation process. It is worth noting that in contrast to the f-plane results the convolution integrals depend on the frequency ω through the β-effect.

The convolution integrals fulfill the equations

$$\partial_x A_n^R = \frac{\beta}{i\varpi}\partial_x B_n^R + R_n^{-2}B_n^R + \partial_x C_n^R, \tag{3.75a}$$

$$\partial_x B_n^R = A_n^R - C_n^R + \Pi \tag{3.75b}$$

that converge to the equations (3.40) in the case of $\beta \to 0$ and consequently $\partial_x C_n^R \overset{\beta \to 0}{=} R_n^{-1} C_n$. Combining the relations (3.75) yields

$$\left(\partial_x^2 - \frac{\beta}{i\varpi}\partial_x - R_n^{-2}\right) B_n^R(x) = \partial_x \Pi(x), \tag{3.76}$$

and from (3.53), (3.73c), and (3.75) follows

$$\left(\partial_x^2 - \frac{\beta}{i\varpi}\partial_x - R_n^{-2}\right) C_n^R(x) = 0.$$

Vertical velocity component

The response of the vertical velocity w_n in the frequency domain is calculated using the Fourier transform of (3.1c) that reads

$$w_n(x, y, \omega) = \frac{i\varpi}{N^2}\partial_z p_n(x, y, \omega). \tag{3.77}$$

Inserting the pressure p_n and performing the mode summation according to (3.4) gives for the baroclinic modes ($n \geq 1$)

$$\begin{aligned} w(x, y, z, \omega) = -v_*^2 \frac{H}{H_{\text{mix}}} \sum_{n=1}^{\infty} \frac{2\lambda_n^2}{\pi^2 n^2} \sin\left(\frac{n\pi}{H} H_{\text{mix}}\right) \sin\left(\frac{n\pi}{H} z\right) \\ \cdot T(\omega)\left(f B_n^R(x, \omega) Q(y) + i\varpi I_n(y, \omega) C_n^R(x, \omega)\right). \end{aligned}$$

Consistency of the solution

The analytical β-plane model is designed to cover a broad frequency band below the inertial frequency. The coastal oceans response to such forcing includes Kelvin waves that act on time scales of a few ten days and planetary waves that act on time scales of hundred days. Both types of waves can not be combined in a consistent linear theory that is uniformly valid at all frequencies. The reason therefore may be too many approximations while deriving the pressure equation (3.49). Hence, the presented solution (3.73) does not solve the set (3.1) exactly, but it is a good approximation that combines Kelvin and Rossby waves in the oceans response.

3.4.5. Discussion of the response in the frequency domain

The basic structure of the solution (3.73) is similar to the f-plane case. It contains the response of the ocean to the WSC regime and the coastal dynamics separately. The convolution integrals A_n^R, B_n^R, and C_n^R pass over to the corresponding functions on the f-plane in the limit $\beta \to 0$. Since β does not occur in other quantities than the convolution integrals, the solution (3.73) passes over to the set (3.39). The same result can be achieved in the high frequency case, i.e. $\omega \to f$, because of $a_{1/2} \stackrel{\omega \to f}{=} R_n^{-1}$. Thus, the high frequency limit of the presented β-plane response is the f-plane solution.

In contrast to the f-plane case, the convolution integrals (3.74) contain two different response parts. The one is the direct wind driven flow restricted to the area of the wind band containing those terms proportional to the forcing function $\Pi(x)$ or its derivative $\partial_x \Pi(x)$. The other is the indirect response through waves excited at the edges of the forced region, i.e. terms proportional to $e^{a_1 x}$ or $e^{a_2 x}$. Here, the expressions $e^{a_1 x}$ describe long Rossby waves that travel westward into the open ocean with wave number $k_1 = -ia_1$. These waves are either emanated at the coast or at the offshore edge of the forcing area. The latter waves are proportional to $\Theta(-x - L - l)$. The term $e^{-a_2 x}$ represents short Rossby waves excited at the offshore edge of the wind band traveling with wave number $-k_2 = -ia_2$ eastward into the forced region. The amplitude of the short Rossby waves is very small compared to the long ones excited at the offshore edge of the wind band as long as the zonal scale of the wind forcing exceeds the Rossby Radius,

$$\frac{a_1}{a_1^2 + b^2} > \frac{a_2}{a_2^2 + b^2} \quad \Rightarrow \quad R_n^2 b^2 < 1.$$

For frequencies well below the critical frequency of Rossby waves, i.e. $\omega < \omega_c$, we can develop the root in the wave number a_1 into a power series,

$$a_1 = \frac{i\beta}{2\varpi}\left(-1 + \sqrt{1 - \frac{\varpi^2}{\omega_c^2}}\right) \approx \frac{i\beta}{2\varpi}\left(-1 + \left(1 - \frac{1}{2}\frac{\varpi^2}{\omega_c^2}\right)\right) = -\frac{i\varpi}{\beta R_n^2}. \tag{3.78}$$

From that follows $k_1 = -\frac{\omega}{\beta R_n^2}$ in the inviscid case. In the long wave limit, Rossby waves are obviously non-dispersive. The above performed approximation is referred to as the long Rossby wave approximation (LRWA). For the steady state response, i.e. $\omega = 0$, we find $a_1 = \frac{r}{\beta R_n^2}$ which is the inverse trapping scale of long Rossby waves in zonal direction. The trapping scale exceeds the zonal scale of the wind band, i.e. $\frac{\beta R_n^2}{r} > l$. Consequently, the Rossby wave terms contribute to the response in the interior forcing area, i.e. $x \approx -l$, as demonstrated by the example of the WSC driven vertical velocity

$$w_n^{\text{curl}} \propto \partial_x \Pi(x) - \partial_x \Pi(0) e^{\frac{r}{\beta R_n^2} x}. \tag{3.79}$$

It changes its sign in the interior wind band due to the term $\partial_x \Pi(x)$, but the specific location is controlled by the trapping scale in the exponential term. Since the trapping scale decreases with increasing mode number the location of change of sign is located further offshore for higher order mode numbers. Otherwise, an increase of the friction parameter decreases the trapping scale. The near coastal limit for the change of direction in the case of a high friction is then $x = -l$ controlled by the term $\partial_x \Pi(x)$ in (3.79).

3.4.6. An analytical approach to the response in the time domain

The derivation of the oceans response in the time domain is not straightforward as on the f-plane since the convolution integrals depend on the frequency ω. To access an approximate solution in the time domain we rewrite the convolution integrals (3.74a) and (3.74b) neglecting the third line terms,

$$
\begin{aligned}
A_n^R(x,\omega) \approx & -\Pi(x) + \Pi(0)e^{a_1 x} \\
& + \frac{bR_n^2}{1+b^2R_n^2}\frac{1}{(\overline{\omega}^2-\gamma_n^2)}\left(\overline{\omega}^2 b(\Pi(x)-e^{a_1 x}\Pi(0)) + i\overline{\omega}\gamma_n(\partial_x\Pi(x)-e^{a_1 x}\partial_x\Pi(0))\right),
\end{aligned}
\tag{3.80}
$$

$$
B_n^R(x,\omega) \approx \frac{R_n^2}{1+b^2R_n^2}\frac{-1}{(\overline{\omega}^2-\gamma_n^2)}\left(\overline{\omega}^2(\partial_x\Pi(x)-e^{a_1 x}\partial_x\Pi(0)) - i\overline{\omega}\gamma_n b(\Pi(x)-e^{a_1 x}\Pi(0))\right). \tag{3.81}
$$

Here, the frequency

$$
\gamma_n = \frac{\beta b}{b^2+R_n^{-2}} \tag{3.82}
$$

was introduced. It combines the zonal scale of the wind forcing and the Rossby Radius with the change of the Coriolis parameter to a temporal scale. The frequency γ_n vanishes notably on the f-plane, i.e. for $\beta = 0$, and for homogeneous wind forcing in cross-shore direction, i.e. for $b = 0$. The frequency γ_n depends mainly on the Rossby Radius. Its influence on γ_n is presented in figure 3.11. The frequency γ_n is in the range of the forcing frequency ω_0 but smaller than the critical Rossby wave frequency ω_c. Notice the similarity of γ_n to the linear Rossby wave dispersion relation (3.55). The zonal wave number k in (3.55) is simply replaced by the wave number b representing the zonal scale of the wind field in (3.82).

In this section, the response of the ocean to a switch-on wind and a periodic forcing in the time domain is studied exemplary for the leading term in the convolution integral B_n^R that impacts pressure and vertical velocity. The leading term in the case of strong WSC, i.e. $l \approx L$, in (3.81) is

$$
\frac{R_n^2}{1+b^2R_n^2}\frac{i\overline{\omega}}{\overline{\omega}^2-\gamma_n^2}\left(\partial_x\Pi(x)-\partial_x\Pi(0)e^{a_1 x}\right). \tag{3.83}
$$

Here, the factor $(i\overline{\omega})^{-1}$ from (3.73c) was included.

Switch-on wind

In a first approach, we neglect the wave term in equation (3.83) and discuss the response to a switch-on wind. Using (3.17) yields the Fourier integral

$$
\int \frac{i}{\omega+i\epsilon}\frac{i\overline{\omega}}{\overline{\omega}^2-\gamma_n^2}e^{-i\omega t}\frac{d\omega}{2\pi} = \Theta(t)\frac{r}{r^2+\gamma_n^2}\left(1+e^{-rt}\left(\frac{\gamma_n}{r}\sin(\gamma_n t)-\cos(\gamma_n t)\right)\right). \tag{3.84}
$$

Notice the similarity to the integral (3.24) that is part of the response to spatially inhomogeneous wind stress in the near-inertial frequency range. The frequency Δ_n in (3.24) is replaced by γ_n here.

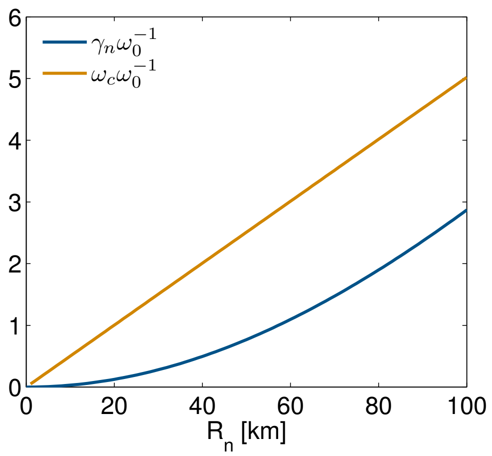

Figure 3.11. Rossby frequency γ_n and critical Rossby wave frequency ω_c normalized by the forcing frequency ω_0 versus the Rossby Radius R_n.

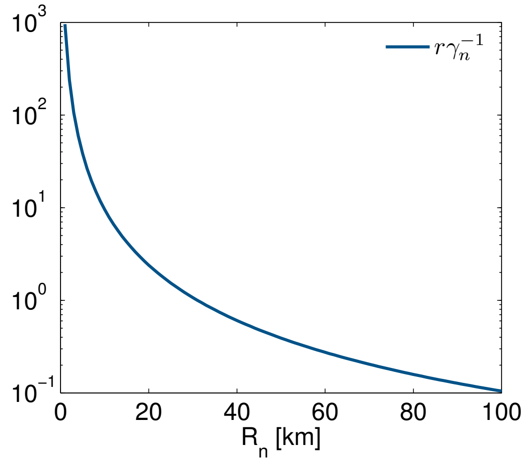

Figure 3.12. Damping ratio $r\gamma_n^{-1}$ versus the Rossby Radius R_n.

The response represented by (3.84) consists of a time independent part overlayed by a damped oscillation. The damping constant of the oscillation is the friction parameter r. In contrast to the inertial oscillations where $\Delta_n > f \gg r$, the frequency γ_n is in the order of the friction parameter r for $R_n \approx 30$ km, see figure 3.12. The damping ratio $\frac{r}{\gamma_n}$ is mainly controlled by the Rossby Radius R_n through the Rossby oscillation frequency γ_n. For values lower than $R_n \leq 30$ km, i.e. on the shelf, for higher order mode numbers, or higher latitudes, the oscillations are over-damped since the damping ratio $\frac{r}{\gamma_n} > 1$. For higher values of the Rossby Radii, as can be found for instance towards the open ocean, the oscillations are under-damped, i.e. $\frac{r}{\gamma_n} < 1$.

An approximate response of the wave terms in (3.83) can be achieved for long Rossby waves. The inverse FT w.r.t. ω in the frame of the LRWA yields the integral

$$\begin{aligned}\int \frac{i}{\omega + i\epsilon} \frac{-i\overline{\omega}}{\overline{\omega}^2 - \gamma_n^2} e^{-i\omega t} e^{-\frac{i\overline{\omega}}{\beta R_n^2} x} \frac{d\omega}{2\pi} \\ = -\Theta\left(t + \frac{x}{c_n}\right) \frac{r}{r^2 + \gamma_n^2} \left(e^{\frac{r}{\beta R_n^2} x} + e^{-rt} \left(\frac{\gamma_n}{r} \sin\left(\gamma_n \left(t + \frac{x}{c_n}\right)\right) - \cos\left(\gamma_n \left(t + \frac{x}{c_n}\right)\right)\right)\right).\end{aligned}$$

The response of the Rossby wave term consists of a time independent part, i.e. $e^{\frac{r}{\beta R_n^2} x}$, trapped to the coast by the trapping scale $\frac{\beta R_n^2}{r}$ and long Rossby waves that travel westward with group speed $c_n = -\beta R_n^2$. These waves are damped by the time scale r^{-1}. Hence, the trapping scale is the distance long Rossby waves travel in the time span r^{-1}. Typical first mode phase speeds of long Rossby waves are in the order of $c_1 \approx 0.05\,\mathrm{m\,s^{-1}}$.

Periodic forcing

The transient response to a periodic forcing of the term (3.83) is evaluated by using the forcing function (3.57). Once more, the wave term in (3.83) is neglected in a first approach. The Fourier integral reads then

$$\int T(\omega)\frac{i\overline{\omega}}{\overline{\omega}^2-\gamma_n^2}e^{-i\omega t}\frac{d\omega}{2\pi}=\frac{r}{r^2+\gamma_n^2}+\widehat{T}\frac{\omega_0(\omega_0^2+r^2-\gamma_n^2)\sin(\omega_0 t)+r(\omega_0^2+r^2+\gamma_n^2)\cos(\omega_0 t)}{(\omega_0^2+r^2)^2-2\gamma_n^2(\omega_0^2-r^2)+\gamma_n^4}. \tag{3.85}$$

The response to the periodic forcing consists of a time independent contribution overlayed by an oscillating signal with forcing frequency ω_0. The response can be rewritten to be proportional to

$$\cos(\omega_0 t-\phi_n)$$

where ϕ_n is the phase angle between forcing and response,

$$\phi_n=\arctan\left(\frac{\omega_0}{r}\left(1-\frac{2\gamma_n^2}{\omega_0^2+r^2+\gamma_n^2}\right)\right). \tag{3.86}$$

The phase angle ϕ_n is mainly controlled by the ratio of the forcing frequency ω_0 and the friction parameter r. The argument in (3.86) is positive for small Rossby Radii, i.e. $R_n \leq 20\,\text{km}$, as the second term in (3.86) can be neglected. In this case, the phase angle is in the order of $0.40\,\pi$. Thus, the response lags the forcing by about 70 days in this example. For higher Rossby Radii, the argument in (3.86) decreases and the phase angle between forcing and the response decreases as well.

The integral including the wave terms in the frame of the LRWA can be calculated similar to (3.85) by replacing t by $t+\frac{x}{c_n}$ in the exponent,

$$\begin{aligned}\int T(\omega)\frac{i\overline{\omega}}{\overline{\omega}^2-\gamma_n^2}e^{-i\omega t}e^{-\frac{i\overline{\omega}}{\beta R_n^2}x}\frac{d\omega}{2\pi}&=\frac{r}{r^2+\gamma_n^2}e^{\frac{r}{\beta R_n^2}x}\\&+\widehat{T}e^{\frac{r}{\beta R_n^2}x}\frac{\omega_0(\omega_0^2+r^2-\gamma_n^2)\sin\left(\omega_0\left(t+\frac{x}{c_n}\right)\right)+r(\omega_0^2+r^2+\gamma_n^2)\cos\left(\omega_0\left(t+\frac{x}{c_n}\right)\right)}{(\omega_0^2+r^2)^2-2\gamma_n^2(\omega_0^2-r^2)+\gamma_n^4}.\end{aligned}$$

The response now consists of Rossby waves with the forcing frequency ω_0 and the phase speed c_n. The phase shift between forcing and response depends now additionally on the zonal coordinate x,

$$\propto\cos\left(\omega_0\left(t+\frac{x}{c_n}\right)-\phi_n\right).$$

It is worth noting that the vertical velocity is related to the pressure field by the time derivative. The phase angle for w in the transient solution therefore changes to

$$\phi_n^w=\phi_n^p+\frac{\pi}{2}.$$

3.4.7. The numerical evaluation of the response in the time domain

The complete transient response to a periodic forcing can be obtained by calculating the imaginary and real parts of the convolution integrals numerically. In order to receive a solution in the time domain, we need to Fourier transform the equations (3.73) w.r.t. ω,

$$\Upsilon(t) = \int T(\omega)\Upsilon(\omega)e^{-i\omega t}\frac{d\omega}{2\pi}$$

where T is the wind forcing function, see (3.57), and Υ stands for any of the quantities A_n^R, B_n^R, C_n^R, and I_n, or a combination of these. Performing the above integration yields

$$\Upsilon(t) = \Upsilon(0) + \frac{\widehat{T}}{2}\left(\Upsilon(\omega_0)e^{-i\omega_0 t} + \Upsilon(-\omega_0)e^{i\omega_0 t}\right) = \Upsilon(0) + \widehat{T}\,\mathrm{Re}(\Upsilon(\omega_0)e^{-i\omega_0 t}) \tag{3.87}$$

where we used that $\Upsilon(\omega_0) = \Upsilon^*(-\omega_0)$. Hereby, the asterisk denotes the complex conjugate. Notice that

$$a_{1/2}^2 = -k_{1/2}^2, \qquad k_{1/2}(-\omega_0) = -k_{1/2}^*(\omega_0), \qquad k_{1/2}^2(-\omega_0) = k_{1/2}^{2*}(\omega_0),$$
$$\alpha_n^*(\omega_0) = \alpha_n(-\omega_0), \qquad i\overline{\omega}(\omega_0) = (i\overline{\omega}(-\omega_0))^*.$$

From (3.87) it can be seen that the oceans response consists of a steady state signal and a seasonal cycle with the amplitude $\widehat{T}$. Averaging the response over one forcing period $T_0 = \frac{2\pi}{\omega_0}$ yields the steady state response,

$$\overline{\Upsilon}(t) = \frac{1}{T_0}\int_0^{T_0}\Upsilon(t)dt = \Upsilon(0) + \frac{1}{i\omega_0}\widehat{T}\,\mathrm{Re}\left(\Upsilon(\omega_0)(e^{-i\omega_0 T_0} - 1)\right) = \Upsilon(0)$$

since the transient of the solution vanishes.

3.4.8. Steady state of the inviscid ocean

In this section, we study the response of the currents and the pressure in the inviscid and stationary regime, i.e. $r = 0$ and $\omega = 0$. This equilibrium state corresponds to a Sverdrup regime adjusted in the wake of a Rossby wave. First of all, we investigate the response of the terms associated with the short Rossby waves and those terms related to long Rossby waves emitted at the offshore edge of the wind band. These terms are the third row terms in (3.74a) and (3.74b). We find numerically

$$a_1 \overset{\omega,r\to 0}{=} 0 \qquad \text{and} \qquad a_2 \overset{\omega,r\to 0}{=} \infty$$

that is consistent with (3.78). Therefore, all exponential terms tend to one and, moreover, the amplitudes vanish,

$$\frac{1}{2\alpha_n}\frac{a_2}{a_2^2+b^2} = \frac{a_2^{-2}}{(a_1+a_2)(a_2^{-1}+a_2^{-3}b^2)} \overset{\omega,r\to 0}{=} 0,$$
$$\frac{1}{2\alpha_n}\frac{a_1}{a_1^2+b^2} = \frac{a_1}{(a_1+a_2)(a_1^2+b^2)} \overset{\omega,r\to 0}{=} 0.$$

From (3.81) it can now easily be seen that

$$\frac{1}{i\omega}B_n^R(x,\omega) \overset{\omega,r\to 0}{=} -\frac{1}{\beta}\left(\Pi(x)-\Pi(0)\right) \tag{3.88}$$

and

$$\frac{1}{i\omega}\partial_x B_n^R(x,\omega) \overset{\omega,r\to 0}{=} -\frac{1}{\beta}\partial_x\Pi(x). \tag{3.89}$$

Moreover, we find for the convolution integral C_n^R

$$C_n^R(x) \overset{\omega,r\to 0}{=} \Pi(0) \tag{3.90}$$

because of

$$\frac{a_2^2}{a_2^2+b^2} = \frac{1}{1+a_2^{-2}b^2} \overset{\omega,r\to 0}{=} 1 \quad \text{and} \quad \frac{a_2}{a_2^2+b^2} \overset{\omega,r\to 0}{=} 0.$$

The function A_n^R gives

$$A_n^R(x,\omega) \overset{\omega,r\to 0}{=} -\Pi(x)+\Pi(0) \tag{3.91}$$

because of (3.75b). In the stationary and inviscid regime follows $\partial_y I_n(y) = Q(y)$ from the definition of the integral I_n. Finally, we find the stationary solution for the horizontal current components and the meridional derivative of the pressure

$$u_n(x,y) = -\left(\frac{1}{\beta}\partial_y + \frac{1}{f}\right)\left(Y_n(x,y) - Y_n(0,y)\right), \tag{3.92a}$$
$$v_n(x,y) = \frac{1}{\beta}\partial_x Y_n(x,y), \tag{3.92b}$$
$$\partial_y p_n(x,y) = -\partial_y\left(\frac{f}{\beta}\left(Y_n(x,y)-Y_n(0,y)\right)\right) + Y_n(0,y). \tag{3.92c}$$

We point out that the analytical β-plane model reproduces the Sverdrup balance (3.92b) in the inviscid and stationary limit. Moreover, the currents in the stationary and inviscid regime are fully horizontal because of (3.1c). The equations (3.92) solve the stationary and inviscid version of the set (3.43), i.e.

$$f v_n + \partial_x p_n = 0,$$
$$-f u + \partial_y p_n = Y_n,$$
$$\partial_x u_n + \partial_y v_n = 0.$$

Notice that $\partial_y v_n = -\partial_x(\frac{\beta}{f^2} + \frac{1}{f}\partial_y)p_n$ on the β-plane.

4. Numerical modeling of the Benguela upwelling system using MOM4

Numerical ocean models provide a useful tool to study the global ocean dynamics. Moreover, they can be extremely helpful by overcoming sparse field data. Two different numerical ocean models are used in this study. They are both based on the sub-release MOM4p1 of the Modular Ocean Model (MOM) that solves the hydrostatic Boussinesq equations on a spherical grid, see Griffies (2007).

While the one numerical model used in this study is a full realistic model driven by realistic winds and involving realistic topography, the other is designed as an idealized box model suitable for closing the gap in complexity between the analytical model and the realistic model or field observations. Both models are described shortly in the following two sections.

4.1. An idealized box model

The domain of the idealized box model is an enclosed, rectangular basin covering the area of 20°W to 0° and 10°S to 30°S. Whereas the latitude of the model covers roughly the latitude of the BUS, the choice of the longitude is somehow arbitrary. The model has a flat bottom and a straight coast as the eastern boundary located along the prime meridian. The horizontal grid resolution is 0.1°. The model is forced by a meridional wind stress of artificial shape corresponding to that of the analytical model. The wind forcing is symmetric around 20°S. Typical scales of the wind forcing with respect to the analytical model are $L = a = 5°$. The variable l can be varied between zero and five degrees. The zonal width of the wind band therefore is variable between five and ten degrees depending on the choice of the parameter l. The model domain of the numerical box model is presented together with the shape of the wind forcing in figure 4.1a.

At the latitude of 20°S, the length of 100 km equals ruffly one degree of longitude, and one degree of latitude equals about 111 km. Hence, the zonal scale of the forced area is comparable to that of the analytical model. In contrast, the meridional extent of the forcing area is roughly 100 km larger than that of the analytical model.

The water depth in the model is 1000 m and the water column is resolved by 200 equally spaced vertical layers. The initial stratification is horizontally and vertically homogeneous. This is achieved by using a constant potential temperature of 15 °C throughout the model domain and a linearly increasing salinity from $35\,\mathrm{g\,kg^{-1}}$ at the surface to $39\,\mathrm{g\,kg^{-1}}$ at the bottom. This results in a constant stratification of $N \approx 8 \cdot 10^{-3}\,\mathrm{s^{-1}}$.

Except for the wind forcing, there is no ocean-atmosphere interaction in the model. Therefore, vertical mixing in the box model is represented by constant mixing coefficients instead of an advanced vertical mixing scheme.

4.2. A realistic model

The realistic numerical model is designed as a regional ocean GCM. It consists of a physical model based on MOM4p1 and an embedded biogeochemical model on the base of ERGOM, see Fennel and Neumann (2004). The biogeochemical model is described in Schmidt and Eggert (2012), and the physical model is described in Herzfeld et al. (2011). However, this study analyzes only the physical results of the model.

4.2.1. Spatial and temporal discretization

The model domain stretches from the equatorial belt to the southern tip of Africa and from 10°W to the African coast, see figure 4.1b. This choice ensures to include the influence of equatorial currents and the SACW to the north as well as the ESACW to the south. The model grid consists of 382 and 273 cells in meridional and zonal direction, respectively. The horizontal resolution is highest on the shelf of Namibia and Angola where the grid cells have an approximate width of eight kilometers. This is in the order of the first internal Rossby Radius on the southwest African shelf. The vertical resolution is represented by 89 layers stretching with increasing depth. The highest vertical grid resolution is three meters and can be found in the top layer. The model is based on an Arakawa B-grid where the velocities are computed at the corners and the tracers, such as temperature or salinity, at the center of the grid cells.

The temporal discretization of the model uses mode splitting which takes into account the different time scales of barotropic and baroclinic processes. The baroclinic time step is chosen to be 1200 s, whereas the barotropic time step is 100 times larger.

4.2.2. Open boundary data

The model domain is connected to the ocean by two open boundaries: to the west and to the south. The data for the sea level, temperature, and salinity at these boundaries is derived from a global ocean GCM – the ECCO-model (http://www.ecco-group.org/). The boundary values for nutrients and oxygen are time independent and originate from the World Ocean Atlas (WOA).

The discharge of the 33 most important rivers along the model coast is considered.

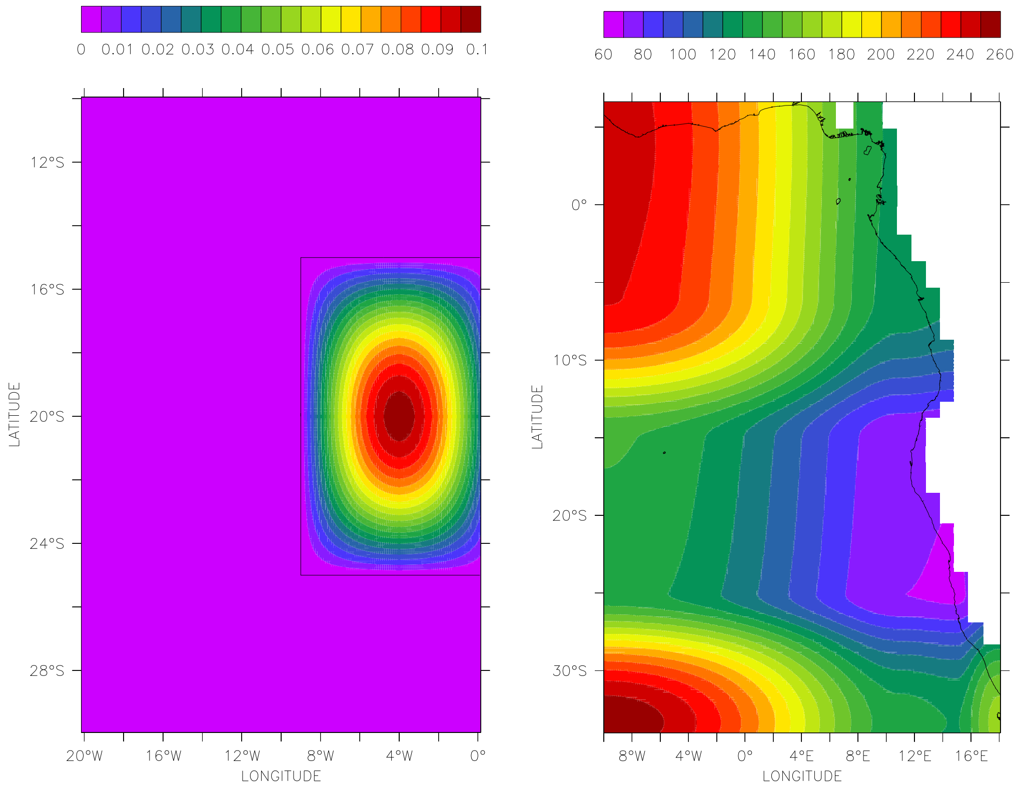

(a) Box model

(b) Realistic model

Figure 4.1. Domain of the numerical box model and the realistic numerical model. The color in (a) encodes an example of the meridional wind stress τ_y using $L = 5°$ and $l = 4°$ whereas in (b) the grid cell area [km^2] is shaded.

The bathymetry of the model is based on the ETOPO5 data set with a five minute spatial resolution.

4.2.3. Atmospheric forcing

The surface fluxes are calculated from model data of the National Centers for Environmental Prediction (NCEP). The wind forcing of the model is critical since the NCEP atmospheric model has a coarse spatial resolution of 1.875°, and remote sensing data exhibits usually a coarse temporal resolution. Therefore, wind stress data from an NCEP model and remote sensing data from the Quick Scatterometer (QuikSCAT) is combined to gain synthetic wind fields that have both high spatial (1/4°) and temporal (6 h) resolution. Since 2009 daily averaged wind stress fields from the Advanced Scatterometer (ASCAT) are used since the QuikSCAT mission ended. The switch of the wind products used for the atmospheric forcing of the model must be kept in mind when analyzing the model output. Bentamy et al. (2012) compared data from both scatterometers during their period of overlap (11/2008 to 11/2009) and found a persistent underestimation of ASCAT winds with respect to QuikSCAT.

4.2.4. Initialization

The model was initialized in the year 1999 with salinity and temperature data taken from the ECCO model. The initial nutrient and oxygen values originate from the WOA.

4.2.5. Computation

The computation of the model is performed at the North-German Supercomputing Alliance (HLRN). Until today, there exist several model runs covering the years 1999 to 2012. Usually, five-day averages of the model output are stored. In order to gain temporally higher resolved data, the data can be recomputed.

From the model output, a climatology of the most important physical and ecological data was calculated. In order to avoid a possible shift in the response due to the switch of the wind forcing products in the year 2009 the climatology was limited to the period of 2000 to 2008. Monthly averages presented throughout this study are based on that climatology.

4.2.6. Validation

Since the model is constantly developed further the validation of the results is an ongoing process. The latest validation of the model was performed by Muller (2013) who compared the general current pattern as well as the salinity and temperature distribution from the numerical model output with mooring data, remote sensing fields, and data from the WOA. Muller (2013) found that the model is able to simulate regional patterns and features across the Benguela region sufficiently well. In particular, the model represents the seasonal cycle of the currents appropriately. Nevertheless, some shortcomings of the model performance were reported. A time series of current data from a long term mooring on the shelf of Namibia suggested a possible overestimation of northward flow by the model and an underestimation of the poleward transport. Furthermore, a positive sea surface temperature (SST) bias of up to 2 K compared to remote sensing data was found in the northern BUS. A possible reason for this bias may be the coarse spatial resolution of the NCEP atmospheric forcing data that leads to wrong heat fluxes at the surface.

5. Current patterns in the Benguela upwelling system

5.1. The meridional currents

The basic response of the longshore flow to the sudden onset of a wind in eastern boundary upwelling systems is governed by an equatorward directed CJ in the mixed layer above a poleward directed undercurrent. Previous studies showed that these currents are modified if zonal variations of the wind stress are considered, e.g. Hurlburt and Thompson (1973), Johnson (1976), McCreary et al. (1987), Fennel and Lass (2007). The southward flow is strengthened and the PUC seems to near the surface. The observed surface poleward flow is often referred to as a counter current since it flows against the local wind.

The aim of this section is describing the interplay between Kelvin waves and zonally and meridionally varying wind stress in shaping the meridional flow along the coast of the BUS.

5.1.1. Near-surface patterns of the meridional currents

A horizontal view on the meridional surface currents derived from the analytical f-plane model 50 days after the onset of the wind is presented in figure 5.1. The wind maximum is located 425 km offshore of the eastern boundary which results in a strong WSC near the coast. The meridional near-surface currents comprise a southward intensifying, equatorward directed CJ and a weak poleward flow in the northern half. This poleward flow is driven by the strong WSC. The development of these patterns can be explained as follows: Kelvin waves are emanated at the northern edge of the forced area immediately after the onset of the wind; these waves travel southward and arrest the developing CJ at earlier stages (and therefore less strength) in the north due to their shorter traveling time. To the south, where the CJ has more time to develop, the CJ overcompensates the WSC driven poleward flow. Therefore, the CJ strengthens to the south while the poleward flow at the surface weakens. Southward propagating Kelvin waves are also responsible for the export of the CJ south of the forcing area, i.e. for $y \leq -500\,\text{km}$. Away from the eastern boundary, the meridional velocity increases and reaches a local maximum in the vicinity of the wind maximum at $x = -425\,\text{km}$.

A southward intensification of the CJ in the BUS is demonstrated by the dynamic topography derived from CTD data recorded during April and May 2004, see figure 5.2. The isobars in ten meter depth

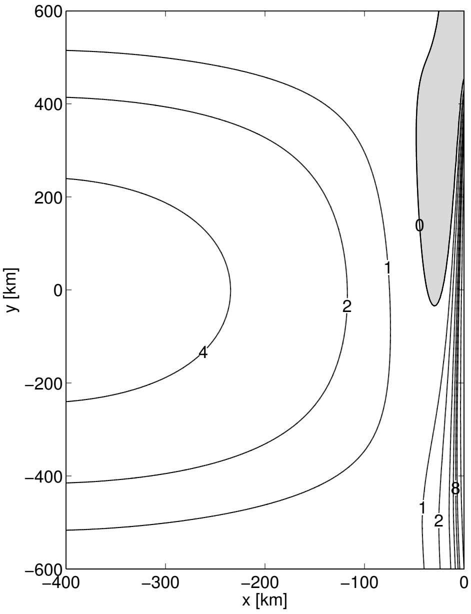

Figure 5.1. Near-surface meridional currents v [$\mathrm{cm\,s^{-1}}$] from the analytical f-plane model at 10 m depth 50 days after the onset of the wind. The wind maximum is located at $x = -425$ km. Negative currents (poleward directed) are shaded gray. The equatorward directed CJ intensifies to the south. The poleward surface flow in the north is a consequence of the WSC.

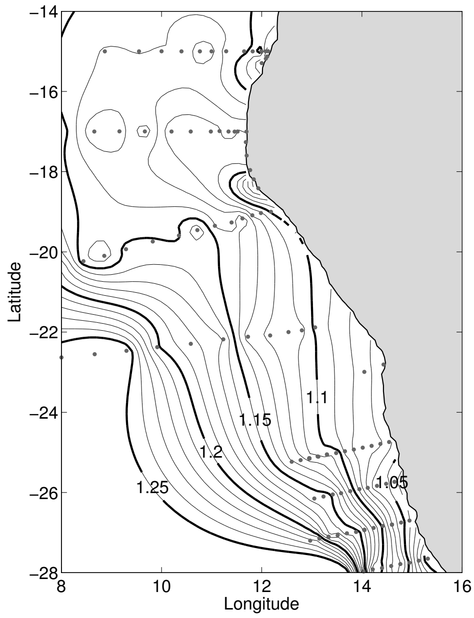

Figure 5.2. Dynamic topography [m] in ten meter depth derived from CTD data recorded during April and May 2004. The figure is redrawn from Mohrholz et al. (2008). The southward narrowing isobars imply a southward intensification of the equatorward directed geostrophic currents.

narrow to the south implying an intensification of the zonal pressure gradient. This in turn results in a southward intensification of the alongshore geostrophic currents.

However, the mean shape of the meridional flow in the BUS can barely be covered by observations. Numerical simulations can help to overcome this data gap. The mean meridional velocity in the surface layer (10 m) from the realistic numerical model is presented in figure 5.3 for January and July. The model data shows an equatorward directed CJ in the surface layer that is much more pronounced in July than in January. Beside that, a clear southward intensification of the CJ in both months is observed. In January, a surface poleward counter current is present seaward of the CJ. It stretches from 18°S to about 28°S. In July, the poleward directed surface current is poorly developed. The seasonal and interannual variation of the meridional transport and its relation to the wind forcing will be investigated in section 5.2.

Both the intensification of the CJ and the weakening of the poleward surface counter current to the south is predicted by the results of the analytical model. These findings suggest that the observed patterns of the poleward surface and subsurface flow in the BUS develop independently of the southward continuation of the AC along the African coast.

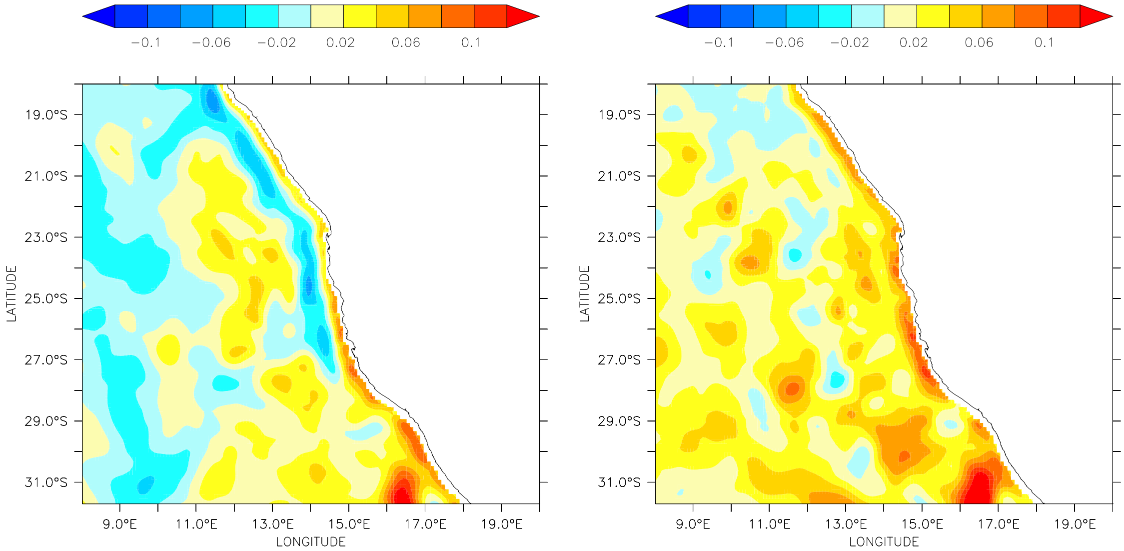

(a) January **(b)** July

Figure 5.3. Mean meridional currents [$\mathrm{m\,s^{-1}}$] in the surface layer (10 m) derived from the realistic numerical model for January and July. The southward intensifying CJ near the coast is more pronounced in July. In January, a poleward directed surface current adjacent to the CJ is observed.

5.1.2. Vertical pattern of the meridional currents

The mean meridional velocity from the realistic numerical model along five zonal transects from 16°S to 28°S is presented in figure 5.4. The equatorward directed CJ in the vicinity of the coast and the PUC are clearly observed. The PUC is strongest in summer and at the northernmost section where it reaches close to the surface. This is in accordance with the near-surface pattern of the meridional velocity presented in figure 5.3. The zonal sections reveal a southward deepening and weakening of the PUC in the BUS that has recently been reported by Veitch et al. (2010) and Muller (2013). The deepening is more apparent during winter (JJA) at the southernmost section when the poleward flow is limited to depth greater than 200 m.

The deepening of the PUC may be explained by noting that it is established by southward traveling coastal Kelvin waves. As the gravest wave modes are associated with the highest phase speeds, they reach further south than higher order modes. Therefore, only the gravest modes are involved in the generation of the PUC at higher latitudes. Following this concept, the vertical structure of the meridional currents along the latitude can be displayed as a function of the involved number of modes. A cumulative sum of the first twenty modes contributing to the meridional velocity near the eastern boundary is presented in figure 5.5. The minimum flow representing the core of the PUC is marked by dots. The data reveals a clear shoaling of the PUC the more modes get involved. In other words: the flow minimum can be found at higher depth if only the gravest modes contribute to the currents. These modes are associated with the highest vertical scales. These findings are in accordance with Philander and Yoon (1982). In the case of $R_1 = 50\,\mathrm{km}$, at least three modes are necessary to establish a minimum below the surface layer in the analytical model results. A decrease of the baroclinic Rossby Radius deepens and weakens the poleward alongshore currents, see figure

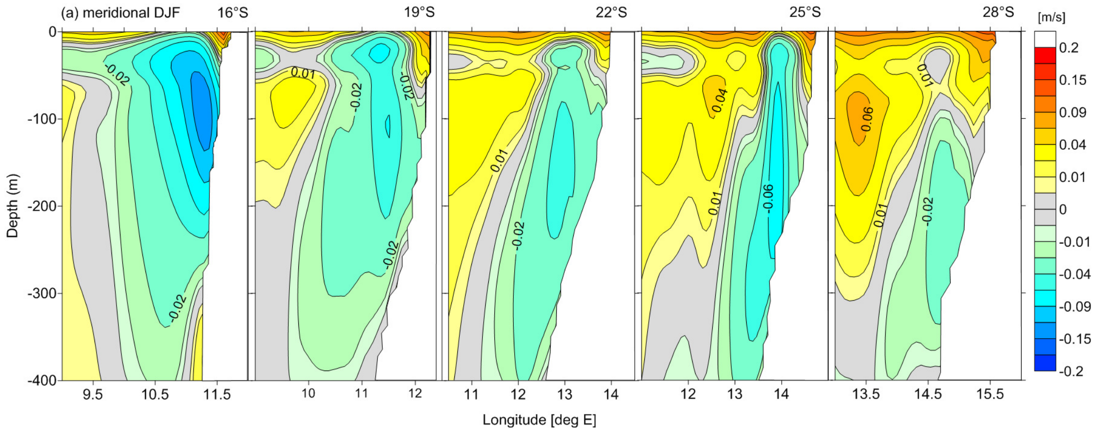

(a) DJF

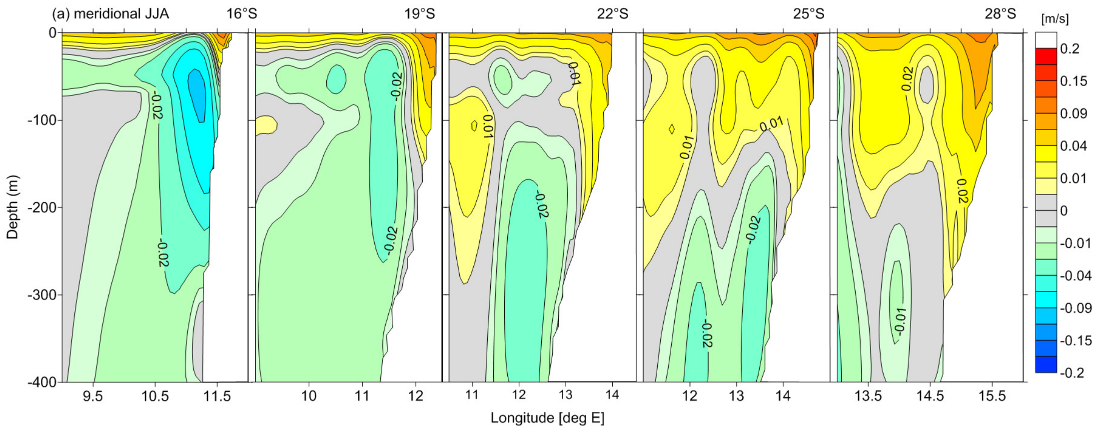

(b) JJA

Figure 5.4. Mean meridional velocity [$\mathrm{m\,s^{-1}}$] in the BUS through five different zonal sections between 16°S and 28°S during summer (DJF) and winter (JJA) taken from Muller (2013). The data reveals a southward deepening of the PUC.

5.5b. This makes sense since the Rossby Radius decreases if the stratification decreases; and the currents should become more barotropic in regimes where the stratification is weak, McCreary and Chao (1985).

The PUC exhibits seasonal variations concerning its mean depth. It is located deeper in winter than in summer especially south of 19°S, see figure 5.4. This corresponds to the seasonal variation of the stratification. Since the mean stratification is weaker in winter than in summer, and consequently the Rossby Radius is smaller, the PUC can be found at higher depth in winter.

The data presented in figure 5.4 also reveals an offshore migration of the PUC at higher latitudes that is more apparent in winter than in summer. This peculiarity may also be explained by the vertical mode structure of the meridional currents. The PUC gets less tightly trapped to the coast at higher latitudes when only the gravest modes are involved, Clarke (1989).

Basic properties of the vertical meridional flow pattern in the BUS may be explained by the vertical mode structure of the currents. Nevertheless, there may be various other reasons for the southward deepening and offshore migration of the PUC. For instance, topographic effects may play

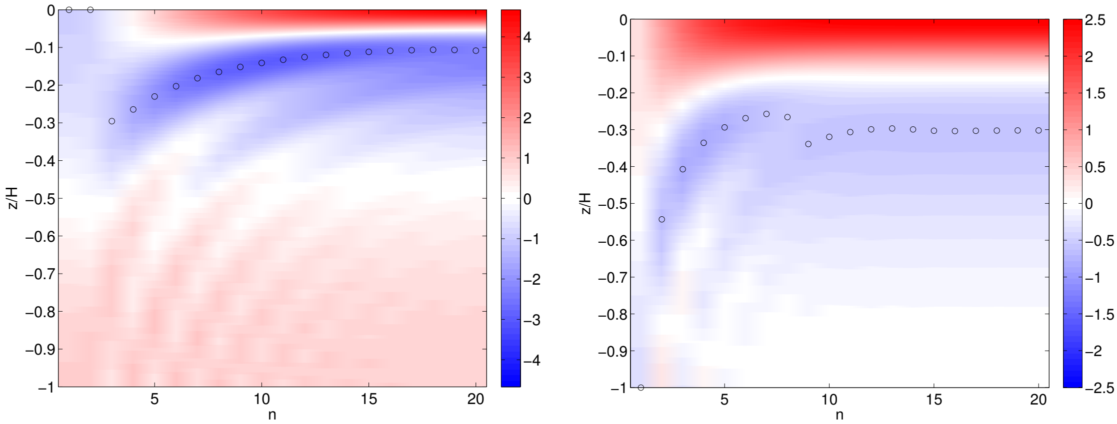

(a) $R_1 = 50\,\text{km}$ **(b)** $R_1 = 20\,\text{km}$

Figure 5.5. Cumulative sum of the first twenty modes contributing to the meridional velocity v [cm s^{-1}] from the analytical f-plane model. The currents were calculated closed to the eastern boundary in the middle of the wind band, i.e. at $y = 0$, $x = -10\,\text{km}$, for two different Rossby Radii. The wind maximum is located at $x = -400\,\text{km}$. The minimum flow representing the core of the PUC is marked by dots. The core of the PUC can be found at higher depth if only the gravest modes are involved.

a role since width and steepness of the shelf vary with latitude. Furthermore, the β-effect and the conservation of potential vorticity must be taken into account as proposed by Veitch et al. (2010).

5.1.3. Response to zonal variation of the forcing

The meridional velocity is shaped by an interplay of the coastal and the WSC dynamics as shown by results of the analytical model. The flow pattern in the vicinity of the coast are determined by the strength of the wind stress and the WSC near the eastern boundary. Both wind stress and WSC can be modified in the analytical model with the variation of the distance of the wind maximum to the coast.

Figure 5.6 presents the meridional velocity from the analytical f-plane model along the cross-shore coordinate x as a function of the distance of the wind maximum to the coast l. The strength of the WSC at the eastern boundary hereby increases with increasing l, whereas the wind stress weakens. The flow patterns are calculated for two different depth levels. At ten meters depth, a strong equatorward directed CJ ($v > 20\,\text{cm s}^{-1}$) exists in the vicinity of the coast for low values of l. This jet weakens for increasing WSC until it is overcompensated by the WSC driven poleward flow for values of $l \gtrsim 450\,\text{km}$. The surface counter current becomes apparent seaward of the CJ at $l \approx 420\,\text{km}$ and further increases in strength and offshore extension with increasing WSC. For a small range of l, the counter current and the CJ exist side by side. The poleward flow reaches its maximal offshore extent of about 100 km at $l = 500\,\text{km}$, i.e. when the WSC is strongest. The flow at 100 m depth is governed by the PUC in the vicinity of the coast. It has a constant offshore extent for $l \lesssim 400\,\text{km}$. For greater values of l the offshore scale increases to an extend that is similar to that in the surface layer.

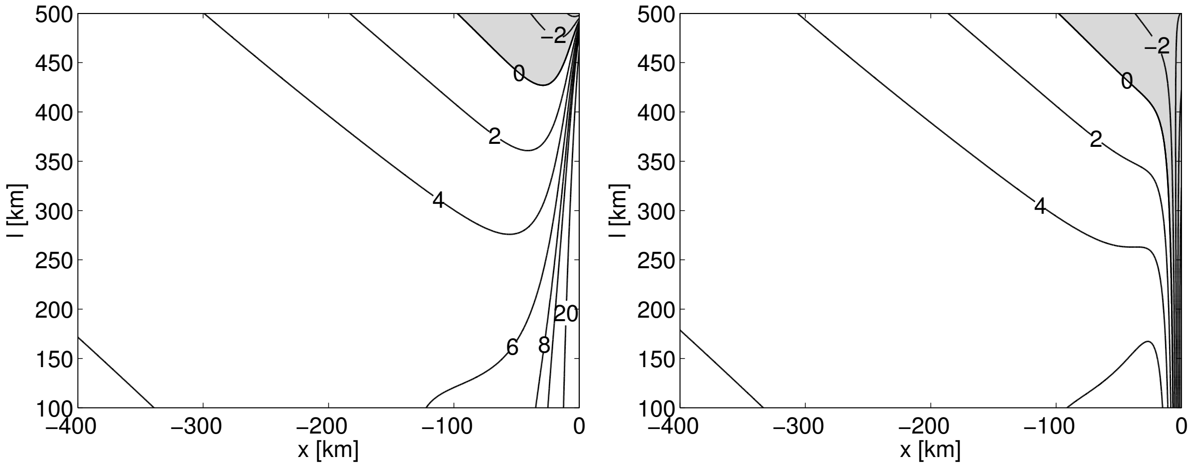

(a) $z = 10\,\text{m}$ **(b)** $z = 100\,\text{m}$

Figure 5.6. Meridional velocity v [cm s^{-1}] from the analytical f-plane model as a function of the distance of the wind maximum to the eastern boundary l and the zonal coordinate x for two depth levels 20 days after the onset of the wind. The currents are calculated in the middle of the wind band, i.e. at $y = 0$. Negative currents (poleward directed) are shaded gray. High WSC, i.e. for $l \gtrsim 420\,\text{km}$, introduces a poleward flow beside the PUC that is observed at $z = 100\,\text{m}$ in the very vicinity of the coast.

The poleward surface counter current that is often observed in field data and model results is explained by the analytical model on the f-plane. However, it must be pointed out that the spatial scales of the wind field at which that current occurs as well as the offshore scales of the poleward flow do not seem realistic. Moreover, the response is very sensitive to small shifts of the wind field. Using the example of January, the distance of the wind maximum to the coast is in the order of about 300 km at 23°S, see figure 3.4. In fact, a poleward surface current is clearly observed in model data at ten meter depth and stretching about 100 km offshore in January, see figure 5.3a. A solution to this contradiction is provided by the β-effect, see figure 5.7. The meridional flow patterns on the β-plane agree basically with those on the f-plane, although the overall poleward flow on the β-plane is enhanced. This is consistent with the results of McCreary and Chao (1985) who found that the β-effect acts to significantly weaken the equatorward flow and to slightly increase the poleward currents. The poleward counter current on the β-plane occurs already for $l \gtrsim 250\,\text{km}$, i.e. for lower WSC values as on the f-plane. The offshore extent of the poleward flow is about 150 km for $l = 300\,\text{km}$ and in the order of the observed values for January. The maximal offshore extent of the poleward surface flow increases to $x \approx -300\,\text{km}$ on the β-plane due to an enhanced trapping scale. Moreover, the response is not as sensitive to zonal changes of the wind field compared to the f-plane results.

The WSC introduces a poleward flow beside the PUC. Since the poleward surface current does not develop as a second cell or core beside the PUC it appears as a surfacing of the PUC. In fact, however, the surface counter current and the PUC result from different mechanisms as shown in the theoretical considerations in section 3.3.6. Whereas the PUC is introduced by Kelvin waves, the WSC driven poleward flow is not affected by coastal waves.

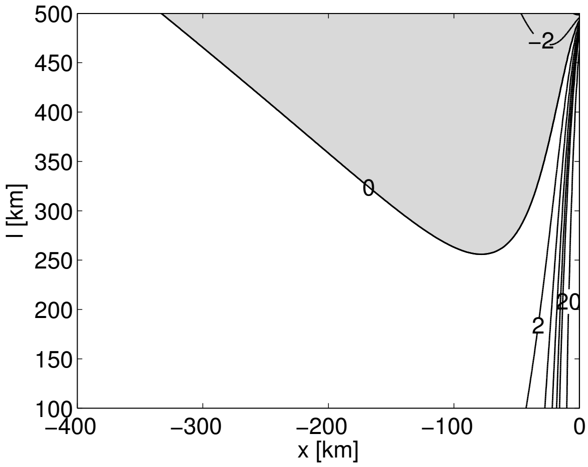

(a) $z = 10\,m$

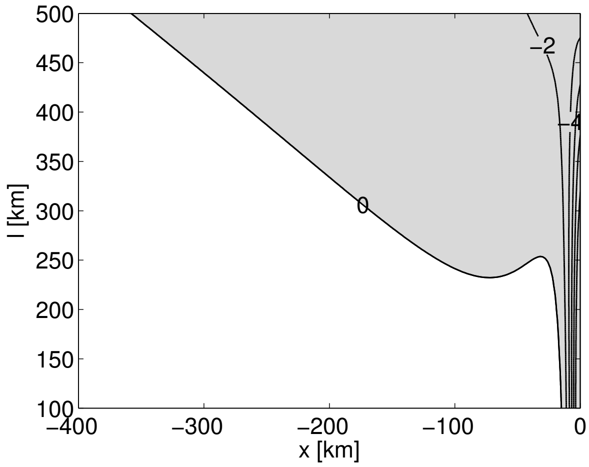

(b) $z = 100\,m$

Figure 5.7. Same as 5.6 but for the stationary part of the meridional velocity on the β-plane. The friction parameter is $r = 0.02\,f$. Negative currents (poleward directed) are shaded gray. The WSC induced poleward flow is observed already for lower WSC values on the β-plane, and the overall poleward directed flow is enhanced.

Results from the analytical models show that the existence of a WSC in eastern boundary upwelling systems increases the overall poleward flow. The poleward directed currents in the surface layer do not result from the β-effect since they can be explained by the help of the f-plane model. Nevertheless, the β-effect is needed to explain the currents structure using realistic scales of the wind field.

5.2. Temporal variability of the meridional transport

Results from the preceding section showed that there is a close connection between the meridional currents and the strength of the wind stress and the WSC. In this section, the response of the meridional transport to the seasonal cycle of the wind stress and the WSC in the BUS is studied. The investigations are based on data of the realistic numerical model and remotely sensed wind data.

Referring to Muller (2013), the meridional transport between the coast and the 300 m isobath is calculated and presented in figure 5.8a. The region north of 20°S was excluded from the calculation since the shelf becomes very steep there and the area between the coast and the 300 m isobath consists of only very few grid cells. The meridional transport is positive throughout the year south of 28°S but exhibits minima in the summer and maxima in the winter. North of that parallel, the direction of the meridional transport varies seasonally. It is directed southward in the summer and northward during winter. That distinct seasonal cycle is consistent with field observations, see Mohrholz et al. (2008). In most years, there exist biannual minima from October to November and February to March in the data. The meridional transport in the BUS exhibits strong interannual variations. A period of strong northward transport during the years 2000 to 2002 is followed by the years 2003 and 2004

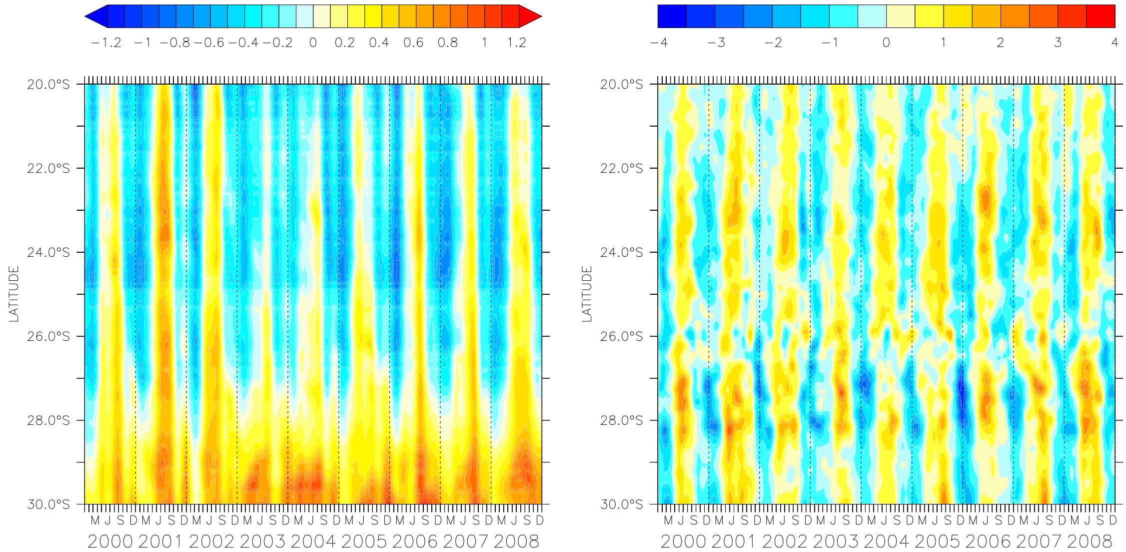

(a) Meridional transport **(b)** WSCA

Figure 5.8. Smoothed time series of the meridional transport [Sv] between the coast and the 300 m isobath and the WSCA [10^{-4} N m^{-2} km^{-1}] averaged over the same region. Notice that a positive WSCA corresponds to low values of absolute WSC. The meridional transport is in phase with the WSC except for a region between 25°S and 27°S. Even the biannual cycle of the WSC is mirrored in the meridional transport.

where the equatorward transport is rather weak. As a consequence, the seasonal variation during that period is relatively small. Long term data from a mooring located on the shelf at about 23°S confirms that the meridional transport in the year 2004 was exceptional negative compared to other years (V. Mohrholz, personal communication). The meridional transport is relatively homogeneous along the latitude north of about 25°S, but that latitude seems to denote a "boundary" at which, especially in the summer, the absolute meridional transport changes remarkably throughout the whole time series. Such latitudinal differences in the transport may of course rise from topographic variations along the shelf. South of about 28°S, the meridional transport is directed northward at all times. The change in direction between the seasons north of 28°S suggests a high seasonal variability in the cross-shore transport between 28°S and 26°S which is in accordance with findings of Muller (2013). The confluence zone between 26°S and 28°S coincides with the latitude to witch the existence of tropical SACW has been observed in model and field data, see e.g. Fennel et al. (2012) and Gordon et al. (1995).

In order to investigate the connection between the meridional transport and the WSC, a time series of the WSC anomaly (WSCA) along the latitude is shown in figure 5.8b. The data reveals a distinct seasonal cycle that is surprisingly uniform along the latitude regarding the latitudinal differences in the seasonal cycle of the wind stress. The WSCA is in the order of about 25 percent of the observed values for the WSC, compare to figure 2.4. The WSCA is in phase with the meridional transport except for a region between 25°S and 27°S where the WSC exhibits a high temporal variability. This region coincides with the location of the Lüderitz upwelling cell, where the wind maximum can be found close to the coast throughout all seasons, see figure 2.3. Positive values of the WSCA (referring to small absolute values of negative WSC) correspond to northward meridional transport, whereas

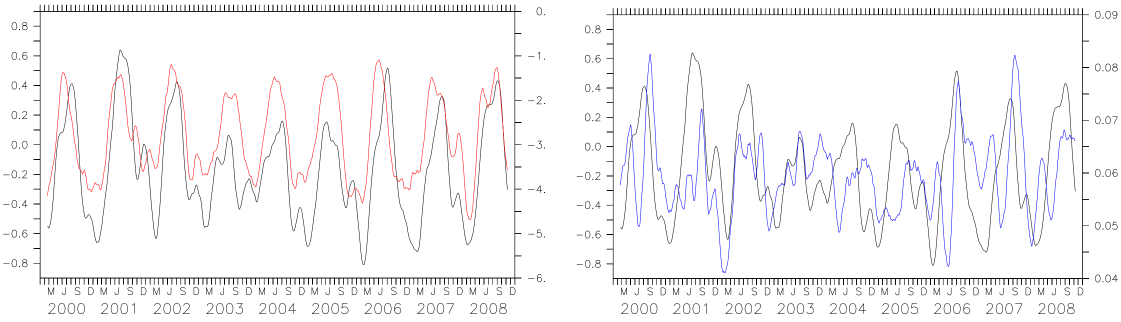

Figure 5.9. Smoothed time series of the meridional transport [Sv] (black, left axis) compared to (a) the WSC [10^{-4} N m^{-2} km^{-1}] (red, right axis) and (b) the meridional wind stress [N m^{-2}] (blue, right axis) at 24°S. The wind stress changes its phase in winter 2003/2004. This may explain the weak poleward flow around that time.

a negative WSCA is linked to poleward transport. There is also a biannual cycle in the WSC most pronounced north of about 24°S. It leads to minima in the WSCA around November and March observed most clearly during the years 2005 to 2007. These minima correspond to the biannual minima found in the meridional transport.

An example of the presented time series of the meridional transport and the WSCA is plotted in figure 5.9a at 24°S. The long term averaged meridional transport through that latitude is directed southward and amounts to about -0.16 Sv. The time series suggests again that there is a close coupling between the strength of the WSC and the strength and direction of the meridional transport along the shelf. A weak WSC leads to an equatorward transport, whereas strong values of (negative) WSC lead to a poleward transport.

Nevertheless, the WSCA does not explain the conspicuous interannual variations of the meridional transport. Since these variations are most pronounced during periods of northward transport (winter) the strength of the wind stress may provide an explanation. A smoothed time series of the meridional wind stress is presented in figure 5.9b. The data reveals a higher temporal variability than observed in the WSC. The seasonal cycle of wind stress and WSC, however, compare but exhibit a phase opposition concerning their strength, i.e. their absolute values. Small absolute WSC values correspond to maxima in the meridional wind stress. Therefore, high wind stress in winter corresponds to a northward transport. In winter 2003/2004, the wind stress changes its phase by about half a year and exhibits a maximum around December 2003 where a minimum is supposed. This wind stress maximum corresponds to the lowest southward transport in summer observed in the time series. From 2006 on, the wind is again in phase with the seasonal cycle of the WSC. Assuming that the wind stress drives a northward, whereas the WSC drives a southward meridional transport, a phase shift of the wind stress by about half a seasonal cycle would lead to weaker northward transport in winter and weaker southward transport in summer in the BUS. This mechanism may provide an explanation for the observed interannual variations in the meridional transport. Nevertheless, remote effects such as coastally trapped waves may also play a role in causing interannual variabilities of the meridional transport.

Lass and Mohrholz (2008) reported biannual maxima in the coastal sea level elevation along the southwest African coast in September to November and February to April and related them to an equatorial Kelvin wave and a freshwater surplus in the eastern tropical Atlantic. These maxima match with observed biannual minima in the meridional transport presented in this study. Indeed, this fact does not contradict the findings of Lass and Mohrholz (2008) since a positive sea surface anomaly is geostrophically balanced by a southward transport anomaly. However, this study suggests that the meridional transport and the sea level variation in the BUS are triggered by the WSC. Interannual variations in the meridional transport may be explained by variations of the phase and strength of the wind stress.

5.3. Cross-shore circulation in inhomogeneous wind fields

5.3.1. General patterns

Spatial inhomogeneities of the wind field in both meridional and zonal direction introduce a contribution to the zonal velocity beside the Ekman transport and its rectification in the subsurface layer, see section 3.3.6. This additional component was referred to as WSC dynamics although it is linked as well to the divergence of the wind field. The major aim of this section is to elucidate the role of both the Ekman and the WSC regime in shaping the zonal velocity.

The near-surface zonal velocity from the analytical model is compared to the outcome of the numerical box model in figure 5.10. The presented data is an average over the first ten days after the onset of the wind. The averaging filters out inertial effects in the numerical model data that are not captured by the analytical model. For comparability, the analytical model results are averaged over the same period of time. The near-surface zonal currents in the analytical model results are negative almost throughout the entire forcing area since they are dominated by the Ekman offshore transport, see figure 5.10a. In the southern half of the wind patch, the offshore flow faces an onshore transport caused by the WSC dynamics. In contrast, in the northern half of the wind band, the Ekman transport is supported by an offshore flow. The resulting zonal surface currents exhibit a clear north-south asymmetry. In the numerical box model, the WSC dynamics is rather weak compared to the analytical model results, see figure 5.10b. This is clearly seen in the weaker onshore transport in the southern half resulting in less distortion of the isotachs in the forced area. The different representation of the WSC dynamics in both models can have many causes. Beside the fact that various approximations went into the calculations of the analytical model results, both models are not comparable one-to-one in many respects. Friction, for instance, is parametrized in a different way in the numerical model compared to the analytical model. The mixed layer depth and the stratification may also differ slightly. Enhanced friction would reduce the influence of the WSC dynamics on the zonal flow, see equation (3.47), and a shallower mixed layer depth would strengthen the Ekman transport. Another reason for the different representation of the WSC dynamics in both models may be due to the fact that the meridional extent of the wind band in the numerical model is slightly larger than in the analytical model, see section 4.1. This leads as well to an underestimation of the WSC dynamics in the numerical model. Nevertheless,

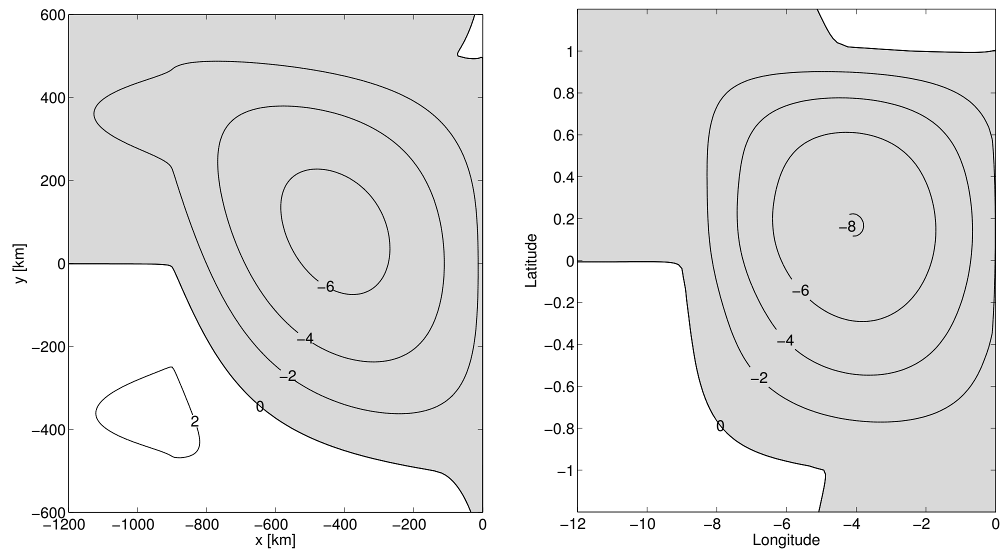

(a) Analytical model **(b)** Numerical box model

Figure 5.10. Near-surface zonal velocity u [cm s^{-1}] at 7.5 m depth from the analytical f-plane model and the numerical box model averaged over the first ten days after the onset of the wind. The wind maximum is located at $x = -400$ km. The latitude in (b) has been centered and normalized by the length of the wind band for comparability with figure 5.12. Negative currents are shaded gray.

the effect of the WSC dynamics on the zonal currents is reproduced by the numerical model not least because of the strict north-south flow separation west of the wind band.

A meridional section of the zonal velocity from the analytical model 100 km off the eastern boundary is shown in figure 5.11a. As discussed already, the flow in the mixed layer is dominated largely by the Ekman offshore transport. Below the surface mixed layer, the currents are governed by the WSC dynamics that separates the response in a northern half where the flow is directed offshore and a southern half where the flow is onshore directed. The zero isotach separating those regions is slightly shifted to the north due to a small onshore contribution of the Ekman rectification flow along the whole transect. This contribution to the currents below the mixed layer is also the reason why the onshore directed flow in the south is stronger than the offshore currents in the northern half. The currents below the mixed layer are dominated by the barotropic signal because the WSC dynamics is proportional to the square of the Rossby Radius, see equation (3.47).

The vertically integrated and normalized velocity in the mixed layer and the layer below is shown in figure 5.11b together with the forcing function in meridional direction and its derivative. The data reveals again that the zonal circulation in the mixed layer is basically proportional to the wind forcing, whereas the dynamics below the mixed layer is linked to the divergence of the wind forcing. The northward shift of the mixed layer maximum flow against the wind maximum is a typical characteristic of the interplay of the WSC and the Ekman regime. Another peculiarity in that system is the shift of the sub-surface integrated flow maxima and minima from the edges of the wind band towards the wind maximum.

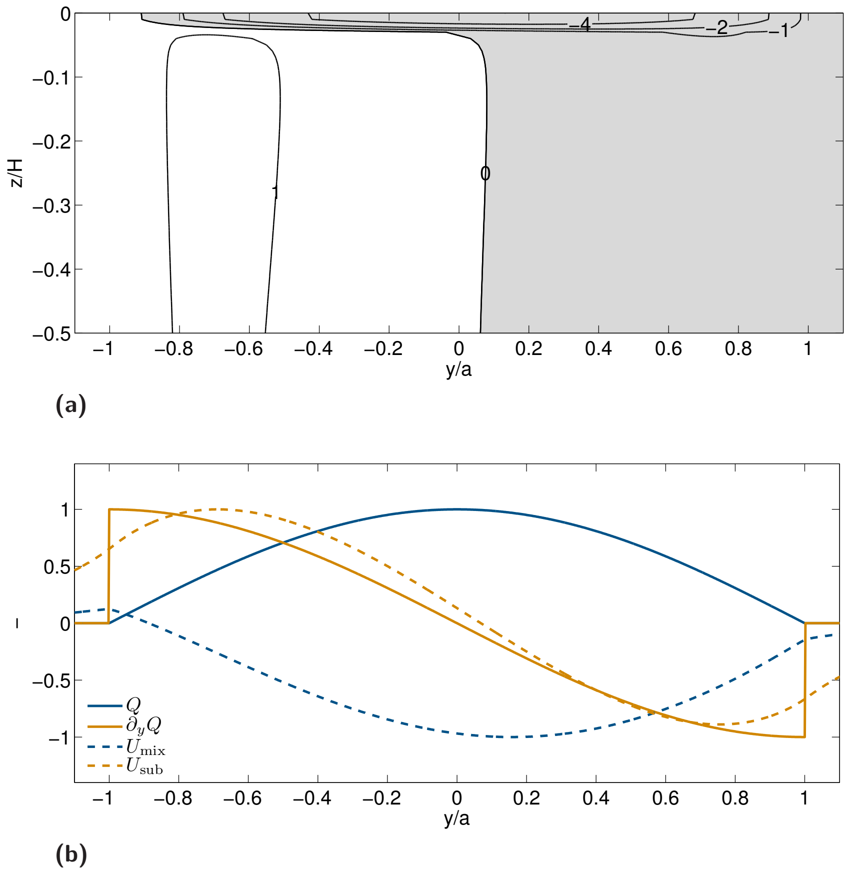

Figure 5.11. (a) Zonal velocity u [cm s^{-1}] from the analytical f-plane model along a meridional transect, i.e. at $x = -100$ km, 20 days after the onset of the wind. Only the upper half of the water column is shown for clarity. The wind maximum is located at $x = -100$ km. Negative currents are shaded gray. (b) Comparison of the normalized vertically averaged zonal currents presented in (a) in the mixed layer (0 to 20 m) and the layer below (20 to 300 m) to the wind forcing functions Q and $\kappa^{-1}\partial_y Q$.

5.3.2. Response to a varying length of the wind band

Since the response of the ocean that is related to the WSC is proportional to the divergence of the wind field, the meridional scale of the wind band should influence the zonal currents. The analytical model predicts an enhanced contribution of the WSC dynamics to the zonal velocity if the meridional scale of the wind band decreases, see section 3.3.6. This would express, for instance, in an intensification of the surface onshore flow in the southern half of the wind band. In order to evaluate the analytical model results in that respect, two runs with the numerical box model for two different lengths of the wind band were performed.

A horizontal view on the near-surface zonal currents from these model runs is shown in figure 5.12. The latitude is centered and scaled by the length of the wind band for comparability purposes. In order to evaluate the different time evolution of the WSC dynamics and the Ekman transport by the way, the results have been averaged this time over the days 10 to 20 after the onset of the wind. Whereas the Ekman transport adjusts immediately after the onset of the wind, the WSC dynamics develops with a time constant being the friction rate ($r^{-1} \approx 10$ d), see section 3.3.6. A comparison

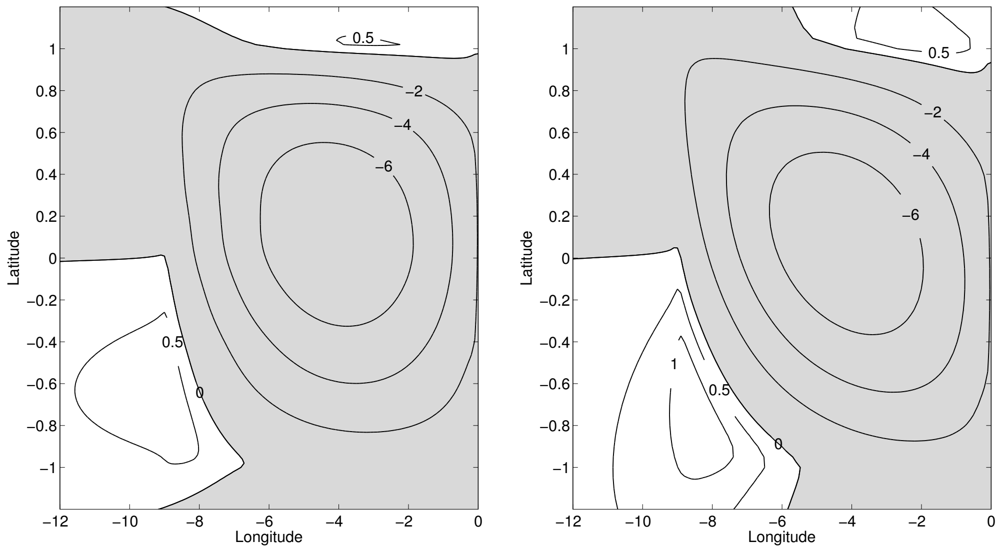

(a) $a = 5°$ **(b)** $a = 2°$

Figure 5.12. Near-surface zonal velocity u [$\mathrm{cm\,s^{-1}}$] at 7.5 m depth from the numerical box model averaged over the days ten to twenty after the onset of the wind for two different lengths of the wind band. The wind maximum is located at 4°W and the western edge of the wind band at 9° W. The latitude has been centered and normalized by the length of the wind band for comparability. Negative currents are shaded gray.

of the figures 5.10b and 5.12a confirms the analytical model results in that respect since the onshore transport in the southern half of the wind band is stronger as more time elapsed after the onset of the wind.

The zonal velocity at the southwestern corner of the wind band is remarkably increased when the length of the wind band is decreased, see figure 5.12. The offshore transport in the southeast of the model domain is weakened. Consequently, the convergence zone between the onshore and the offshore flow in the southern half is shifted towards the coast. Moreover, the offshore flow in the northwestern forcing area increased slightly, and in the northeast, the onshore flow (that is also part of the WSC regime) increases.

As a summary it may be stated that inhomogeneities of the wind field in both meridional and zonal direction modify the classical picture of the zonal currents in upwelling systems. The dynamics caused by the inhomogeneity of the wind field introduces an onshore (offshore) flow in the southern (northern) half of the wind band. Whereas the flow in the mixed layer is basically governed by the Ekman currents, the WSC dynamics dominates below the mixed. The smaller the wind scales, the more important the WSC contribution becomes.

5.4. Cross-shore dynamics in the very northern Benguela upwelling system

The results of the analytical theory show that there is a distinct north-south asymmetry of the zonal flow in systems with high inhomogeneities in the wind stress. This may be a reason for the remarkably northward spreading of cold upwelled water that can often be seen in remotely sensed SST data, e.g. Fennel et al. (2012). Indeed, the existence of a frontal band (detected in SST and chlorophyll *a* data) appearing to be more diffusive in the northern BUS than in the southern was already reported by Shannon (1985). However, there is no indication for a persistent surface onshore flow in the southern BUS from observations or the realistic numerical model. As the coast of southwest Africa is not strictly orientated meridionally and, more importantly, changes its orientation, computing the onshore velocity component along the entire coast of the BUS is not trivial. Apart from that, a likely reason why this peculiarity is not observed is the meridional scale of the winds in the BUS. As estimated in section 3.3.6, the meridional scales of the wind band at which the WSC dynamics becomes important for the zonal velocity must be comparable to (or smaller) than the zonal wind scales. If we consider the zonal wind scales in the BUS to be determined by the WSC, the meridional scales must not exceed a few hundred kilometers. Thus, the effect of the WSC dynamics on the zonal velocity in the entire BUS can assumed to be weak. But the situation might be different in regions of enhanced meridional wind stress close to the coast that are characterized by high wind stress divergence such as off Lüderitz and in the Cape Frio region, see figure 3.5. Therefore, this section is dedicated to the investigation of the cross-shore dynamics and its relation to the wind forcing in the Cape Frio region.

5.4.1. The Cape Frio cell

The area between 15°S and 19°S located off Cape Frio is referred to as the Cape Frio cell (CFC) in this study. The CFC can be considered as the northern gate to the BUS for tropical waters. The poleward surface and subsurface continuation of the AC transports nutrient rich and oxygen poor SACW through that region into the northern Benguela ecosystem. The dynamics in the CFC are therefore highly relevant for the biogeochemical conditions on the shelf of southwest Africa. Recent comparisons of the cross-shelf and along shelf transport budgets in the northern BUS based on realistic model data presented by Muller (2013) show that the annual mean cross-shelf transport between 16°S and 19°S is nearly of the same amount as the longshore transport through 16°S but exhibits a higher seasonal variability. These findings suggest an enhanced influence of the cross-shelf transport on the ecosystem variability in comparison with the meridional currents.

The CFC is characterized by a very pronounced and persistent wind patch with a mean wind maximum located at about 17°S in a distance of about 50 to 100 km to the coast, see figure 2.3. It has a meridional extent of about 400 to 500 km. The shelf in that region is very narrow and steep and changes drastically to the south, see figure 2.1.

5.4.2. Zonal currents in the Cape Frio cell from observations and model data

Beside the poleward continuation of the AC, a partly offshore bending of that flow between 15°S and 19°S is indicated in several studies but not discussed, e.g. Mohrholz et al. (2001), John et al. (2004), Colberg and Reason (2006). However, field data is very rare in that region and observations

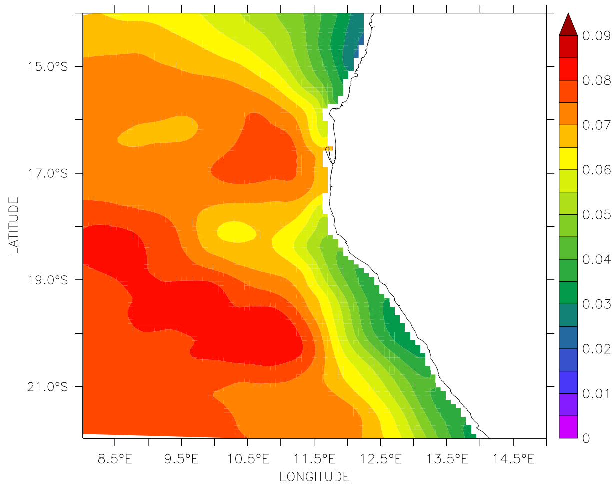

Figure 5.13. Remotely sensed meridional wind stress component [N m^{-2}] off Cape Frio averaged from April to May 2004. The wind mimics the typical forcing conditions with a wind maximum around 17°S located about 100 km off the coast.

are mostly based on meridionally oriented transects that follow the cross-shelf gradients, e.g. Lass et al. (2000), Mohrholz et al. (2001).

A map of the dynamic ocean topography derived from CTD data in the northern BUS was presented already in figure 5.2. This data suggests a negative geostrophically balanced zonal current component north of about 17°S and an onshore contribution south of that parallel. The meridional wind component derived from remote sensing data during that time is shown in figure 5.13. The wind conditions mimic the typical forcing condition in that region. A wind maximum at about 17°S in a distance of about 100 km to the coast is observed. The wind drops sharply to the north and south of the maximum resulting in high wind stress divergence.

A possibility to receive an impression of the mean currents in the CFC is provided by the mean dynamic ocean topography (MDOT). The MDOT is derived from the mean sea surface height by subtracting the geoid, Maximenko et al. (2009). It represents the ocean topography that is balanced by the mean barotropic geostrophic currents. Data covering the years 1992 to 2002 was downloaded from the Asia Pacific Data-Research Center (http://apdrc.soest.hawaii.edu/projects/DOT) to compute the geostrophic zonal velocity in the CFC. The result is shown in figure 5.14a. In the data, an area of westward flow from about 17.5°S to 16°S can be recognized northward of an area of intense onshore flow although the spatial resolution is coarse and data in the vicinity of the coast is missing. A better spatial resolution of the geostrophic zonal velocity can be derived using realistic model data. The geostrophic zonal velocity was calculated from the mean sea surface elevation of the years 2000 to 2008 and is presented in figure 5.14b. The data has been removed along a coastal strip to exclude ageostrophic effects like the Ekman currents. Although both data cover different periods, the model data is in accordance with the general structure of the MDOT. Only the area of negative zonal flow south of 19°S in the model outcome stretches further onshore compared to the observations.

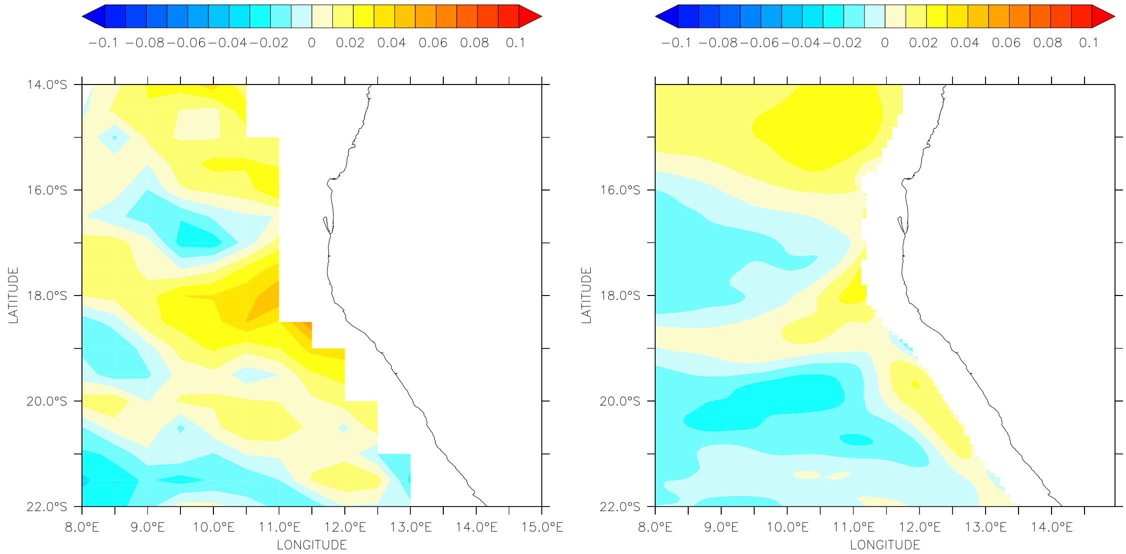

(a) MDOT **(b)** Realistic numerical model

Figure 5.14. Mean barotropic geostrophic zonal velocity [$\mathrm{m\,s^{-1}}$] off Cape Frio calculated from the mean dynamic ocean topography (MDOT) and from the mean sea surface height of the realistic numerical model. The data in (b) has been removed along a coastal strip to exclude ageostrophic effects. The data reveals an offshore flow around 17°S and an area of onshore transport south of it.

Ocean GCMs offer the opportunity to directly investigate the mean currents. The mean zonal velocity from the realistic numerical model is shown for the area around Cape Frio in figure 5.15. The averaged surface (0 to 30 m) and subsurface (30 to 300 m) currents are hereby displayed separately and the mean flow direction is indicated by arrows. The surface zonal velocity is presumably dominated by the Ekman transport and therefore negative in the entire CFC. The flow is strongest in a broad zonal band between about 16°S and 18°S. This band is associated with the westward deflection of the southward flow along the Angolan coast as the arrows indicate. The same band of negative zonal flow associated with a partly westward bending of the AC can be observed in the subsurface layer, although the velocity is rather weak and the mean flow is not strictly directed eastward. Moreover, the arrows indicate a partly southward recirculation into a band of positive zonal velocity that stretches from the coast up to 19°S and 8°W.

The mean vertical patterns of the cross-shore flow in the CFC are investigated along a meridional transect derived from the realistic numerical model for August, see figure 5.16. The data shows an offshore flow stretching over almost the whole water column north of 17°S with the strongest values found in the surface layer. This offshore flow is probably supplied by the westward bending branch of the AC. South of 17°S, the flow is directed offshore in the surface layer and onshore below. The location of zero velocity below the mixed layer coincides roughly with the location of the mean wind maximum in the CFC.

The vertical and near-surface patterns of the mean zonal velocity off Cape Frio observed in field data and numerical model data compare well to the findings of the analytical model. This strengthens the idea that the wind forcing is crucial for shaping the zonal currents in that region. Thus, the spatial shape of the wind patch off Cape Frio has an important impact on the cross-shelf exchange and

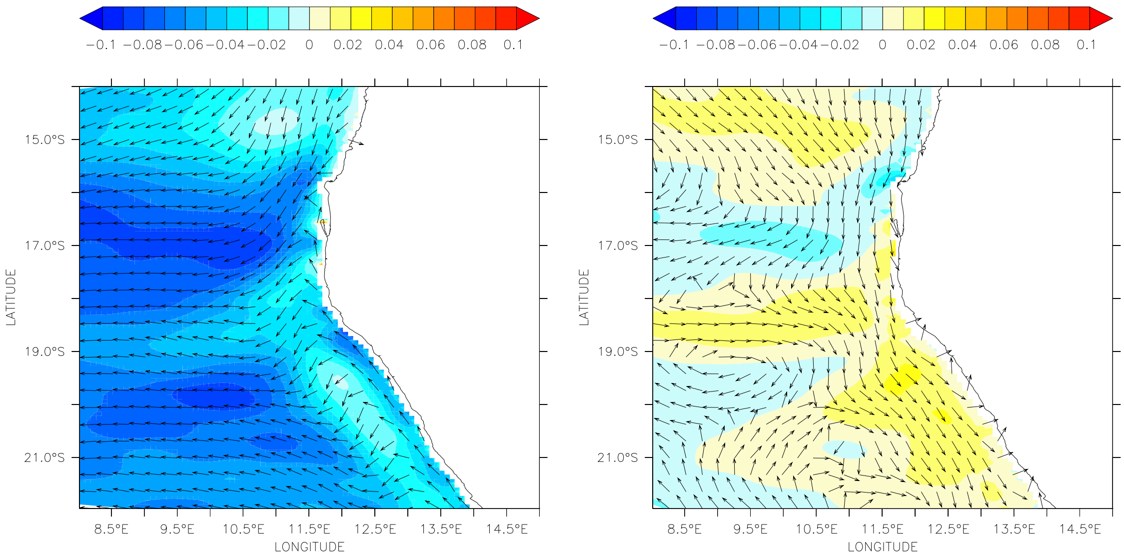

(a) 0 to 30 m **(b)** 30 to 300 m

Figure 5.15. Mean zonal velocity [m s^{-1}] off Cape Frio from the realistic numerical model averaged over the surface layer (0 to 30 m) and the layer below (30 to 300 m). The mean flow direction is indicated by arrows. The band of offshore flow around 17°S in the layer of 30 to 300 m is related to a partly westward bending of the southward flow along the African coast.

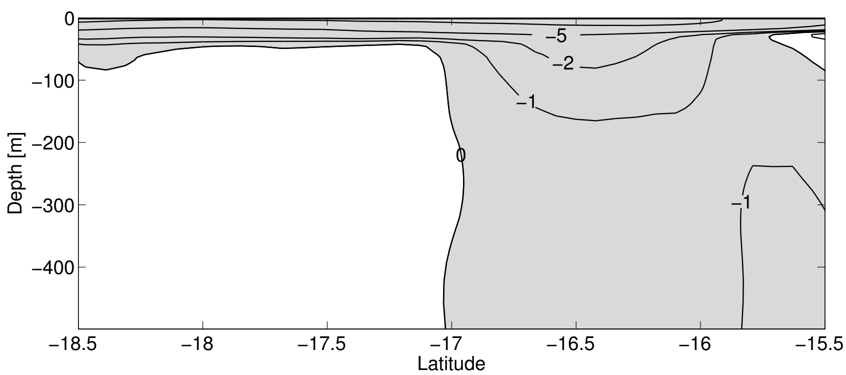

Figure 5.16. Mean zonal velocity [cm s^{-1}] from the realistic numerical model along 11°E in August. Only the upper 500 meters are shown for clarity. Negative currents are shaded gray.

the penetrability of tropical waters along the coast into the BUS. The wind forcing off Cape Frio may modify the southward advected SACW not only by upwelling, see Mohrholz et al. (2001), but also by transporting water of tropical origin from the shelf westward replacing it by water of more oceanic character. Nevertheless, it still needs some work to relate possible seasonal and interannual variations of the zonal transport to the shape and strength of the wind forcing in the Cape Frio cell.

The crucial role of the wind forcing off Cape Frio may provide an explanation, among others, for upper ocean temperature biases that are often observed in coupled GCMs along the southwest African coast, see Xu et al. (2013) and references therein. An underestimation of the meridional and zonal inhomogeneities of the wind field in the CFC may lead to an erroneous representation of the zonal

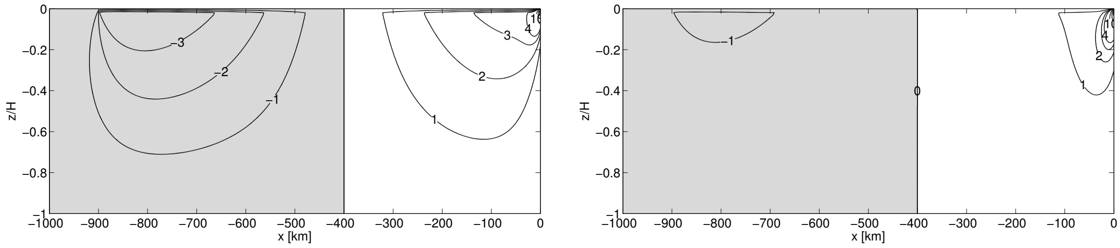

(a) $y = 0$ **(b)** $y = -400$ km

Figure 5.17. Zonal sections of the vertical velocity w [10^{-4} cm s^{-1}] from the analytical f-plane model 50 days after the onset of the wind in the middle of the wind band, i.e. $y = 0$, and near the southern edge, i.e. $y = -400$ km. The wind maximum is located at $x = -400$ km. Negative currents are shaded gray.

currents in that region. This in turn may lead to an overshooting of the AC and an overestimated advection of warm, tropical waters into the BUS as reported by Xu et al. (2013).

5.5. Upwelling dynamics

5.5.1. General patterns

As pointed out in section 2.2 there are two main upwelling mechanism that play a role in the BUS. Coastal upwelling is driven by the Ekman divergence in the vicinity of the coast and is influenced by coastally trapped waves. WSC driven upwelling, however, acts independently of the coastal inhibition. This section investigates the spatial patterns of the vertical velocity related to both upwelling mechanism. Elucidating the relative importance of WSC driven and coastal upwelling in the BUS is another aim of this section.

Two zonal sections of the vertical velocity from the analytical f-plane model are presented in figure 5.17. The data was calculated at two different latitudes 50 days after the onset of the wind. At both latitudes, the maximum upwelling can be found in the vicinity of the coast. The vertical velocity here reaches values of more than 10^{-3} cm s^{-1}. In the middle of the wind band, i.e. at $y = 0$, the vertical velocity exceeds values of 1 cm s^{-1} up to 300 km offshore. These currents are related to the WSC. Near the southern edge of the wind band, i.e. at $y = -400$ km, where the wind stress (and consequently the WSC) is weaker, the upwelling is limited to the near coastal area. Although the wind stress is weaker near the southern edge of the wind band, the vertical velocity in the vicinity of the coast is enhanced compared to the values in the middle of the wind band. This is a result of Kelvin waves that carry the upwelling signal southward, see also Fennel et al. (2012). The vertical velocity is positive for $x > -l$, i.e. for the region where the WSC is negative, and downwelling occurs where the WSC is positive, i.e. for $x < -l$. The highest velocity values in the offshore half of the wind band can be found towards the edge of the wind band where the WSC is strongest and in the vicinity of the mixed layer. Notice that the response pattern of the WSC driven upwelling would be almost symmetric around $x = -l$ if $l = L$.

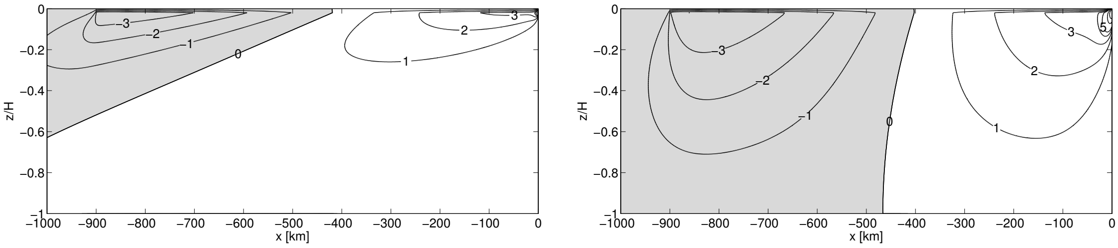

(a) $r = 10^{-3}\, f$ (b) $r = 0.02\, f$

Figure 5.18. Zonal sections of the steady state vertical velocity w [10^{-4} cm s^{-1}] from the analytical β-plane model for two different friction parameter. The wind maximum is located at $x = -400$ km. Negative currents are shaded gray. In contrast to the f-plane results, the zero isotach is tilted. The tilting is reduced if friction increases.

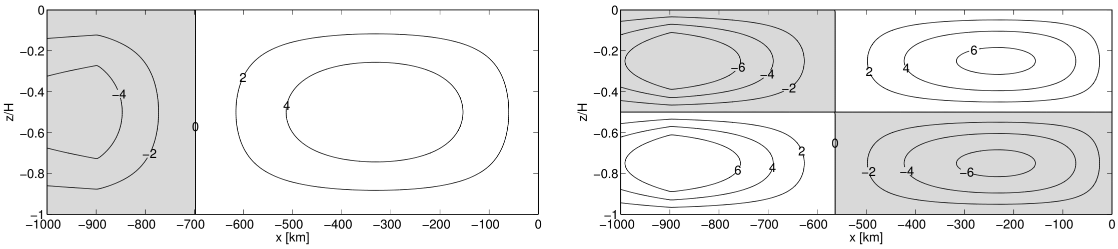

(a) First mode (b) Second mode

Figure 5.19. First and second mode contribution to the steady state vertical velocity w [10^{-5} cm s^{-1}] from the analytical β-plane model. Negative currents are shaded gray. The vertically oriented zero isotach is shifted onshore for higher order modes since the zonal trapping scale of Rossby waves decreases.

The steady state vertical velocity on the β-plane is shown in figure 5.18. The steady state response on the β-plane corresponds to the equilibrium state adjusted by Rossby waves after the onset of the wind. In contrast to the f-plane solution, the response on the β-plane is not strictly connected to the shape of the wind forcing. In particular, the upwelling area reaches slightly further offshore than the wind maximum located at $x = -l$. Moreover, the zero isotach (oriented vertically on the f-plane) is tilted. The vertical structure of the vertical velocity component including the tilting can be explained regarding the response as a sum of modes. The sign of the first mode response is uniform throughout the water column being negative in the western and positive in the eastern part, see figure 5.19a. The sign changes at a certain location, i.e. at $x \approx -700$ km in this example. The second mode changes its sign further onshore at $x \approx -560$ km, see figure 5.19b. This is a result of the fact that the trapping scale is mode dependent and exceeds the zonal wind scale on the β-plane, see section 3.4.5. The higher the mode number the smaller the trapping scale and the closer the vertically oriented zero isotach comes to the coast. Additionally, the second mode becomes zero in the middle of the water column, i.e. at $0.5\, H$. The vertical velocity in the upper water column is negative (positive) in the western (eastern) part and vice versa for the lower water column. Adding the second to the first mode extends the negative velocity area in the upper water column to the east and the positive area in the lower water column to the west. At the same time, the second order mode introduces an area of negative vertical velocity to the lower water column in the eastern part. Therefore, the basic pattern in figure 5.18a can not be reproduced by involving only the two gravest modes. Calculations including higher order modes reveal that these modes contribute substantially

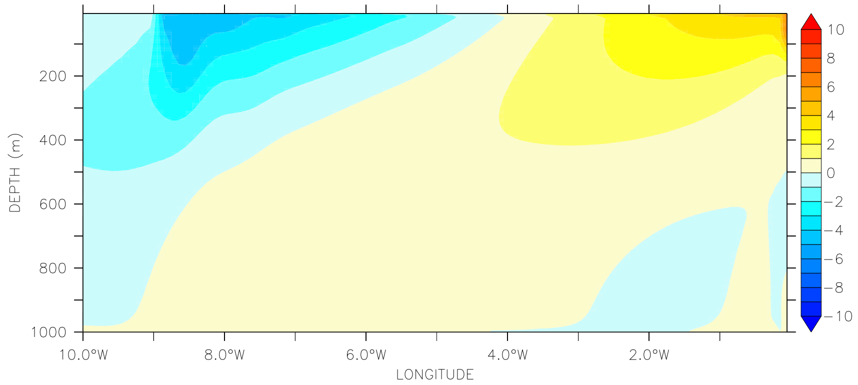

Figure 5.20. Zonal section of the vertical velocity $[10^{-4}\,\mathrm{cm\,s^{-1}}]$ from the numerical box model in the middle of the wind band averaged over one year after the onset of the wind. The wind maximum is located at 4°W. The results compare well to the findings of the analytical model. The tilting of the zero isotach is clearly observed.

to the response. Since enhanced friction reduces the zonal trapping scale, see section 3.4.5, the downwelling area should be shifted towards the eastern boundary with increasing friction on the β-plane. Moreover, the differences of the trapping scale between the single modes increase with an increase of the friction parameter. The tilt of the zero in the response should therefore become less pronounced. In fact, both processes are captured by the results presented in figure 5.18b. Here, a friction parameter of $0.02f$ has been used. Notice that the response gets closer to the f-plane results as the friction is enhanced.

Coastal upwelling is not captured in the β-plane results when friction is set to relatively small values, see figure 5.18a. This is a consequence of less damping of Kelvin waves that are known to reduce and export coastal upwelling to the south. A higher friction parameter, however, limits the influence of Kelvin waves and the upwelling intensity near the cost increases, see figure 5.18b.

A zonal section of the mean vertical velocity derived from the numerical box model is presented in figure 5.20. The result of the numerical simulation corroborates the analytical solution regarding its shape and absolute values. The positive upwelling area stretches slightly further offshore than the location of the wind maximum at 4°W in the numerical results. The tilt of the zero isotach is clearly observed. The downwelling is strongest near the offshore edge of the wind band, i.e. at 9°W, and an area of intense upwelling in the vicinity of the coast is observed. However, the areas of slight negative vertical velocity between about 3°W and 0° in the lower water column are not captured by the results of the analytical model.

An example of a zonal section of the mean vertical velocity from the realistic numerical model at 24°S is shown in figure 5.21. The mean WSC at that latitude is negative up to about 11.8°E and positive further offshore (not shown). The upwelling has two maxima: one in the vicinity of the coast and another around the shelf edge at about 13.3°E. The upwelling area stretches up to about 10.1°E close to the surface and thus further offshore than the area of negative WSC. Adjacent to that area, a region of negative vertical velocity can be found which is deepening to the west. It can be stated

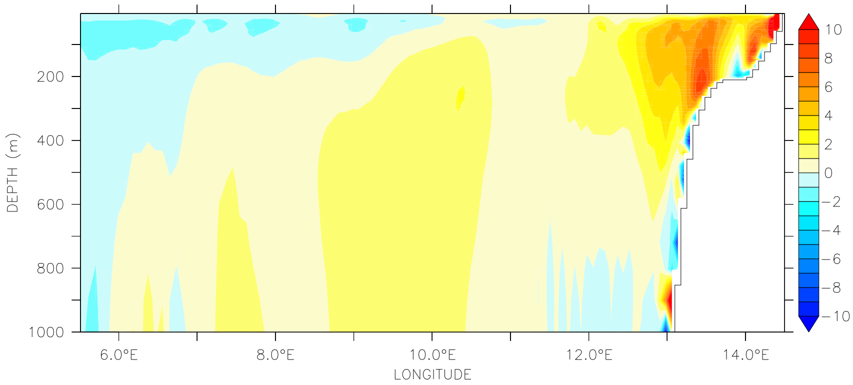

Figure 5.21. Example of the mean vertical velocity [10^{-4} cm s^{-1}] from the realistic numerical model along 24°S. Only the upper 1000 meter of the water column are shown. The basic structure of the mean vertical currents corresponds to the results of the analytical model and the numerical box model.

that the basic patterns of the vertical velocity from the realistic numerical model coincide with the results from the analytical model and the idealized box model.

As mentioned in section 2.1.3, there exists an area of positive WSC inducing downwelling adjacent to the coastal strip of negative WSC along the whole BUS. The downwelling in the negative WSC area may be a mechanism of modifying future thermocline waters when moved to the coast by the subsurface onshore transport. For sure, the cross-shelf circulation is not two-dimensional in the coastal ocean and the longshore currents must be taken into account when investigating the cross-shelf dynamics. An estimation of the horizontal circulation on the shelf can be obtained from long term mooring data recorded off Walvis Bay. Progressive vector diagrams derived from those data show an eastward displacement of about 600 km in 21 month (approx. 640 d) at 40 meter depth and a corresponding southward displacement of about 400 km, see Mohrholz et al. (2008). The ratio of net eastward to southward displacement from this example is 3 to 2. Assuming that the meridional scale of the BUS is much greater than the distance of the downwelling area to the coast, waters from the downwelling region may reach the coastal areas by the Ekman rectification flow. Of course, this estimation is very rough. The mooring data is limited to one spot on the shelf and the velocity field may be different further offshore. Moreover, the downwelling process depends on the buoyancy fluxes of the offshore drifting surface water. Rapid heating of these water masses by solar insolation may hamper downwelling. In contrast slow heating may support convection, and consequently, cold surface water can be shifted below warm oceanic waters. However, there are no observations so far that support the idea of the downwelling mechanism being involved in modifying future thermocline waters on the shelf of the BUS.

5.5.2. Seasonal variation of the different upwelling mechanism

Upwelling studies in the BUS mostly focus on coastal upwelling and its effect on SST, e.g. Hagen et al. (2001), Cole and Villacastin (2000). A reason therefore may be its easy detectability in remotely sensed data where upwelling is mirrored as a band of cold water along the coast. WSC driven upwelling, however, expresses in a slow doming of the thermocline which is instantly "destroyed" by mixed layer turbulence. This fact makes it difficult to detect this process by measurements. Since both upwelling mechanism have a different impact on the condition of marine ecosystems and their productivity it is important to determine the relative contribution of both mechanism to the vertical velocity and their seasonality, Rykaczewski and Checkley (2008). The fact that wind stress and WSC exhibit a phase opposition in the northern BUS leads to the question whether stronger WSC driven upwelling in summer may compensate weaker coastal upwelling.

In this section, analytical calculations are used to estimate the relative contribution of coastal and WSC driven upwelling and their seasonal variation in the BUS. The calculations are performed with realistic winds based on remotely sensed data. The coastal upwelling contribution is estimated using the analytical model presented in this study whereby meridional and zonal variations of the wind stress are neglected. As a consequence, the model gets independent of the alongshore coordinate and the mode summation can be performed analytically, see Fennel and Lass (1989). The water depth in the vicinity of the coast is assumed to be $H = 100\,\mathrm{m}$. The vertically averaged BVF near the coast was estimated from the realistic numerical model to be in the range of $0.8 \cdot 10^{-2}$ to $1.2 \cdot 10^{-2}\,\mathrm{s}^{-1}$. A slight seasonal variation of the stratification was assumed in the analytical model approach. The vertical velocity that is related to the WSC driven upwelling can be estimated at the bottom of the mixed layer by

$$w(H_{\mathrm{mix}}) = \frac{1}{f\rho_0}\left(\partial_x\tau_y - \partial_y\tau_x\right),$$

e.g. Gill (1982). Here, $\rho_0 = 1025\,\mathrm{kg\,m}^{-3}$ is a mean density of the ocean, and τ_y and τ_x are the wind stress components in meridional and zonal direction, respectively. The mixed layer depth is assumed to be $H_{\mathrm{mix}} = 25\,\mathrm{m}$.

Numerical circulation models cover both processes, coastal and WSC driven upwelling. Therefore, their results can be used to verify the analytical approach of calculating coastal and WSC driven upwelling separately. Moreover, they allow a more general view on the upwelling dynamics since they include also the impact of coastally trapped waves and Rossby waves. The analytical estimation of the mean vertical velocity as a sum of coastal and WSC driven upwelling is compared to the results from the realistic numerical model for January in figure 5.22. The results compare well with respect to the cross-shelf distribution of the vertical velocity component. The highest upwelling intensity ($> 6 \cdot 10^{-5}\,\mathrm{m\,s}^{-1}$) can be found in the vicinity of the coast in both the analytical approach and the numerical model. A band of less strong vertical velocities ($\approx 10^{-5}\,\mathrm{m\,s}^{-1}$) between the coast and the 300 m isobath is also captured by both results. This band is related to the WSC driven upwelling. Nevertheless, both results exhibit differences concerning the alongshore distribution of the vertical velocity patterns. Whereas the high upwelling intensity in the Cape Frio cell is captured appropriately by the analytical approach, it underestimates the vertical velocities in the Lüderitz upwelling cell. This shortcoming is even more striking for July, see figure 5.23. In general, coastal upwelling in the northern BUS is much stronger in July in both approaches. But the coastal upwelling south of the Cape Frio upwelling cell is highly underrepresented in the analytical results. In contrast to January, upwelling is almost in the entire BUS confined to the coast in July. Only off Cape Frio does WSC

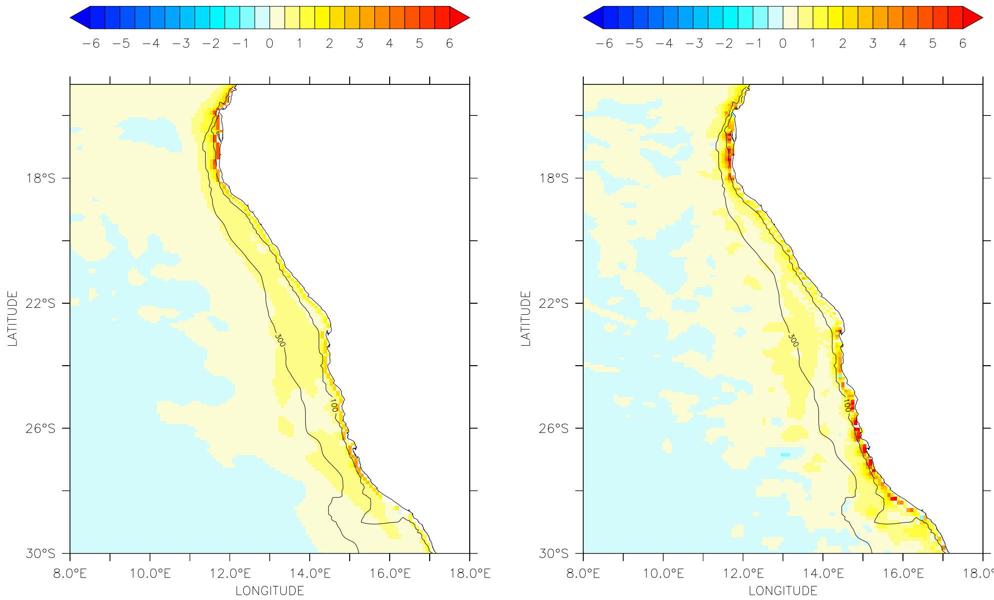

(a) Analytical approach **(b)** Numerical model

Figure 5.22. Mean vertical velocity [$10^{-5}\,\mathrm{m\,s^{-1}}$] from an analytical approach combining coastal and WSC driven upwelling compared to the results from the realistic numerical model for January at $z = 25\,\mathrm{m}$. The 100 m and 300 m depth contours are shown. The vertically averaged BVF was assumed to be $N = 1.2 \cdot 10^{-2}\,\mathrm{s}^{-1}$. The analytical approach reproduces the band of WSC induced upwelling between the coast and the 300 m depth contour.

driven upwelling play a major role. It expresses in a northward widening wedge shaped cell that is reproduced by the analytical results.

Absolute differences in the upwelling strength between the analytical approach and the numerical model can be attributed to the high idealization of the analytical model and the parameter choice. Differences in the alongshore distribution may be explained by remote effects since both results are based on the same wind forcing. The fact that the analytical approach reproduces coastal upwelling off Cape Frio appropriately, but fails in doing so southward of that cell, suggests that coastally trapped waves play a crucial role in exporting upwelling from that area southwardly. As the shelf widens to the south, an interplay with topographic features may also be relevant. Kelvin waves, for instance, slow down if the water depth decreases, and this may lead to a cumulation of upwelling similar to what Fennel et al. (2010) observed in the central Baltic Sea. What can be given as a conclusion of the comparison is that estimating the vertical velocities related to coastal upwelling from an idealized analytical model is difficult. WSC driven upwelling, however, is represented fairly well by the analytical approach. This leads to the assumption that the best estimate of the coastal upwelling strength in the BUS may be achieved from the numerical model by simply subtracting the WSC driven upwelling contribution calculated analytically.

In order to investigate the impact of both upwelling mechanism on the water composition in the mixed layer, the mean vertical velocity component at 25 meter depth is integrated zonally starting at the coast. The result depicts the offshore cumulated vertical transport (CVT) that is the amount of water transported into the mixed layer. The CVT related to both upwelling processes is presented in

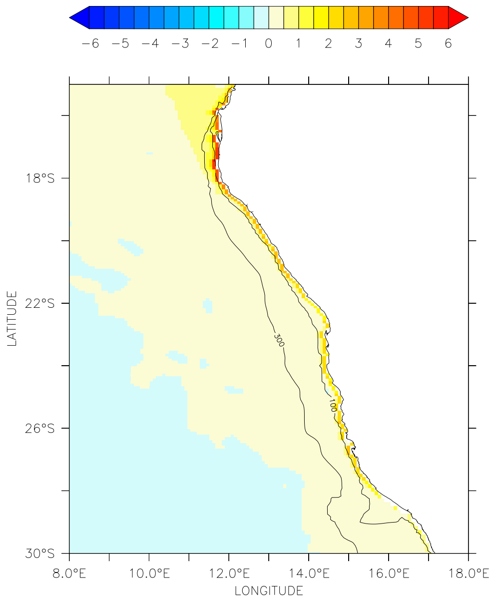

(a) Analytical approach

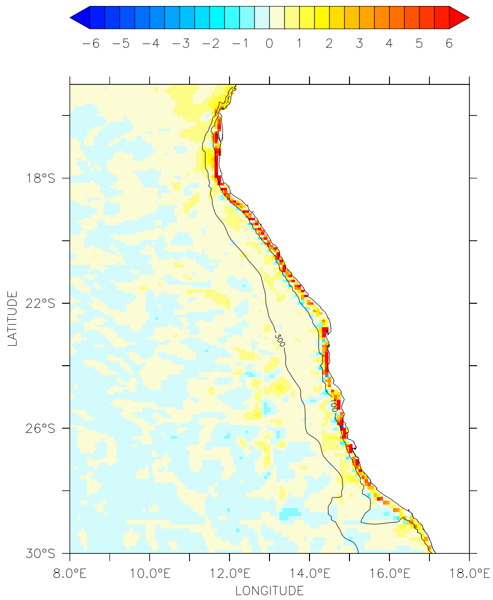

(b) Numerical model

Figure 5.23. Same as figure (5.22) but for July. The vertically averaged BVF was assumed to be $N = 0.8 \cdot 10^{-2}\,\mathrm{s}^{-1}$. The analytical approach reproduces coastal upwelling off Cape Frio appropriately but fails in doing so southward of that cell.

figure 5.24 for January. As stated above, coastal upwelling is assumed to be represented by the vertical velocity from the realistic numerical model subtracted by the WSC driven upwelling contribution. The CVT related to WSC driven and coastal upwelling is of the same order of magnitude (about $0.5\,\mathrm{m}^2\,\mathrm{s}^{-1}$) in the vicinity of the shelf edge. But here, cumulated WSC driven upwelling is about two times higher than coastal upwelling. The CVT related to the WSC shows slight maxima between 22°S and 24°S and around 26°S and 27°S. These maxima are located in a distance of about 300 to 400 km to the coast. Along the shelf break, the cumulated WSC driven upwelling is more or less homogeneous. In contrast, the cumulated coastal upwelling exhibits a higher latitudinal variability with maxima off Cape Frio, between 24°S and 26°S and south of 28°S. The sum of cumulated WSC driven and coastal upwelling (represented by the results of the realistic numerical model) is shown in figure 5.24c. The total CVT is highest off Cape Frio and south of 22°S with values of about $1\,\mathrm{m}^2\,\mathrm{s}^{-1}$. In order to highlight seasonal differences in the cumulated upwelling, the results for July are presented in figure 5.25. In contrast to January, cumulated WSC driven upwelling is of slightly smaller values than coastal upwelling almost everywhere along the shelf in July. The CVT related to coastal upwelling is dominant in a region north of 20°S, whereas between 20°S and 24°S cumulated coastal upwelling is of less importance. In summer, the sum of cumulated WSC driven and coastal upwelling is slightly higher than in winter.

The presented approach of calculating WSC driven and coastal upwelling with realistic wind fields independently of each other has some shortcomings. The estimation of WSC driven upwelling assumes a constant mixed layer depth which in reality exhibits spatial and temporal variations. And the stratification in the vicinity of the coast has been assumed to be spatially homogeneous which is certainly not the case. Nevertheless, the presented results can be regarded as an estimate demon-

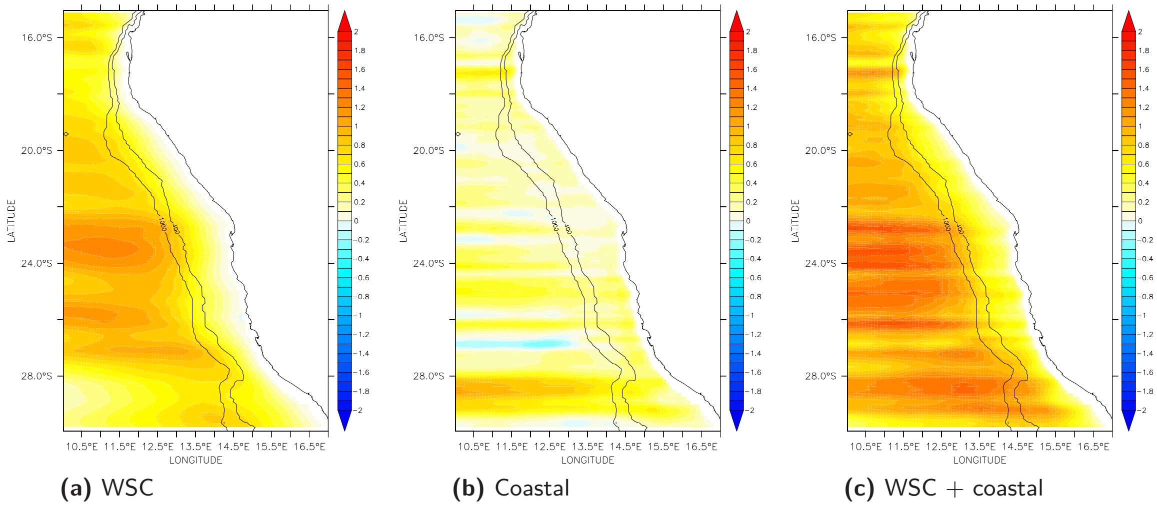

Figure 5.24. Comparison of the offshore cumulated vertical transport [$m^2\,s^{-1}$] through $z = 25\,m$ related to WSC driven and coastal upwelling for January. WSC driven upwelling is estimated analytically, whereas coastal upwelling is assumed to be represented by the vertical velocity from the realistic numerical model subtracted by the WSC driven upwelling contribution.

strating that cumulated WSC driven upwelling is of the same order as coastal upwelling and even exceeds its contribution almost everywhere along the shelf in January. The results suggest that WSC driven upwelling can compensate weaker coastal upwelling in summer. Upwelling indices that are based only on the spatial extent of cold upwelled water may therefore suffer a strong bias. Future upwelling studies need to consider WSC driven upwelling as an important mechanism of modifying the water composition in the euphotic layer in the BUS.

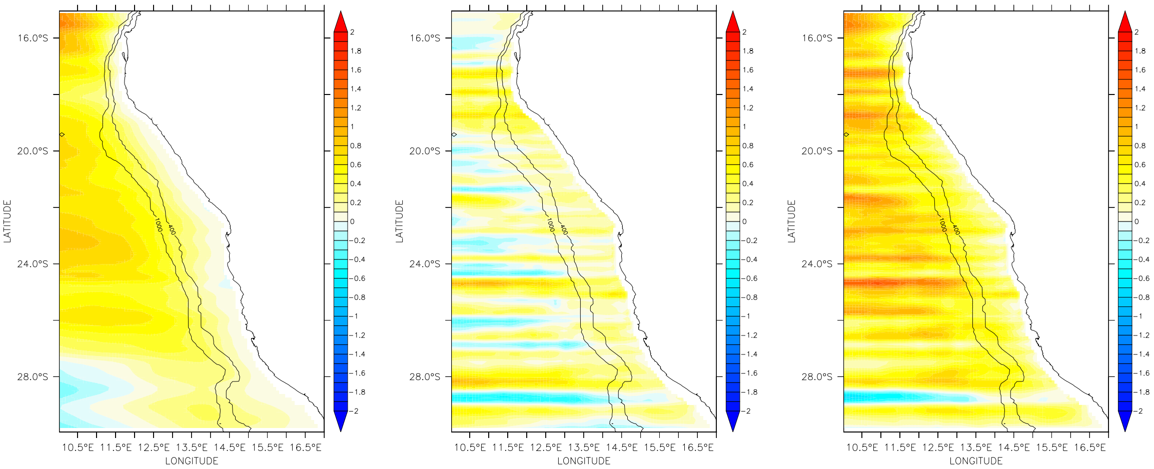

(a) WSC **(b)** Coastal **(c)** WSC + coastal

Figure 5.25. Same as figure 5.24 but for July

6. Summary

This study investigates the response of the Benguela upwelling system to spatial and temporal changes of the wind forcing. For that purpose, an analytical model based on the linear, hydrostatic Boussinesq equations was applied. The model is forced by a meridionally and zonally varying alongshore wind stress. The spatial shape of the model wind follows observations and can be adjusted by the choice of parameters. Concerning the temporal variations of the wind forcing, two cases were realized: the forcing by a switch-on wind (on the f-plane) and by a seasonally varying wind stress (β-plane). An idealized numerical box model is used to verify the analytical results. The f-plane case allows an exact analytical solution of the model equations in the frame of the long wave and the low frequency approximation, whereas for the β-plane model only an approximate solution can be achieved. Hereby was assumed that the coastal ocean is adjusted by Kelvin waves at all times, and that only seasonal variations of the wind field and westward propagating Rossby waves modify this state. Although the analytical model is mainly designed for the sub-inertial domain, some features of the response to a spatially inhomogeneous wind forcing in the near-inertial frequency range are illuminated. It turned out that the frequency of inertial oscillations experiences a "blue shift" that depends on the spatial scales of the wind forcing. The response of Rossby waves to a switch-on wind is affected in a similar manner by the wind field. The analytical model results are combined with the output of an ocean GCM and observations to elucidate some important aspects of the BUS: the dynamical reasons for the spatial patterns of the meridional currents, the temporal variability of the meridional transport and its relation to the local wind forcing, the zonal currents in the Cape Frio cell, and the relative importance of coastal and WSC driven upwelling.

The present study corroborates previous findings by showing that a zonally varying wind stress modifies the classical picture of eastern boundary currents and the upwelling dynamics. The existence of a cyclonic WSC introduces a poleward flow beside the PUC. This flow overcompensates the equatorward directed CJ in the mixed layer in the very northern part of the wind patch. The CJ itself intensifies to the south since the influence of Kelvin waves on it decreases. The poleward flow, however, weakens and deepens southward which may be explained by the modal structure of the meridional currents. Observational evidence of these peculiarities in the BUS from numerical simulations and field data is presented in this study.

Data from an ocean GCM reveals that the meridional transport in the BUS exhibits a pronounced seasonality with high interannual variations. The seasonal cycle may be triggered by the strength of the WSC. The transport is slightly directed northward in summer when the WSC is weakest and southward in winter when the WSC is strongest. The long term averaged transport is negative in the northern and positive in the southern BUS. Biannual minima in the WSC data are mirrored in the meridional transport and the coastal sea level. Interannual variations of the transport may be explained by the phase and strength of the meridional wind stress.

Analytical model results show that the zonal currents are, similar to the meridional flow, affected by spatial inhomogeneities of the wind field. The presence of a WSC and wind divergence introduces a flow beside the offshore directed Ekman transport and its onshore rectification below the mixed layer. The WSC driven current is directed onshore (offshore) in the southern (northern) half of the forcing area. Whereas the surface currents are dominated by the Ekman transport, the flow below the mixed layer is governed by the WSC dynamics. The spatial wind scales at which this contribution becomes relevant are limited to a very few hundred kilometers. These findings are used for investigating the cross-shelf dynamics in the very northern BUS – the Cape Frio cell. This region is characterized by a very localized and persistent wind forcing. A partly westward bending of the AC in the area of Cape Frio was indicated by previous studies. This study presents some observations of this feature together with an onshore flow below the mixed layer on the southern ramp of the wind patch. We propose the dynamical reason for these pattern to be the strong spatial inhomogeneity of the wind forcing.

The outcome of the analytical model reproduces the two main upwelling mechanism in the BUS: coastal upwelling that is confined to the coast and WSC driven upwelling localized within a band of a few 100 kilometers width off the coast. Analytical model results show that the vertical structure of the velocity field changes if the β-effect is considered because the trapping scale of Rossby waves exceeds the band of negative WSC. The relative importance of coastal and WSC driven upwelling and their seasonal and spatial variation is estimated by an analytical approach using observed wind fields. This approach is compared to the output of the realistic numerical model. Absolute differences are attributed to the high idealization of the analytical approach and the choice of the parameters; whereas differences in the alongshore distribution highlight the impact of coastally trapped waves on the vertical velocity. The comparison suggests that Kelvin waves play a crucial role in exporting upwelling from the Cape Frio cell southwardly (into a region governed by less wind forcing). Moreover, the comparison leads to the assumption that the best estimate of the coastal upwelling strength in the BUS may be achieved from the numerical model by simply subtracting the upwelling contribution of the WSC. It can be stated that cumulated WSC driven upwelling is in the same order of magnitude as coastal upwelling and can compensate weaker coastal upwelling in summer.

Since the present study examines the role of wind forcing in the BUS in a rather qualitative manner, it leaves scope for further investigations related to the quantification of the demonstrated processes. Some aspects that may be emphasized in future studies are: a quantification of the wind stress and WSC driven meridional advection and the relative importance of remote effects on the longshore currents; an improved understanding of the impact of coastally trapped waves on the spatial upwelling distribution in the BUS; a quantification of the impact of the cross-shore dynamics in the Cape Frio cell on the water mass composition and the ecosystem condition along the southwest African shelf. The availability of spatially high resolved wind data in the vicinity of the coast is absolutely essential for all of these issues.

A. List of analytical model parameters

Table A.1. List of parameters in the analytical f-plane model

Parameter	Meaning	Input value	Unit
f	Coriolis parameter	$6 \cdot 10^{-5}$	s^{-1}
r	Friction parameter	$0.02\,f$	s^{-1}
R_1	First mode internal Rossby Radius	50	km
R_0	External Rossby Radius	$\frac{\sqrt{gH}}{f} \approx 1650$	km
H	Water depth	1000	m
H_{mix}	Mixed layer depth	20	m
v_*^2	Squared friction velocity	0.8	$\mathrm{cm}^2\,\mathrm{s}^{-2}$
N	Brunt-Väisälä frequency	$\frac{\pi R_1 f}{H} \approx 9 \cdot 10^{-3}$	s^{-1}
$2L$	Width of the wind band (zonal direction)	1000	km
$2a$	Length of the wind band (meridional direction)	1000	km

Table A.2. List of parameters in the analytical β-plane model. Parameters from the f-plane model are valid as long as otherwise stated.

Parameter	Meaning	Input value	Unit
β	Latitudinal variation of the Coriolis parameter f	$2 \cdot 10^{-11}$	$\mathrm{m}^{-1}\,\mathrm{s}^{-1}$
r	Friction parameter	$10^{-3}\,f$	s^{-1}
ω_0	Forcing frequency	$2 \cdot 10^{-7}$	s^{-1}
$\widehat{T}$	Wind amplitude of the seasonal cycle	0.2	$-$

B. Calculation of certain important integrals

B.1. The convolution integrals $G_n * \Pi$, $G_n * \partial_{x'}\Pi$, and $\frac{1}{R_n}e^{\frac{x+x'}{R_n}} * \Pi$

We solve the convolution integrals

$$G_n * \Pi = \int_{-\infty}^{0} dx' G_n(x,x')\Pi(x'), \tag{B.1}$$

$$G_n * \partial_{x'}\Pi = \int_{-\infty}^{0} dx' G_n(x,x')\partial_{x'}\Pi(x'), \tag{B.2}$$

on the β-plane with the Green's function

$$G_n(x,x') = e^{-\frac{i\beta}{2\varpi}(x-x')}\frac{1}{2\alpha_n}\left(e^{\alpha_n(x-x')} - e^{-\alpha_n|x-x'|}\right).$$

The integrals (B.1) and (B.2) can be divided into four integrals each by using the relation

$$-|x-x'| = \left\{ \begin{array}{cc} -x+x' & |x| \leq |x'| \\ x-x' & |x'| \leq |x| \end{array} \right\}.$$

We find for (B.1)

$$\begin{aligned} G_n * \Pi = \frac{1}{2\alpha_n}\Bigg(& e^{a_1 x}\int_{-(L+l)}^{0} e^{a_2 x'}\cos(b(x'+l))dx' \\ & -\Theta(x+L+l)e^{-a_2 x}\int_{-(L+l)}^{x} e^{a_2 x'}\cos(b(x'+l))dx' \\ & -\Theta(-x-L-l)e^{a_1 x}\int_{-(L+l)}^{0} e^{-a_1 x'}\cos(b(x'+l))dx' \\ & -\Theta(x+L+l)e^{a_1 x}\int_{x}^{0} e^{-a_1 x'}\cos(b(x'+l))dx'\Bigg) \end{aligned}$$

where

$$a_1 = -\frac{i\beta}{2\varpi} + \alpha_n \qquad \text{and} \qquad a_2 = \frac{i\beta}{2\varpi} + \alpha_n.$$

The substitution $s = x' + l$ converts the single integrals to integrals of the type

$$\int e^{as}\cos(bs)ds = \frac{e^{as}}{a^2+b^2}(a\cos(bs) + b\sin(bs))$$

that can be solved in a straightforward manner. Adding the single integrals afterwards, the convolution integral reads

$$G_n * \Pi = \frac{1}{2\alpha_n}\Bigg[\left(\frac{ba_2^2}{a_2^2+b^2}-\frac{ba_1^2}{a_1^2+b^2}\right)e^{a_1 x}\sin(bl)+\left(\frac{a_2^3}{a_2^2+b^2}+\frac{a_1^3}{a_1^2+b^2}\right)e^{a_1 x}\cos(bl)$$
$$-\Theta(x+L+l)\left(\left(\frac{ba_2^2}{a_2^2+b^2}-\frac{ba_1^2}{a_1^2+b^2}\right)\sin(b(x+l))+\left(\frac{a_2^3}{a_2^2+b^2}+\frac{a_1^3}{a_1^2+b^2}\right)\cos(b(x+l))\right)$$
$$+\frac{ba_2^2}{a_2^2+b^2}e^{a_1 x}e^{-a_2(L+l)}-\Theta(-x-L-l)\frac{ba_1^2}{a_1^2+b^2}e^{a_1(x+L+l)}-\Theta(x+L+l)\frac{ba_2^2}{a_2^2+b^2}e^{-a_2(x+L+l)}\Bigg]. \tag{B.3}$$

The integral (B.2) can be solved analogously making use of the integral

$$\int e^{as}\sin(bs)ds = \frac{e^{as}}{a^2+b^2}(a\sin(bs)-b\cos(bs)).$$

The calculation yields

$$G_n * \partial_{x'}\Pi = -\frac{b}{2\alpha_n}\Bigg[\left(\frac{a_2}{a_2^2+b^2}+\frac{a_1}{a_1^2+b^2}\right)e^{a_1 x}\sin(bl)+\left(\frac{-b}{a_2^2+b^2}+\frac{b}{a_1^2+b^2}\right)e^{a_1 x}\cos(bl)$$
$$-\Theta(x+L+l)\left(\left(\frac{a_2}{a_2^2+b^2}+\frac{a_1}{a_1^2+b^2}\right)\sin(b(x+l))+\left(\frac{-b}{a_2^2+b^2}+\frac{b}{a_1^2+b^2}\right)\cos(b(x+l))\right)$$
$$+\frac{a_2}{a_2^2+b^2}e^{a_1 x}e^{-a_2(L+l)}+\Theta(-x-L-l)\frac{a_1}{a_1^2+b^2}e^{a_1(x+L+l)}-\Theta(x+L+l)\frac{a_2}{a_2^2+b^2}e^{-a_2(x+L+l)}\Bigg]. \tag{B.4}$$

During the derivation of the convolution integrals the relations

$$\Theta(x)e^{-x}+\Theta(-x)e^{x} = \Theta(x)e^{-|x|}+\Theta(-x)e^{-|x|} = (\Theta(x)+\Theta(-x))e^{-|x|} = e^{-|x|}, \tag{B.5}$$
$$\Theta(x)e^{-x}-\Theta(-x)e^{x} = \Theta(x)e^{-|x|}-\Theta(-x)e^{-|x|} = (\Theta(x)-\Theta(-x))e^{-|x|} = \operatorname{sign}(x)\,e^{-|x|} \tag{B.6}$$

were used.

The convolution integral

$$\frac{1}{R_n}e^{\frac{x+x'}{R_n}} * \Pi = \frac{1}{R_n}\int_{-\infty}^{0} dx' e^{\frac{x+x'}{R_n}}\Pi(x')$$

is calculated in the same manner as the integral (B.1). The calculation gives

$$\frac{1}{R_n}e^{\frac{x+x'}{R_n}} * \Pi = \frac{1}{1+R_n^2 b^2}\left(e^{\frac{x}{R_n}}(\cos(bl)+bR_n\sin(bl))+bR_n e^{\frac{(x-L-l)}{R_n}}\right).$$

B.2. The integrals I_n and J_n

We solve the Fourier integral

$$I_n(y,\omega) = \int \frac{-iQ(\kappa)}{\varpi\lambda_n+\kappa}e^{i\kappa y}\frac{d\kappa}{2\pi}$$

with the help of the convolution theorem and find

$$I_n = \int_{-a}^{a} \cos(\kappa_0 y')\Theta(y'-y)e^{i\lambda_n\omega(y'-y)}dy'.$$

We have to distinguish now three different cases depending on the value of y:

$$I_n(y,\omega) = \begin{cases} 0 & \text{for} \quad y > a \\ \Theta(-y-a)\displaystyle\int_{-a}^{a} \cos(\kappa_0 y')e^{i\lambda_n\omega(y'-y)}dy' & \text{for} \quad y < -a \\ \Theta(a-|y|)\displaystyle\int_{y}^{a} \cos(\kappa_0 y')e^{i\lambda_n\omega(y'-y)}dy' & \text{for} \quad -a < y < a. \end{cases}$$

Thus, we find for the integral

$$\begin{aligned} I_n(y,\omega) = \Theta(-y-a)&\frac{-1}{\kappa_0^2-\lambda_n^2\overline{\omega}^2}\Big(e^{i\lambda_n\overline{\omega}(a-y)}\left(i\lambda_n\overline{\omega}\cos(\kappa_0 a)+\kappa_0\sin(\kappa_0 a)\right) \\ &-e^{-i\lambda_n\overline{\omega}(a+y)}\left(i\lambda_n\overline{\omega}\cos(\kappa_0 a)-\kappa_0\sin(\kappa_0 a)\right)\Big) \\ +\Theta(a-|y|)&\frac{-1}{\kappa_0^2-\lambda_n^2\overline{\omega}^2}\Big(e^{i\lambda_n\overline{\omega}(a-y)}\left(i\lambda_n\overline{\omega}\cos(\kappa_0 a)+\kappa_0\sin(\kappa_0 a)\right) \\ &-\left(i\lambda_n\overline{\omega}\cos(\kappa_0 y)+\kappa_0\sin(\kappa_0 y)\right)\Big). \end{aligned} \tag{B.7}$$

We use $\cos(\kappa_0 a) = 0$ and $\sin(\kappa_0 a) = 1$ and consequently (B.7) simplifies to

$$\begin{aligned} I_n(y,\omega) = \frac{\kappa_0}{\lambda_n^2\overline{\omega}^2-\kappa_0^2}&\Big(\Theta(a-y)e^{i\lambda_n\overline{\omega}(a-y)}+\Theta(-a-y)e^{i\lambda_n\overline{\omega}(-a-y)} \\ &-\Theta(a-|y|)\left(\frac{i\lambda_n\overline{\omega}}{\kappa_0}\cos(\kappa_0 y)+\sin(\kappa_0 y)\right)\Big). \end{aligned} \tag{B.8}$$

The integral

$$J_n(y,t) = \int T(\omega)I_n(\omega,y)e^{-i\omega t}\frac{d\omega}{2\pi}$$

can be divided into four single integrals writing

$$J_n(y,t) = \Theta(a-y)H_1 + \Theta(-a-y)H_2 - \Theta(a-|y|)\left(H_3\cos(\kappa_0 y)+H_4\sin(\kappa_0 y)\right). \tag{B.9}$$

The calculation of H_3 and H_4 is straightforward and gives

$$\begin{aligned} H_3 &= \int \frac{i\lambda_n\overline{\omega}}{\lambda_n^2\overline{\omega}^2-\kappa_0^2}\frac{i}{\omega+i\epsilon}e^{-i\omega t}\frac{d\omega}{2\pi} = \frac{\Theta(t)}{\lambda_n^2 r^2+\kappa_0^2}\left(r\lambda_n - e^{-rt}\left(r\lambda_n\cos\left(\frac{\kappa_0}{\lambda_n}t\right)-\kappa_0\sin\left(\frac{\kappa_0}{\lambda_n}t\right)\right)\right) \\ H_4 &= \int \frac{\kappa_0}{\lambda_n^2\overline{\omega}^2-\kappa_0^2}\frac{i}{\omega+i\epsilon}e^{-i\omega t}\frac{d\omega}{2\pi} = \frac{\Theta(t)}{\lambda_n^2 r^2+\kappa_0^2}\left(-\kappa_0 + e^{-rt}\left(r\lambda_n\sin\left(\frac{\kappa_0}{\lambda_n}t\right)+\kappa_0\cos\left(\frac{\kappa_0}{\lambda_n}t\right)\right)\right). \end{aligned}$$

Adding both integrals according to (B.9), we find

$$\cos(\kappa_0 y)H_3+\sin(\kappa_0 y)H_4 = \frac{\Theta(t)}{\lambda_n r\left(1+\frac{\kappa_0^2}{r^2\lambda_n^2}\right)}\left(\cos(\kappa_0 y)-\frac{\kappa_0}{r\lambda_n}\sin(\kappa_0 y)-e^{-rt}\Psi_n\left(y+\frac{t}{\lambda_n}\right)\right)$$

where

$$\Psi_n\left(y+\frac{t}{\lambda_n}\right)=\cos\left(\kappa_0\left(y+\frac{t}{\lambda_n}\right)\right)-\frac{\kappa_0}{r\lambda_n}\sin\left(\kappa_0\left(y+\frac{t}{\lambda_n}\right)\right) \tag{B.10}$$

was introduced for convenience.

The calculation of the integrals H_1 and H_2 compares to the calculation of the integral H_3. We find

$$\begin{aligned}
H_1 &= \int \frac{\kappa_0}{\lambda_n^2\overline{\omega}^2-\kappa_0^2}\frac{i}{\omega+i\epsilon}e^{i\lambda_n\overline{\omega}(a-y)}e^{-i\omega t}\frac{d\omega}{2\pi}\\
&= \frac{\Theta(t-\lambda_n(a-y))}{\lambda_n^2r^2+\kappa_0^2}\left(-\kappa_0 e^{-r\lambda_n(a-y)}+e^{-rt}\left(r\lambda_n\sin\left(\frac{\kappa_0}{\lambda_n}(t-\lambda_n(a-y))\right)\right.\right.\\
&\qquad\left.\left.+\kappa_0\cos\left(\frac{\kappa_0}{\lambda_n}(t-\lambda_n(a-y))\right)\right)\right)
\end{aligned}$$

and

$$\begin{aligned}
H_2 &= \int \frac{\kappa_0}{\lambda_n^2\overline{\omega}^2-\kappa_0^2}\frac{i}{\omega+i\epsilon}e^{i\lambda_n\overline{\omega}(-a-y)}e^{-i\omega t}\frac{d\omega}{2\pi}\\
&= \frac{\Theta(t+\lambda_n(a+y))}{\lambda_n^2r^2+\kappa_0^2}\left(-\kappa_0 e^{r\lambda_n(a+y)}+e^{-rt}\left(r\lambda_n\sin\left(\frac{\kappa_0}{\lambda_n}(t+\lambda_n(a+y))\right)\right.\right.\\
&\qquad\left.\left.+\kappa_0\cos\left(\frac{\kappa_0}{\lambda_n}(t+\lambda_n(a+y))\right)\right)\right).
\end{aligned}$$

Both integrals can be simplified using the identities

$$\begin{aligned}
\cos\left(\kappa_0\left(\frac{t}{\lambda_n}\pm a+y\right)\right) &= \cos(\pm\kappa_0 a)\cos\left(\kappa_0\left(\frac{t}{\lambda_n}+y\right)\right)-\sin(\pm\kappa_0 a)\sin\left(\kappa_0\left(\frac{t}{\lambda_n}+y\right)\right)\\
&= \mp\sin\left(\kappa_0\left(\frac{t}{\lambda_n}+y\right)\right)
\end{aligned}$$

and

$$\begin{aligned}
\sin\left(\kappa_0\left(\frac{t}{\lambda_n}\pm a+y\right)\right) &= \sin(\pm\kappa_0 a)\cos\left(\kappa_0\left(\frac{t}{\lambda_n}+y\right)\right)+\cos(\pm\kappa_0 a)\sin\left(\kappa_0\left(\frac{t}{\lambda_n}+y\right)\right)\\
&= \pm\cos\left(\kappa_0\left(\frac{t}{\lambda_n}+y\right)\right).
\end{aligned}$$

Rewriting H_1 and H_2 using (B.10) yields

$$\begin{aligned}
H_1 &= \frac{\Theta(t-\lambda_n(a-y))}{\lambda_n r\left(1+\frac{\kappa_0^2}{r^2\lambda_n^2}\right)}\left(-\frac{\kappa_0}{r\lambda_n}e^{-r\lambda_n(a-y)}+e^{-rt}\Psi_n\left(y+\frac{t}{\lambda_n}\right)\right),\\
H_2 &= \frac{\Theta(t+\lambda_n(a+y))}{\lambda_n r\left(1+\frac{\kappa_0^2}{r^2\lambda_n^2}\right)}\left(-\frac{\kappa_0}{r\lambda_n}e^{r\lambda_n(a+y)}-e^{-rt}\Psi_n\left(y+\frac{t}{\lambda_n}\right)\right).
\end{aligned}$$

Finally, we sum up the single integrals to find

$$
\begin{aligned}
J_n(y,t) = {} & \frac{\Theta(t)\Theta(a-|y|)}{\lambda_n r(1+\frac{\kappa_0^2}{r^2\lambda_n^2})}\left(\cos(\kappa_0 y) - \frac{\kappa_0}{r\lambda_n}\sin(\kappa_0 y) - e^{-rt}\Psi_n\left(y+\frac{t}{\lambda_n}\right)\right) \\
& + \frac{\Theta(a-y)\Theta(t-\lambda_n(a-y))}{\lambda_n r(1+\frac{\kappa_0^2}{r^2\lambda_n^2})}\left(\frac{\kappa_0}{r\lambda_n}e^{-r\lambda_n(a-y)} + e^{-rt}\Psi_n\left(y+\frac{t}{\lambda_n}\right)\right) \\
& + \frac{\Theta(-a-y)\Theta(t+\lambda_n(a+y))}{\lambda_n r(1+\frac{\kappa_0^2}{r^2\lambda_n^2})}\left(\frac{\kappa_0}{r\lambda_n}e^{-r\lambda_n(-a-y)} - e^{-rt}\Psi_n\left(y+\frac{t}{\lambda_n}\right)\right). \qquad \text{(B.11)}
\end{aligned}
$$

C. Deriving the formal solution for p_n

C.1. Calculation of the Green's function K_n

The Green's function for the pressure obeys the equation

$$\partial_x{}^2 K_n(x,x') - \frac{\beta}{i\omega}\partial_x K_n(x,x') - (\kappa^2 + R_n^{-2})K_n(x,x') = \delta(x-x') \tag{C.1}$$

with the boundary conditions

$$\partial_x K_n(0,x') + \xi K_n(0,x') = 0 \qquad \text{and} \qquad K_n(-\infty,x') \to 0. \tag{C.2}$$

The variable $\xi = \kappa\frac{f}{\omega}$ has been introduced in section 3.4.1. The basic idea of calculating the Green's function is to compose it from two linearly independent solutions $K_n^<(x,x')$ and $K_n^>(x,x')$ for the intervals $x = [-\infty, x'[$ and $x =]x', 0]$, respectively,

$$K_n(x,x') = K_n^<(x,x')\Theta(x'-x) + K_n^>(x,x')\Theta(x-x').$$

Let Φ and Ψ be now two linearly independent solutions of the homogenous differential equation (C.1), where Ψ fulfills the boundary condition at $x=-\infty$ and Φ at $x=0$. Then, the functions $K_n^<(x,x')$ and $K_n^>(x,x')$ can be constructed in the way that,

$$\begin{aligned} K_n^>(x,x') &= \frac{\Psi(x')\Phi(x)}{W(x')}, \\ K_n^<(x,x') &= \frac{\Psi(x)\Phi(x')}{W(x')}, \end{aligned}$$

where $W(x) = \Psi\partial_x\Phi - \Phi\partial_x\Psi$ is the Wronski determinant, see Fennel and Lass (1989). Hence, using the ansatz

$$\Phi(x) = e^{-\frac{i\beta}{2\omega}x}\varphi(x) \qquad \text{and} \qquad \Psi(x) = e^{-\frac{i\beta}{2\omega}x}\psi(x) \tag{C.3}$$

the Green's function can be calculated by

$$K_n(x,x') = \frac{e^{-\frac{i\beta}{2\omega}(x+x')}}{W(x')}\left(\varphi(x)\psi(x')\Theta(x'-x) + \psi(x)\varphi(x')\Theta(x-x')\right). \tag{C.4}$$

We now have to estimate the functions Φ and Ψ. Inserting (C.3) in the homogenous version of (C.1) and the corresponding boundary conditions (C.2) yields

$$\partial_x^2\varphi - \alpha_n^2\varphi = 0 \qquad \text{and} \qquad \partial_x\varphi(0) + \left(\xi - i\frac{\beta}{2\varpi}\right)\varphi(0) = 0 \tag{C.5}$$

and

$$\partial_x^2\psi - \alpha_n^2\psi = 0 \qquad \text{and} \qquad \psi(-\infty) = 0, \tag{C.6}$$

where $\alpha_n^2 = \kappa^2 + R_n^{-2} - \frac{\beta^2}{4\varpi^2}$. A solution for (C.5) and (C.6) can be derived using the ansatz $\psi(x) = Ae^{\alpha_n x} + Be^{-\alpha_n x}$ and $\varphi(x) = A\cosh(\alpha_n x) + B\sinh(\alpha_n x)$. Then follows

$$\begin{aligned}
\psi(x) &= e^{\alpha_n x},\\
\varphi(x) &= \frac{1}{2}\left[e^{\alpha_n x} + e^{-\alpha_n x} - \frac{1}{\alpha_n}\left(\xi - \frac{i\beta}{2\varpi}\right)\left(e^{\alpha_n x} - e^{-\alpha_n x}\right)\right]
\end{aligned}$$

and the Wronski determinant amounts to

$$W(x) = \Psi\partial_x\Phi - \Phi\partial_x\Psi = e^{-\frac{i\beta}{\varpi}x}\left(\psi(x)\partial_x\varphi(x) - \varphi(x)\partial_x\psi(x)\right) = e^{-\frac{i\beta}{\varpi}x}\left(\frac{i\beta}{2\varpi} - \xi - \alpha_n\right). \tag{C.7}$$

In order to calculate the two solutions $K_n^{<}(x,x')$ and $K_n^{>}(x,x')$, we need to estimate the products $\varphi(x')\psi(x)$ and $\psi(x')\varphi(x)$ which give

$$\begin{aligned}
\varphi(x')\psi(x) &= \frac{1}{2\alpha_n}\left[e^{\alpha_n(x+x')}\left(\alpha_n - \xi + \frac{i\beta}{2\varpi}\right) + e^{-\alpha_n(x'-x)}\left(\alpha_n + \xi - \frac{i\beta}{2\varpi}\right)\right],\\
\psi(x')\varphi(x) &= \frac{1}{2\alpha_n}\left[e^{\alpha_n(x+x')}\left(\alpha_n - \xi + \frac{i\beta}{2\varpi}\right) + e^{-\alpha_n(x-x')}\left(\alpha_n + \xi - \frac{i\beta}{2\varpi}\right)\right].
\end{aligned}$$

Inserting them and the Wronski determinant (C.7) into (C.4) by using the relation (B.5) we finally find the Green's function for the pressure

$$K_n(x,x') = \frac{1}{2\alpha_n}e^{-\frac{i\beta}{2\varpi}(x-x')}\left(e^{\alpha_n(x+x')}\frac{\frac{i\beta}{2\varpi} + \alpha_n - \xi}{\frac{i\beta}{2\varpi} - \alpha_n - \xi} - e^{-\alpha_n|x-x'|}\right). \tag{C.8}$$

C.2. Source representation for p_n

In order to derive a source representation for the pressure p_n, we define a differential operator $\boldsymbol{D}_n$ from equation (3.58) as

$$\boldsymbol{D}_n(x) \coloneqq \partial_x^2 - \frac{\beta}{i\varpi}\partial_x - (\kappa^2 + R_n^{-2}).$$

The forcing term on the RHS of (3.53) is defined as

$$\mathcal{F}_n \coloneqq \frac{f}{i\varpi}\partial_x Y_n.$$

Then, we can write (3.58) and (3.53) as

$$\boldsymbol{D}_n(x')K_n(x,x') = \delta(x-x'),$$
$$\boldsymbol{D}_n(x')p_n(x') = \mathcal{F}_n(x').$$

Multiplying the first equation with $p_n(x')$ and the second with $K_n(x,x')$ and subtracting the second from the first gives

$$p_n(x')\boldsymbol{D}_n(x')K_n(x,x') - K_n(x,x')\boldsymbol{D}_n(x')p_n(x') = p_n(x')\delta(x-x') - K_n(x,x')\mathcal{F}_n(x').$$

Integrating this equation from $-\infty$ to 0 and rearranging yields

$$p_n(x) = -\int_{-\infty}^{0} \left[p(x')\boldsymbol{D}_n(x')K_n(x,x') - K_n(x,x')\boldsymbol{D}_n(x')p_n(x')\right] dx' + \int_{-\infty}^{0} K_n(x,x')\mathcal{F}_n(x')dx'.$$

Integration by parts twice gives

$$p_n(x) = -\left[K_n(x,x')\partial_{x'}p_n(x') - p_n(x')\partial_{x'}K_n(x,x') - \frac{\beta}{i\varpi}K_n(x,x')p_n(x')\right]_{-\infty}^{0} + \int_{-\infty}^{0} K_n(x,x')\mathcal{F}_n(x')dx'.$$

We use now the boundary conditions of the Green's function K_n, see (C.2), and the pressure p_n and find

$$p_n(x) = -\frac{f}{i\varpi}K_n(x,0)Y(0) - p_n(x,0)\left(\frac{\beta}{i\varpi}K_n(x,0) + \xi K_n(x,0) + \partial_{x'}K_n(x,x')|_{x'=0}\right) + \int_{-\infty}^{0} K_n(x,x')\mathcal{F}_n(x')dx'.$$

The Term $p_n(x,0)\left(\frac{\beta}{i\varpi}K_n(x,0) + \xi K_n(x,0) + \partial_{x'}K_n(x,x')|_{x'=0}\right)$ vanishes because of $\partial_{x'}K_n(x,x')|_{x'=0} = -\left(\xi + a_1 - a_2\right)K_n(x,0)$ and $\frac{\beta}{i\varpi} = a_1 - a_2$. Further note that

$$K_n(x,0) = -e^{a_1 x}\frac{1}{\xi + a_1},$$
$$\partial_{x'}K_n(x,x') = e^{a_1 x}\left(1 - \frac{a_2}{\xi + a_1}e^{a_2 x'}\right),$$
$$\partial_{x'}K_n(x,x')|_{x'=0} = e^{a_1 x}\left(\frac{\xi + a_1 - a_2}{\xi + a_1}\right).$$

Finally, we end up with a source representation for the pressure

$$p_n(x) = -\frac{f}{i\varpi}K_n(x,0)Y(0) + \frac{f}{i\varpi}K_n * \partial_{x'}Y_n$$

where

$$K_n * \partial_{x'}Y_n = \int_{-\infty}^{0} K_n(x,x')\,\partial_{x'}Y_n(x')\,dx'.$$

Bibliography

Anderson, D. L. and Gill, A. (1975). Spin-up of a stratified ocean, with applications to upwelling. *Deep Sea Research and Oceanographic Abstracts*, 22(9):583 – 596.

Bakun, A. and Nelson, C. S. (1991). The Seasonal Cycle of Wind-Stress Curl in Subtropical Eastern Boundary Current Regions. *Journal of Physical Oceanography*, 21(12):1815–1834.

Bentamy, A., Grodsky, S. A., Carton, J. A., Croizé-Fillon, D., and Chapron, B. (2012). Matching ASCAT and QuikSCAT winds. *Journal of Geophysical Research*, 117(C2):C02011.

Chavez, F. P. and Messie, M. (2009). A comparison of Eastern Boundary Upwelling Ecosystems. *Progress in Oceanography*, 83:80–96.

Clarke, A. J. (1989). Theoretical understanding of eastern ocean boundary poleward undercurrents. In Neshyba, S. J., Mooers, C., Smith, R., and Barber, R., editors, *Poleward Flows Along Eastern Ocean Boundaries*, volume 34 of *Coastal Estuarine Studies*, pages 26–39. AGU, Washington, D. C.

Colberg, F. and Reason, C. J. C. (2006). A model study of the Angola Benguela Frontal Zone: Sensitivity to atmospheric forcing. *Geophysical Research Letters*, 33(19):1–6.

Cole, J. and Villacastin, C. (2000). Sea surface temperature variability in the northern Benguela upwelling system, and implications for fisheries research. *International Journal of Remote Sensing*, 21(8):1597–1617.

Crépon, M., Richez, C., and Chartier, M. (1984). Effects of Coastline Geometry on Upwellings. *Journal of Physical Oceanography*, 14(8):1365–1382.

Fennel, W. (1999). Theory of the Benguela Upwelling System. *Journal of Physical Oceanography*, 29(2):177–190.

Fennel, W., Junker, T., Schmidt, M., and Mohrholz, V. (2012). Response of the Benguela upwelling systems to spatial variations in the wind stress. *Continental Shelf Research*, 45(0):65–77.

Fennel, W. and Lass, H. U. (1989). *Analytical Theory of Forced Oceanic Waves*. Akademie-Verlag Berlin.

Fennel, W. and Lass, H. U. (2007). On the impact of wind curls on coastal currents. *Journal of Marine Systems*, 68:128–142.

Fennel, W. and Neumann, T. (2004). *Introduction to the Modelling of Marine Ecosystem*, volume 72 of *Elsevier Oceanography Series*. Elsevier.

Fennel, W., Radtke, H., Schmidt, M., and Neumann, T. (2010). Transient upwelling in the central Baltic Sea. *Continental Shelf Research*, 30(19):2015 – 2026.

Florenchie, P., Lutjeharms, J. R. E., Reason, C. J. C., Masson, S., and Rouault, M. (2003). The source of Benguela Niños in the South Atlantic Ocean. *Geophysical Research Letters*, 30(10):1505–1507.

Gammelsrød, T., Bartholomae, C. H., Boyer, D. C., Filipe, V. L. L., and O'Toole, M. J. (1998). Intrusion of warm surface water along the Angolan-Namibian coast in February-March 1995: the 1995 Benguela Niño. *South African Journal of Marine Science*, 19(1):41–56.

Gill, A. E. (1982). *Atmosphere-ocean dynamics*, volume 30 of *International Geophysics Series*. Academic Press.

Gordon, A. L., Bosley, K. T., and III, F. A. (1995). Tropical atlantic water within the Benguela upwelling system at 27°S. *Deep Sea Research Part I: Oceanographic Research Papers*, 42(1):1 – 12.

Griffies, S. (2007). Elements of mom4p1. GFDL Ocean Group Technical Report 6, NOAA/Geophysical Fluid Dynamics Laboratory. Available online at http://www.gfdl.noaa.gov/ fms.

Gutknecht, E., Dadou, I., Charria, G., Cipollini, P., and Garcon, V. (2010). Spatial and temporal variability of the remotely sensed chlorophyll a signal associated with Rossby waves in the South Atlantic Ocean. *Journal of Geophysical Research*, 115:C05004.

Hagen, E., Feistel, R., Agenbag, J. J., and Ohde, T. (2001). Seasonal and interannual changes in Intense Benguela Upwelling (1982-1999). *Oceanologica Acta*, 24(6):557 – 568.

Herzfeld, M., Schmidt, M., Griffies, S., and Liang, Z. (2011). Realistic test cases for limited area ocean modelling. *Ocean Modelling*, 37:1 – 34.

Houry, S., Dombrowsky, E., Mey, P. D., and Minster, J.-F. (1987). Brunt-Väisälä Frequency and Rossby Radii in the South Atlantic. *Journal of Physical Oceanography*, 17:1619–1626.

Hurlburt, H. E. and Thompson, J. D. (1973). Coastal Upwelling on a β-Plane. *Journal of Physical Oceanography*, 3(1):16–32.

Hutchings, L., van der Lingen, C., Shannon, L., Crawford, R., Verheye, H., Bartholomae, C., van der Plas, A., Louw, D., Kreiner, A., Ostrowski, M., Fidel, Q., Barlow, R., Lamont, T., Coetzee, J., Shillington, F., Veitch, J., Currie, J., and Monteiro, P. (2009). The Benguela Current: An ecosystem of four components. *Progress In Oceanography*, 83(1–4):15–32.

John, H.-C., Mohrholz, V., Lutjeharms, J., Weeks, S., Cloete, R., Kreiner, A., and da Silva Neto, D. (2004). Oceanographic and faunistic structures across an Angola Current intrusion into northern Namibian waters. *Journal of Marine Systems*, 46(14):1 – 22.

Johnson, J. A. (1976). Modifications of coastal currents and upwelling by offshore variations in wind stress. *Tellus*, 28(3):254–260.

Kanzow, T., Cunningham, S. A., Johns, W. E., Hirschi, J. J.-M., Marotzke, J., Baringer, M. O., Meinen, C. S., Chidichimo, M. P., Atkinson, C., Beal, L. M., Bryden, H. L., and Collins, J. (2010). Seasonal Variability of the Atlantic Meridional Overturning Circulation at 26.5°N. *Journal of Climate*, 23(21):5678–5698.

Kundu, P. K., Chao, S.-Y., and McCreary, J. P. (1983). Transient coastal currents and inertio-gravity waves. *Deep Sea Research Part A. Oceanographic Research Papers*, 30(10):1059 – 1082.

Kundu, P. K. and Thomson, R. E. (1985). Inertial Oscillations due to a Moving Front. *Journal of Physical Oceanography*, 15(8):1076–1084.

Lass, H. U. and Mohrholz, V. (2008). On the interaction between the subtropical gyre and the Subtropical Cell on the shelf of the SE Atlantic. *Journal of Marine Systems*, 74:1 – 43.

Lass, H. U., Schmidt, M., Mohrholz, V., and Nausch, G. (2000). Hydrographic and Current Measurements in the Area of the Angola-Benguela Front. *Journal of Physical Oceanography*, 30(10):2589–2609.

Le Traon, P.-Y. and Minster, J.-F. (1993). Sea level variability and semiannual Rossby waves in the South Atlantic subtropical gyre. *Journal of Geophysical Research: Oceans*, 98(C7):12315–12326.

LeBlond, P. H. and Mysak, L. A. (1978). *Waves in the ocean*, volume 20 of *Elsevier Oceanography Series*. Elsevier.

Maximenko, N., Niiler, P., Centurioni, L., Rio, M.-H., Melnichenko, O., Chambers, D., Zlotnicki, V., and Galperin, B. (2009). Mean Dynamic Topography of the Ocean Derived from Satellite and Drifting Buoy Data Using Three Different Techniques. *Journal of Atmospheric and Oceanic Technology*, 26(9):1910–1919.

McCreary, J. P. (1981). A Linear Stratified Ocean Model of the Coastal Undercurrent. *Philosophical Transactions of the Royal Society of London. Series A, Mathematical and Physical Sciences*, 302(1469):385–413.

McCreary, J. P. and Chao, S.-Y. (1985). Three-dimensional shelf circulation along an eastern ocean boundary. *Journal of Marine Research*, 43(1):13–36.

McCreary, J. P., Kundu, P. K., and Chao, S.-Y. (1987). On the dynamics of the California Current system. *Journal of Marine Research*, 45:1–32(32).

Meeuwis, J. M. and Lutjeharms, J. R. E. (1990). Surface thermal characteristics of the Angola-Benguela front. *South African Journal of Marine Science*, 9(1):261–279.

Mohrholz, V., Bartholomae, C., van der Plas, A., and Lass, H. (2008). The seasonal variability of the northern Benguela undercurrent and its relation to the oxygen budget on the shelf. *Continental Shelf Research*, 28(3):424 – 441.

Mohrholz, V., Schmidt, M., and Lutjeharms, J. (2001). The hydrography and dynamics of the Angola-Benguela Frontal Zone and environment in April 1999. *South African Journal of Science*, 97:199–208.

Muller, A. (2013). *Cross-shore exchange in the northern Benguela and the related role of upwelling filaments*. PhD thesis, University of Cape Town.

Muller, A. A., Mohrholz, V., and Schmidt, M. (2013). The circulation dynamics associated with a northern Benguela upwelling filament during October 2010. *Continental Shelf Research*, 63(0):59 – 68.

Peterson, R. G. and Stramma, L. (1991). Upper-level circulation in the South Atlantic Ocean. *Progress In Oceanography*, 26(1):1–73.

Philander, S. G. H. and Yoon, J. H. (1982). Eastern boundary currents and coastal upwelling. *Journal of Physical Oceanography*, 12(8):862–879.

Reason, C. J. C., Mysak, L. A., and Cummins, P. F. (1987). Generation of Annual-Period Rossby Waves in the South Atlantic Ocean by the Wind Stress Curl. *Journal of Physical Oceanography*, 17(11):2030–2042.

Richter, I., Behera, S. K., Masumoto, Y., Taguchi, B., Komori, N., and Yamagata, T. (2010). On the triggering of Benguela Niños: Remote equatorial versus local influences. *Geophysical Research Letters*, 37:L20604.

Risien, C. M. and Chelton, D. B. (2008). A Global Climatology of Surface Wind and Wind Stress Fields from Eight Years of QuikSCAT Scatterometer Data. *Journal of Physical Oceanography*, 38(11):2379–2413.

Rouault, M., Illig, S., Bartholomae, C., Reason, C., and Bentamy, A. (2007). Propagation and origin of warm anomalies in the Angola Benguela upwelling system in 2001. *Journal of Marine Systems*, 68:473 – 488.

Rykaczewski, R. R. and Checkley, D. M. (2008). Influence of ocean winds on the pelagic ecosystem in upwelling regions. *Proceedings of the National Academy of Sciences*, 105(6):1965–1970.

Schmidt, M. and Eggert, A. (2012). A regional 3D coupled ecosystem model of the Benguela upwelling system. Marine Science Reports 87, Institute for Baltic Sea Research, Warnemuende, Germany. Available online at http://www.io-warnemuende.de/marine-science-reports.html.

Schumann, E. H. and Brink, K. H. (1990). Coastal-Trapped Waves off the Coast of South Africa: Generation, Propagation and Current Structures. *Journal of Physical Oceanography*, 20(8):1206–1218.

Shannon, L. (1985). The Benguela ecosystem, Part I. Evolution of the Benguela, physical features and processes. *Oceanography and marine biology, An annual review*, 23:105–182.

Shannon, L. and Nelson, G. (1996). The Benguela: Large Scale Features and Processes and System Variability. In Wefer, G., Berger, W. H., Siedler, G., and Webb, D. J., editors, *The South Atlantic - Present and Past Circulation*, pages 163–210. Springer-Verlag.

Shillington, F. (1998). *The Benguela Upwelling System off Southwestern Africa*, volume 11 of *The Sea*, chapter 20, pages 583–604. Wiley. Allan R. Robinson and Kenneth H. Brink.

Shillington, F., Reason, C. J. C., Rae, C. M. D., Florenchie, P., and Penven, P. (2006). *Large Scale Physical Variability of the Benguela Current Large Marine Ecosystem (BCLME)*, volume 14 of *Large Marine Ecosystems Series*, chapter 4, pages 47–68. Elsevier. V. Shannon, G. Hempel, P. Malanotte-Rizzoli, C. Moloney and J. Woods (Editors).

Suginohara, N. and Kitamura, Y. (1984). Long-Term Coastal Upwelling over a Continental Shelf-Slope. *Journal of Physical Oceanography*, 14(6):1095–1104.

Veitch, J., Penven, P., and Shillington, F. (2010). Modeling Equilibrium Dynamics of the Benguela Current System. *Journal of Physical Oceanography*, 40(9):1942–1964.

Witter, D. L. and Gordon, A. L. (1999). Interannual variability of South Atlantic circulation from 4 years of TOPEX/POSEIDON satellite altimeter observations. *Journal of Geophysical Research: Oceans*, 104(C9):20927–20948.

Xu, Z., Li, M., Patricola, C. M., and Chang, P. (2013). Oceanic origin of southeast tropical Atlantic biases. *Climate Dynamics*, :1–16.

Eidesstattliche Erklärung

Ich versichere hiermit an Eides statt, dass ich die vorliegende Arbeit selbstständig angefertigt und ohne fremde Hilfe verfasst habe. Dazu habe ich keine außer den von mir angegebenen Hilfsmitteln und Quellen verwendet und die den benutzten Werken inhaltlich und wörtlich entnommenen Stellen habe ich als solche kenntlich gemacht.

Rostock, July 28, 2014 Tim Junker